

Simulations of group-delay tracking strategies in the astronomical K and L bands

For improved sensitivities at the Very Large Telescope Interferometer

INAUGURAL-DISSERTATION

zur

Erlangung des Doktorgrades
der Mathematisch-Naturwissenschaftlichen Fakultät
der Universität zu Köln



vorgelegt von

Balaji Muthusubramanian
aus Chennai, India

Köln 2019

Berichterstatter: Prof. Dr. Lucas Labadie
Prof. Dr. Yaping Shao

Tag der letzten mündlichen Prüfung: 23.04.2018

Dedicated to the loving memory of Prof. P. Devadas.

1922 – 2016.

The man who inspired this 10 year old kid to be a professional Astronomer.

ABSTRACT

Motivation:

Atmospheric turbulence is a major issue in achieving high angular resolutions for optical and infrared astronomical observations. Such turbulences induce phase fluctuations on the incoming stellar wavefronts. With the recent advances in Adaptive Optics, we can overcome this effect and remove most of the aberrations on the stellar wavefront. However, the global phase shift (piston) which is not corrected by the adaptive optics system, plays a significant role in optical and infrared interferometry. The piston or Optical Path Difference (OPD) fluctuations induced by atmospheric turbulence and instrumental vibrations at an interferometer affects the position of the fringes on the detector and thus influencing the visibility measurements. Thus, a dedicated fringe tracker is required in addition to the adaptive optics system in an optical or infrared interferometer.

The fringes can be tracked in two ways, namely group delay tracking and phase delay tracking. Phase delay tracking involves in tracking each individual fringe phases and group delay tracking involves in tracking the fringe envelope. Currently the Very Large Telescope Interferometer (VLTI) houses GRAVITY fringe tracker, FINITO and PRIMA FSU which tracks group and phase delays in H and K bands. However, targets such as Young Stellar Objects (YSO), dusty torus around Active Galactic Nuclei (AGN), etc. are brighter at longer wavelengths due to the presence of dust around them. Hence in this work, I explore the possibility of on-source fringe tracking in the L band alongside K band. Fringe tracking in L band is advantageous due to its longer atmospheric coherence time and larger Fried parameter as compared to that of shorter wavelengths. I also extend my work in performing feed-forward group delay estimation at mid-infrared wavelengths using inter-band dispersion between K and L bands.

The main goal of the work is to analyze the performance of a simultaneous K and L band group delay tracker which keeps the fringe frames of the science channel within coherence length. The sensitivity of the science channel can then be increased by stacking each frame by its power spectrum.

Method:

To analyze the performance of a fringe tracker at K and L bands, I have developed a atmospheric turbulence simulator (GDsim) which includes atmospheric water vapor dispersion and instrumental vibrations at the VLTI. The simulated OPD fluctuations are then injected into simulated noisy K and L band fringes over different lengths

integration times. Group delay is then estimated from the resulting fringes through spectrally dispersed ABCD encoding technique, least squares estimation and the double Fourier technique. The performance and sensitivity of each of the group delay estimation algorithm is then estimated by comparing the simulated input group delay and the measured group delay.

Result:

The loss in fringe contrast over integration time follows a random walk behavior due to the temporal decorrelation of the phase fluctuations at each telescope over long integration times ($T_{\text{int}} \geq 1.79\tau_0$). Thus the Signal to Noise Ratio (SNR) on the correlated flux is unreliable in estimating the sensitivity of a group delay tracker at such integration times. Alternatively, by analyzing the Root Mean Squared (RMS) on the residual group delay for each group delay estimation algorithm, we can estimate the sensitivity and performance of the group delay tracker simultaneously. However, the threshold on the RMS of the residual group delay (input group delay - measured group delay) depends on the spectral resolution of the science channel for incoherent stacking of fringe frames. For astronomical observations in the L band with MATISSE at low spectral resolution ($R=30$) with an acceptable maximum loss in fringe contrast of 10%, we can perform coherencing with a K and L band sensitivities in the range of 13.36 - 14.67 magnitudes and 6.64 - 10.02 magnitudes respectively for the different group delay estimation algorithms.

Feed forward group delay tracking performance and sensitivity at mid-infrared wavelengths (M & N bands) can be estimated by comparing the individual group delay estimation errors in K and L bands. The sensitivity to perform feed forward group delay tracking using only K and L band group delay information for science in the N band with MATISSE at low spectral resolution ($R=30$) is 9.0 magnitude in the K band and 8.3 magnitude in the L band. Also, only the spectrally dispersed ABCD encoding algorithm in K and L bands can coherence the N band fringes with a maximum loss in fringe contrast of 10%. However, this sensitivity applies only for instantaneous estimation of water vapor dispersion. The feed forward sensitivity can be enhanced by averaging the water vapor content over multiple duty cycles of K and L band group delay estimation. The L band group delay estimation sensitivity can also be enhanced by coherencing the L band fringe tracking channel using K band group delay information at a faster duty cycle.

ZUSAMMENFASSUNG

Motivation:

Atmosphärische Turbulenz stellt ein Hauptproblem für das Erreichen hoher Winkelauflösungen für optische und infrarote astronomische Beobachtungen dar. Die atmosphärische Turbulenz induziert Phasenfluktuationen an den eingehenden stellaren Wellenfronten. Mit den jüngsten Fortschritten in adaptiver Optik u.A. können wir diesen Effekt minimieren und die Aberrationen der stellaren Wellenfront größtenteils beseitigen. Allerdings wird die globale Phasenverschiebung (Piston) nicht durch das adaptive Optiksyste m korrigiert. Diese spielt jedoch eine kritische Rolle in der optischen- und infrarot-Interferometrie. Die Schwankungen der optischen Wegdifferenz (OPD), induziert durch atmosphärische Turbulenzen und Vibrationen des Instruments, beeinflussen die Positionen des Interferenzmusters (Fringes) auf dem Detektor und damit die Bestimmung des Kontrasts. Somit ist ein dedizierter sogenannter Fringe Tracker zusätzlich zu einem adaptiven Optiksyste m notwendig in einem optischen- oder infrarot-Interferometer.

Die Fringes können auf zwei Arten verfolgt werden, nämlich durch Verfolgung der Gruppengeschwindigkeit und durch Verfolgung der Phasenverzögerung. Die Verfolgung der Phasenverzögerung beinhaltet die Verfolgung jeder einzelnen Fringe Phase und Gruppengeschwindigkeitsverfolgung beinhaltet das Verfolgen der Hüllenkurve. Derzeit verfügt das Very Large Telescope Interferometer (VLTI) über den Gravity Fringe Tracker, FINITO und Prima FSU, die Gruppen- und Phasenverzögerungen in den H- und K-Bändern verfolgen. Objekte wie Young Stellar Objects (YSO), staubige Tori um aktive galaktische Kerne (AGN) usw. sind jedoch bei längeren Wellenlängen, aufgrund des Vorhandenseins von umgebenden Staub, heller. In meiner Arbeit erkundige ich daher die Möglichkeit on-source Fringe Tracking im K und L Band zu realisieren. Fringe Tracking im L Band ist vorteilhaft, da hier die Kohärenzzeit der Atmosphäre länger ist und der Fried Parameter größer im Vergleich zu kürzeren Wellenlängen ist. Ich erweitere außerdem meine Arbeit auf feed-forward Gruppenverzögerung im mittleren Infrarot indem ich inter-Band Dispersion zwischen dem K und L band studiere.

Methode:

Um die Leistung eines Fringe-Trackers in den K- und L-Bändern zu analysieren, habe ich einen atmosphärischen Turbulenzsimulator (GSDim) entwickelt, der atmosphärische Wasserdampfdispersion und Instrumentenvibrationen am VLTI beinhaltet. Die simulierten OPD-Fluktuationen werden dann in simulierte, verrauschte K- und L-Fringes über unterschiedliche Integrationszeiten injiziert. Die Gruppenverzögerung

wird dann aus den resultierenden Interferenzstreifen durch die spektral verteilte ABCD-Codierungstechnik, die Methode der kleinsten Quadrate und die Doppel-Fourier-Technik geschätzt. Die Leistung und Empfindlichkeit jedes der Gruppenlaufzeitschätzalgorithmen wird dann durch Vergleichen der simulierten Eingangsgruppenverzögerung und der gemessenen Gruppenverzögerung geschätzt.

Ergebnisse:

Der Verlust im Kontrast über die Integrationszeit folgt einem zufälligen Random Walk aufgrund der zeitlichen Dekorrelation der Phasenfluktuationen an jedem Teleskop über längere Integrationszeiten (T_{int} 1,79 & t_0). Daher ist das Signal-Rausch-Verhältnis (SNR) auf dem korrelierten Fluss unzuverlässig beim Schätzen der Empfindlichkeit eines Gruppenverzögerungs-Verfolgers bei solchen Integrationszeiten. Alternativ können wir durch das quadratische Mittel (Root Mean Squared, RMS) auf die Restgruppenverzögerung für jeden Gruppenverzögerungsschätzalgorithmus die Empfindlichkeit und Leistung des Gruppenverzögerungsverfolgers gleichzeitig abschätzen. Die Schwelle für die RMS der Restgruppenverzögerung hängt jedoch von der spektralen Auflösung für die inkohärente Addition von Interferenzaufnahmen ab. Für die Studien im L-Band mit MATISSE bei niedriger spektraler Auflösung ($R = 30$) mit einem akzeptablen maximalen Verlust im Kontrast von 10% können wir eine Kohärenz mit einer K- und L-Bandsensitivität im Bereich von 13,36-14,67 und 6,64 - 10,02 Magnituden für die verschiedenen Gruppenverzögerungsschätzalgorithmen realisieren.

Durch Vergleich der individuellen Gruppenverzögerungs-Schätzfehler in den K- und L-Bändern wird die Empfindlichkeit zur Durchführung der Vorwärts-Gruppenlaufzeitverfolgung unter Verwendung von nur K- und L-Bandgruppenverzögerungsinformation für Studien im N-Band mit MATISSE bei niedriger spektraler Auflösung ($R = 30$) zu 9,0 Magnitude im K-Band und 8,3 Magnitude im L-Band bestimmt. Außerdem kann der einzige spektral verteilte ABCD-Codieralgorithmus in K- und L-Bändern die N-Band-Fringes mit einem maximalen Kontrastverlust von 10% kohärent arbeiten. Die Feed-Forward-Empfindlichkeit kann jedoch durch Mitteln des Wasserdampfgehalts über mehrere Arbeitszyklen der K- und L-Bandgruppenverzögerungsschätzung verbessert werden.

CONTENTS

| | | |
|-------|---|----|
| 1 | INTRODUCTION | 1 |
| 1.1 | Scientific motivation | 2 |
| 1.1.1 | Young Stellar Objects | 2 |
| 1.1.2 | Active Galactic Nuclei(AGN) | 6 |
| 1.1.3 | Dusty S-Cluster Object- Galactic Center | 8 |
| 1.2 | Interferometry | 9 |
| 1.2.1 | Young's double slit experiment | 9 |
| 1.2.2 | Michelson's interferometer | 9 |
| 1.2.3 | Stellar interferometry | 10 |
| 1.3 | Very Large Telescope Interferometer | 11 |
| 1.4 | Atmospheric Turbulence | 12 |
| 1.5 | Fringe Tracking | 15 |
| 1.5.1 | Phase delay tracking (Co-phasing) | 15 |
| 1.5.2 | Group delay tracking (Coherencing) | 16 |
| 1.6 | Closure Phase | 17 |
| 1.7 | Fringe tracking for infrared targets | 17 |
| 1.8 | Goals of the thesis | 18 |
| 2 | ATMOSPHERIC TURBULENCE | 20 |
| 2.1 | Kelvin-Helmholtz instability | 20 |
| 2.2 | Kolmogorov theory of Atmospheric turbulence | 21 |
| 2.2.1 | Outer scale | 23 |
| 2.2.2 | von Karman power spectrum | 24 |
| 2.3 | Numerical simulations of atmospheric turbulence | 25 |
| 2.3.1 | white noise | 25 |
| 2.3.2 | Generating random turbulence screens | 27 |
| 2.4 | Characterizing turbulent screens | 28 |
| 2.4.1 | Kolmogorov-Obhukov statistics | 28 |
| 2.4.2 | Other structure functions | 30 |
| 2.4.3 | Phase Structure function | 31 |
| 3 | GDSIM:TEMPORAL EVOLUTION OF PHASE | 36 |
| 3.1 | GDSIM | 36 |
| 3.2 | Taylor's frozen turbulence flow hypothesis | 36 |
| 3.3 | Phase Structure function | 37 |
| 3.4 | Temporal Power Spectrum | 38 |
| 3.5 | Instrumental vibration | 42 |
| 3.6 | Simulating phase/OPD fluctuation time series | 44 |

| | | |
|--------|---|-----|
| 3.7 | Variance of OPD fluctuations | 46 |
| 3.8 | Strehl Ratio - Maréchal's Approach | 49 |
| 3.9 | Deviation from Maréchal's approximation | 51 |
| 3.9.1 | Random walk model | 51 |
| 3.9.2 | Longer time scale OPD drift | 52 |
| 3.10 | Effects of atmospheric dispersion | 53 |
| 3.10.1 | water vapor refractivities | 54 |
| 3.11 | Non-Kolmogorov turbulence | 59 |
| 3.12 | Comparison with FINITO data | 60 |
| 3.13 | Birefringence | 63 |
| 4 | SIGNAL TO NOISE RATIO AND SENSITIVITY | 64 |
| 4.1 | Noise | 64 |
| 4.1.1 | Photon/Shot Noise | 64 |
| 4.1.2 | Detector Noise | 64 |
| 4.1.3 | Thermal Background | 65 |
| 4.2 | SNR on the flux of the source | 67 |
| 4.3 | SNR on the correlated flux | 68 |
| 4.4 | Noise on the measurement of phase | 69 |
| 4.5 | Noise on the group delay measurements | 70 |
| 4.6 | Simulating noisy two telescope fringes | 70 |
| 4.7 | Poisson Noise and Gaussian Noise | 73 |
| 4.8 | GRAVITY fringe tracker | 74 |
| 4.9 | MATISSE | 76 |
| 4.10 | Simulated noisy fringes | 78 |
| 4.11 | loss in fringe contrast | 79 |
| 4.12 | Phase Delay Sensitivity | 81 |
| 5 | GROUP DELAY TRACKING | 83 |
| 5.1 | ABCD on dispersed fringes | 83 |
| 5.1.1 | Dynamic range | 85 |
| 5.2 | Least Square estimation | 89 |
| 5.3 | Double Correlation | 92 |
| 5.4 | Other techniques | 95 |
| 5.4.1 | Sliding Window | 95 |
| 5.4.2 | Sliding Template | 96 |
| 6 | RESULTS AND DISCUSSION | 97 |
| 6.1 | Residual group delay | 97 |
| 6.2 | RMS on the residual group delay | 97 |
| 6.3 | Ideal integration time | 100 |
| 6.4 | Performance and Sensitivity | 102 |
| 6.5 | Incoherent stacking | 103 |

| | | |
|-----|--|-----|
| 6.6 | Coherencing with Auxiliary telescopes | 106 |
| 6.7 | Group delay tracking with resolved sources | 107 |
| 6.8 | Different vibration modes | 108 |
| 6.9 | Mid-IR feed forward group delay | 109 |
| 7 | SUMMARY AND CONCLUSION | 115 |
| 7.1 | Future work | 118 |

LIST OF FIGURES

| | | |
|-----------|--|----|
| Figure 1 | Classification of YSO (<i>Armitage, 2010</i>). | 2 |
| Figure 2 | Mass fraction of crystalline silicate grains as compared to the mass of the host (<i>Apai et al., 2005</i>) | 4 |
| Figure 3 | Spectral Energy Distribution (SED) of the brown dwarf L316 with an infrared excess and mid-infrared dip showing the existence of an inner hole. The diamonds indicate the observed photometric fluxes and the solid and dotted lines shows the best fitting model (<i>Muzerolle et al., 2006</i>) | 5 |
| Figure 4 | HD142527 observed by <i>Honda et al. (2009)</i> using Subaru telescope at 3.08 μ m wavelength | 6 |
| Figure 5 | Unified model of an AGN (<i>Beckmann & Shrader, 2012</i>) | 7 |
| Figure 6 | mid infrared SED of Dusty S-Cluster Object (DSO)/G2 with a stellar black body of $T = 4200\text{K}$ and a $T = 874\text{K}$ blackbody for the infrared thermal emission of dust (<i>Zajaček et al., 2017</i>) | 8 |
| Figure 7 | Young's Double slit experiment | 9 |
| Figure 8 | Schematic of a typical Michelson interferometer | 10 |
| Figure 9 | different baseline configurations at VLTI | 12 |
| Figure 10 | Standard shapes of wavefronts for n order and m frequency Zernike polynomials (<i>Lakshminarayanan & Fleck, 2011</i>) | 14 |
| Figure 11 | Representation of broadband fringes and fringe envelope. The green shaded region shows the region of accuracy in which the cophasing is done. The yellow region shows the accuracy in which coherencing is done. | 16 |
| Figure 12 | Comparison of K and L band magnitudes of YSOs in embedded clusters. The vertical red line shows the K band sensitivity limit of Gravity fringe tracker. The horizontal green and yellow dashed lines shows the L band sensitivity of MATISSE operating without and with an external fringe tracker respectively. The green and yellow shaded region contains targets which are too faint to be detected with Gravity fringe tracker in the K band but are bright enough to be detected by MATISSE without and with an external fringe tracker respectively | 18 |
| Figure 13 | Power spectrum of a laboratory turbulence (<i>Champagne, 1978</i>) | 25 |
| Figure 14 | Sample random white noise over time | 25 |
| Figure 15 | Distribution of the values in the random white noise | 26 |
| Figure 16 | Power spectrum of the random white noise | 26 |
| Figure 17 | initial conditions for generating a Kolmogorov turbulence screen on refractive index | 27 |
| Figure 18 | A random realization of Kolmogorov turbulence screen on refractive index | 28 |

| | | |
|-----------|--|----|
| Figure 19 | Structure function estimated from the Kolmogorov screen (fig. 18a) and the analytical fit given by eq. 39. We see a divergence between the analytical and the numerical correlation functions at a distance of $0.26\times$ box size. This is mainly computational issue due to the limited box size of the simulated refractive index screen. | 30 |
| Figure 20 | Wind velocity as a function of height at Antofagasta base during the month of July | 34 |
| Figure 21 | Comparison of the three C_n^2 models | 34 |
| Figure 22 | Turbulence strength measured at Cerro Paranal, Chile (Quirrenbach, 2014) | 35 |
| Figure 23 | Description of a Kolmogorov turbulent screen blown over a telescope aperture with a specific wind velocity (v) | 37 |
| Figure 24 | Temporal power spectrum of an interferometer with baseline of 80 meters and wind velocity of 10m/s | 39 |
| Figure 25 | Power spectra of OPD fluctuations measured on Mark III interferometer at Mt.Wilson (Buscher et al., 1995). Both the observations were done at 31.5 meter baseline, but on different observing nights. The effect of the outer scale is clearly visible below 0.1 Hz. On the left plot, the $-2/3$ asymptotic behavior characteristic of the Kolmogorov model is clearly noticeable. On the right plot, the outer scale of that night was smaller and a flat behavior of the power spectrum with a 0 exponent is visible. . | 40 |
| Figure 26 | Representation of the Taylor's frozen turbulence flow over an interferometer with 8 meter apertures and a baseline $B = 80\text{m}$ | 41 |
| Figure 27 | Temporal power spectrum of OPD fluctuations derived with Taylor's frozen turbulence hypothesis compared with the analytical power spectrum. The entire signal was simulated for 18.63 seconds with a 10m/s wind speed | 41 |
| Figure 28 | OPD fluctuation power spectrum due to instrumental vibrations at Unit Telescopes (UT)1-UT2 with a total vibration $\sigma_{\text{OPD,vib}} = 300\text{nm}$ | 43 |
| Figure 29 | Simulated OPD time-series for an 80 meter baseline including both atmospheric turbulence and instrumental vibrations of UT1-UT2 combination | 45 |
| Figure 30 | power spectrum of simulated OPD time-series shown in fig. 29 | 45 |
| Figure 31 | OPD time-series simulated by Choquet et al. (2014) for a 100m baseline including instrumental vibrations at VLTI | 45 |
| Figure 32 | Standard deviation of OPD fluctuation in an interferometer as a function of baseline, model of turbulence and outer scale | 47 |

| | | |
|-----------|---|----|
| Figure 33 | Filtered and unfiltered Kolmogorov temporal power spectrum for a baseline of 80 meters and integration time of 1 second. The orange dashed curve shows the filter function for a box width of one second. The solid blue curve shows a typical Kolmogorov power spectrum. The green dashed dotted lines shows the filtered Kolmogorov power spectrum. | 48 |
| Figure 34 | Growth of σ_{OPD} over integration time estimated in both temporal and power spectral domain. | 48 |
| Figure 35 | Maréchal's approximation of the loss in visibility amplitude due to atmospheric turbulence of a spatially unresolved source in the K band at a baseline of 80 meters. | 51 |
| Figure 36 | Loss of visibility amplitude due to Maréchal (analytical) approximation and random walk model with simulated numerical K band broadband fringe contrast loss | 52 |
| Figure 37 | Dry air and water vapor temporal power spectral densities measured at Keck interferometer at a baseline of 82meters (Colavita, 2010). The upper curves are for dry air and the lower curves are water vapor fluctuations | 57 |
| Figure 38 | Simulated differential water vapor column density fluctuations between two arms of an interferometer separated by a baseline of 80m | 58 |
| Figure 39 | Measured water vapor differential column density fluctuations at Keck interferometer (Koresko et al., 2006) on a relatively larger humidity as compared to the observation of Masson (1994). | 58 |
| Figure 40 | design layout of FINITO fringe tracker at VLT (Gai et al., 2004) | 60 |
| Figure 41 | H band closed-loop group delay measurements of 31Ori measured with FINITO fringe tracker at VLT | 61 |
| Figure 42 | H band closed-loop group delay measurements of α -Tau measured with FINITO fringe tracker at VLT | 61 |
| Figure 43 | Normalized power spectrum of group delay fluctuations shown in fig. 41. | 62 |
| Figure 44 | Normalized power spectrum of group delay fluctuations shown in fig. 42. | 62 |
| Figure 45 | Thermal background for Paranal, Chile (Absil et al., 2006) | 65 |
| Figure 46 | Thermal background structure function measured at VLT using MIDI data (Matter et al., 2016) | 66 |
| Figure 47 | Evolution of simple SNR_{flux} over time for a 6th magnitude star | 68 |
| Figure 48 | Evolution of simplified SNR_c over integration time using the simulated numerical fringe contrast | 69 |
| Figure 49 | Poisson distributions centered around 0.5, 3.0 and 10.0 | 73 |
| Figure 50 | Integrated optics beam combiner of Gravity instrument at VLT (Gravity Collaboration et al., 2017) | 74 |
| Figure 51 | Sample Gravity fringe tracker image | 75 |
| Figure 52 | left: Layout of the Hawaii-2RG detector. right: Sample 4 telescope L band interferometric fringes. (Millour et al., 2016) | 77 |

| | | |
|-----------|--|----|
| Figure 53 | Sample K band noisy fringes for a 8th magnitude source with an integration time of 10ms | 78 |
| Figure 54 | Sample L band noisy fringes for a 8th magnitude source with an integration time of 10ms | 78 |
| Figure 55 | Simulated dispersed fringes ($R=500$) for an unresolved source of 5th magnitude in the L band. | 79 |
| Figure 56 | Simulated dry air OPD time-series for a baseline of 80 meters and wind velocity of 10m/s | 79 |
| Figure 57 | K band interferometric fringes of an unresolved source of 8th magnitude, aberrated by the simulated OPD disturbance shown in fig.56 for an integration time of 1 second | 80 |
| Figure 58 | Loss in fringe contrast over 1 second of integration of fringes shown in fig.57 | 80 |
| Figure 59 | Comparison of observed loss in visibility amplitude for 200 millisecond integration time with UT1-UT3 combination of VLTI with the simulated loss of visibility amplitude for a 100 meter baseline | 81 |
| Figure 60 | SNR_c vs K band magnitude for an integration time of 100ms for Gravity fringe tracker setup. The black horizontal line marks the threshold of $SNR_c = 4$ | 82 |
| Figure 61 | SNR_c vs L band magnitude for an integration time of 100ms for MATISSE L band low spectral resolution ($R=30$) setup. The black horizontal line marks the threshold of $SNR_c = 4$ | 82 |
| Figure 62 | Description of the ABCD fringe encoding | 83 |
| Figure 63 | absolute value of the Discrete Fourier Transform (DFT) described in eq. 120 for a 5th magnitude star in the K band with a group delay of $-8\mu m$ | 85 |
| Figure 64 | K band simulated and measured group delay time series using ABCD algorithm on dispersed fringes in the K band for an unresolved source with 10th magnitude and an integration time of 100ms | 87 |
| Figure 65 | L' band simulated and measured group delay time series using ABCD algorithm on dispersed fringes in the L band for an unresolved source with 7th magnitude and an integration time of 100ms | 87 |
| Figure 66 | Comparison of the input and measured K band group delay of the time series shown in fig. 64 | 88 |
| Figure 67 | Comparison of the input and measured L' band group delay shown in fig. 65 | 88 |
| Figure 68 | Sample K band simulated noisy broad band fringe of an unresolved source at 10th magnitude with a delay of $-11\mu m$ fitted with the model | 90 |
| Figure 69 | Simulated input and measured group delay in K band using noisy fringes of a 10th magnitude unresolved source with 100ms integration using the least squares technique | 90 |

| | | |
|-----------|---|-----|
| Figure 70 | <i>Simulated input and measured group delay in L' band using noisy fringes of a 5th magnitude unresolved source with 100ms integration using the least squares technique</i> | 91 |
| Figure 71 | <i>Comparison of K band input and measured group delay from the time series shown in fig. 69</i> | 91 |
| Figure 72 | <i>Comparison of L' band input and measured group delay from the time series shown in fig. 70</i> | 92 |
| Figure 73 | <i>Input and measured group delay time series with synthetic noisy fringes of an unresolved K band source at 10th magnitude</i> | 93 |
| Figure 74 | <i>Input and measured group delay time series with synthetic noisy fringes of an unresolved L' band source at 5th magnitude</i> | 94 |
| Figure 75 | <i>Comparison of the input and the measured group delay in K band shown in fig. 73. The black diagonal line shows the ideal case where input group delay = measured group delay</i> | 94 |
| Figure 76 | <i>Comparison of the input and the measured group delay in L' band shown in fig. 76. The black diagonal line shows the ideal case where input group delay = measured group delay</i> | 95 |
| Figure 77 | <i>Sample residual group delay estimated with the least square algorithm with a K band unresolved source of 10th magnitude at an integration time of 100ms</i> | 97 |
| Figure 78 | <i>RMS of the residual group delay in the K band for a Gravity fringe tracker with 100ms integration time set up for one random realization of the atmospheric turbulence</i> | 98 |
| Figure 79 | <i>RMS on the residual group delay in the K band with Gravity fringe tracker setup for different stellar magnitudes at 100ms integration time</i> | 99 |
| Figure 80 | <i>RMS on the residual group delay in the L' band with Matisse L band setup for different stellar magnitudes at 100ms integration time</i> | 99 |
| Figure 81 | <i>Comparison of RMS on the residual group delay for 100ms and 700ms integration time with different group delay estimation techniques in the K band</i> | 101 |
| Figure 82 | <i>Comparison of RMS on the residual group delay for 100ms and 2.1 seconds integration time with different group delay estimation techniques in the L' band</i> | 102 |
| Figure 83 | <i>RMS on the residual group delay in K band for a Gravity fringe tracker set up for 100ms integration time for different stellar magnitudes. The horizontal black line shows the $3.25\mu\text{m}$ threshold for MATISSE L band science at low spectral resolution ($R=30$). The vertical black dotted line shows the 10th magnitude phase delay tracking limit of Gravity Fringe tracker in the K band.</i> | 105 |

| | | |
|-----------|--|-----|
| Figure 84 | <i>RMS on the residual group delay in the L' band for MATISSE L band set up for 100ms integration time for different stellar magnitudes. The horizontal black line shows the $3.25\mu\text{m}$ threshold for MATISSE L band science at low spectral resolution ($R=30$)</i> | 105 |
| Figure 85 | <i>RMS on the residual group delay measured in K and L' bands with a Gravity fringe tracker and MATISSE L band setup at 100ms integration time with the Auxiliary Telescopes (AT)s at a baseline of 80 meters. The vertical black dotted line shows the K=7 phase delay sensitivity limit of the Gravity fringe tracker with ATs.</i> | 107 |
| Figure 86 | <i>RMS on the residual group delay in the K band with a spatially resolved phase reference. The vertical black dotted line shows the 10th magnitude phase delay sensitivity limit of Gravity fringe tracker with the UTs. . .</i> | 108 |
| Figure 87 | <i>RMS on the residual OPD at K and L bands for high vibration levels with UT1-UT2 combination with $\sigma_{\text{OPD,vib}} = 411\text{nm}$. Estimated on a spatially unresolved source ($v = 1$). The black vertical dotted line shown in the left figure shows the 10th magnitude phase delay tracking sensitivity of Gravity fringe tracker with UTs! (UTs!)</i> | 109 |
| Figure 88 | <i>Errors on estimation of Σ_{vv} using K and L band group delay</i> | 112 |
| Figure 89 | <i>Error on the feed-forward group delay at N band estimated using K and L band group delay estimation errors</i> | 112 |
| Figure 90 | <i>Decision tree for an efficient way to perform coherencing and cophasing at mid-infrared using K and L band group and phase delays.</i> | 114 |
| Figure 91 | <i>Comparison of K and L magnitudes of class 1 YSOs in embedded clusters with the new group delay sensitivity limits estimated by this work . . .</i> | 116 |
| Figure 92 | <i>Comparison of K and L magnitudes of class 2 YSOs in embedded clusters with the new group delay sensitivity limits estimated by this work . . .</i> | 117 |

LIST OF TABLES

| | | |
|----------|---|-----|
| Table 1 | OPD RMS induced by instrumental vibrations of the UTs at VLTI (<i>Mérand et al., 2012</i>) | 43 |
| Table 2 | vibration model parameters (<i>Choquet et al., 2014</i>) | 44 |
| Table 3 | Ideal gas parameters for dry air and water vapor during the observation of <i>Colavita et al. (2004)</i> | 54 |
| Table 4 | Specific refractivities of dry air and water vapor at infrared wavelengths | 55 |
| Table 5 | Power spectral parameters for water vapor and dry air measured at the Keck Interferometer at a baseline of 82 meters and a wind velocity of 10m/s (<i>Colavita, 2010</i>) | 57 |
| Table 6 | Input parameters used in simulating K and L band fringes | 71 |
| Table 7 | L band sensitivity (in magnitudes) of MATISSE without an external fringe tracker (<i>Matter et al., 2016</i>) | 77 |
| Table 8 | K and L band sensitivity in estimating group delay for coherencing science fringes in the L band with MATISSE at low spectral resolution | 106 |
| Table 9 | K and L band sensitivity in estimating group delay with ATs for coherencing science fringes in the L band with MATISSE at low spectral resolution | 107 |
| Table 10 | K band group delay sensitivity by using a spatially resolved phase reference | 108 |
| Table 11 | K and L band sensitivity in estimating group delay for coherencing science fringes at high vibration level (411nm) in the L band with MATISSE at low spectral resolution | 109 |

ACRONYMS

| | |
|------|-------------------------------------|
| PSF | Point Spread Function |
| GTC | Gran Telescope Canarias |
| LBT | Large Binocular Telescope |
| VLT | Very Large Telescope |
| HET | Hobby Eberly Telescope |
| GMT | Giant Magellan Telescope |
| EELT | European Extremely Large Telescope |
| TMT | Thirty Meter Telescope |
| LSST | Large Synoptic Survey Telescope |
| AU | Astronomical Unit |
| MCF | Mutual Coherence Function |
| AO | Adaptive Optics |
| EM | Electro Magnetic |
| IO | Integrated Optics |
| GLS | Gallium Lanthanum Sulphide |
| OPD | Optical Path Difference |
| VLTI | Very Large Telescope Interferometer |
| UT | Unit Telescopes |
| AT | Auxiliary Telescopes |
| YSO | Young Stellar Objects |
| SED | Spectral Energy Distribution |
| AGN | Active Galactic Nuclei |

| | |
|--------|---|
| SMBH | Super Massive Black Hole |
| DSO | Dusty S-Cluster Object |
| GSM | Generalised Seeing Monitor |
| RMS | Root Mean Squared |
| PTI | Palomar Testbed Interferometer |
| ABL | Atmospheric Boundary Layer |
| PBL | Planetary Boundary Layer |
| FINITO | Fringe-tracking Instrument of Nice and TOrino |
| SNR | Signal to Noise Ratio |
| CCD | Charge Coupled Device |
| APD | Avalanche Photo Diode |
| DFT | Discrete Fourier Transform |
| IOTA | Infrared Optical Telescope Array |
| SPH | Smoothed Particle Hydrodynamics |

INTRODUCTION

High angular resolution and high sensitivity is the major desire for every astronomical observation. This has been a driving force for development in Astronomical instrumentation. This fueled innovations such as long baseline interferometry, adaptive optics, large segmented primary mirrors using active optics, etc. Resolution is defined as the ability to separate two objects or sources of light into two separate Point Spread Function (PSF). Resolution limit of an astronomical telescope with a primary mirror diameter D observing at a wavelength λ is given by,

$$\Theta = 1.22 \frac{\lambda}{D} \quad (1)$$

The current pathway for Astronomical instrumentation is striving in achieving higher resolutions by implementing new technologies on producing larger primary mirrors. Current large scale telescope such as Gran Telescope Canarias (GTC), Large Binocular Telescope (LBT), Very Large Telescope (VLT), Hobby Eberly Telescope (HET), Keck, Gemini, Giant Magellan Telescope (GMT), etc. have pushed the sensitivity and resolution higher with technologies such as Multi-Conjugate and extreme adaptive optics, active optics, etc. This has paved the way to future telescopes such as European Extremely Large Telescope (EELT), Thirty Meter Telescope (TMT), Large Synoptic Survey Telescope (LSST), etc., which will further push the boundaries on the sensitivity and resolution of Astronomical observations.

However, we can still push the boundary of resolution by using Stellar Interferometers. Combining the light received by two telescopes separated by a baseline B , we can achieve a resolution of,

$$\Theta = 1.22 \frac{\lambda}{B} \quad (2)$$

Observing astronomical targets at high angular resolutions gives us more detailed information about the morphology of the objects and the physical and chemical processes involved to a greater detail.

1.1 SCIENTIFIC MOTIVATION

1.1.1 *Young Stellar Objects*

Young Stellar Objects (YSO) are young stars and their surrounding material (dusty envelope, protoplanetary disk, etc.), which are a few million years old. These objects are the perfect laboratories in understanding the processes of star and planet formation. YSO environment consists of mainly of dust and gas. These two components play a key role in the star and planet formation.

Due to the dusty nature of YSOs, they are brighter at near and mid- infrared wavelengths. Their Spectral Energy Distribution (SED) shows an excess at these wavelengths when compared to the stellar blackbody SED. YSOs can be classified based on the slope of the SED at infrared wavelengths (Lada & Wilking, 1984). They are classified as,

- **Class 0:** Protostars with a collapsing envelope around.
- **Class 1:** Protostars with a collapsing envelope and a newly forming disk around.
- **Class 2:** Protostars with an active accretion disk (Protoplanetary disk) around them.
- **Class 3:** Protostars having weaker disks around them with very low or no accretion.

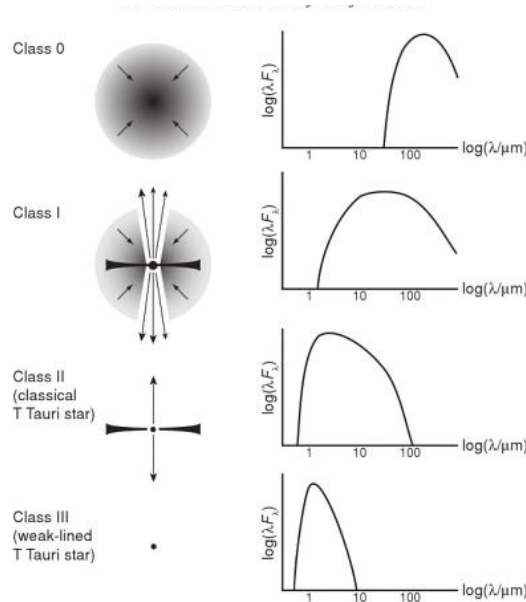


Figure 1: *Classification of YSO (Armitage, 2010).*

To understand the physical and chemical processes involved with formation of planets, we need to understand the nature of dust and gas in Class 2 YSOs (Protoplanetary disks).

Brown dwarf transitional disks

Brown dwarfs are sub-stellar objects whose mass is $\leq 0.8M_{\odot}$ (Kumar (1963), Hayashi & Nakano (1963)). Due to their low masses they fail to start Hydrogen burning thus ending up being a failed star (sub-stellar object). Circumstellar material around young brown dwarf disks were first discovered through excess in the H-K colors (Luhman (1999), Muench et al. (2001)) hinting the existence of planet formation around brown dwarfs. Various Smoothed Particle Hydrodynamics (SPH) simulations of dust particles around brown dwarf protoplanetary disks have shown that dust grains can efficiently move radially inwards forming a high density inner region with an exponential surface density cut-off as compared to T-Tauri disks (Pinilla et al., 2013).

Due to the low flux from the primary brown dwarf in optical wavelengths, exoplanets around brown dwarfs can only be discovered at near- & mid-infrared through microlensing events. Han et al. (2017) was the first to discover a $1.9 \pm 0.2M_J$ (Jupiter mass) at a distance of 0.87 Astronomical Unit (AU) around a $0.022M_{\odot}$ (Solar mass) brown dwarf using microlensing events. The host to planet mass ratio of 0.08 ± 0.001 shows that the planet may have formed in a protoplanetary disk. Similar planet to host mass ratio has been identified by other microlensing discoveries (Mróz et al., 2017). Mohanty et al. (2013) analyzed the brown dwarf and disk masses of a large sample of M dwarfs and Brown dwarfs and concluded that the typical disk to stellar mass ratio of such systems is 3.98×10^{-3} . This is in the order of magnitude of the observed host to planet ratio, which implies highly efficient planet formation mechanism on the disk. This is in line with the SPH simulations of Pinilla et al. (2013) where the dust efficiently moves radially inwards of the disk which creates a high density region of dust particles. Apai et al. (2005) observed a strong presence of crystalline silicates in a sample of brown dwarf protoplanetary disks using low resolution spectroscopic instrument on the Spitzer space telescope. This shows that the protoplanetary disk around brown dwarfs have similar planet formation mechanism as that of T-Tauri and Herbig systems. However, the dust accumulation of Pinilla et al. (2013) and the relatively cooler disk, shows us that these dust grains can efficiently settle down at the mid-plane of the disk accelerating the planet formation mechanisms.

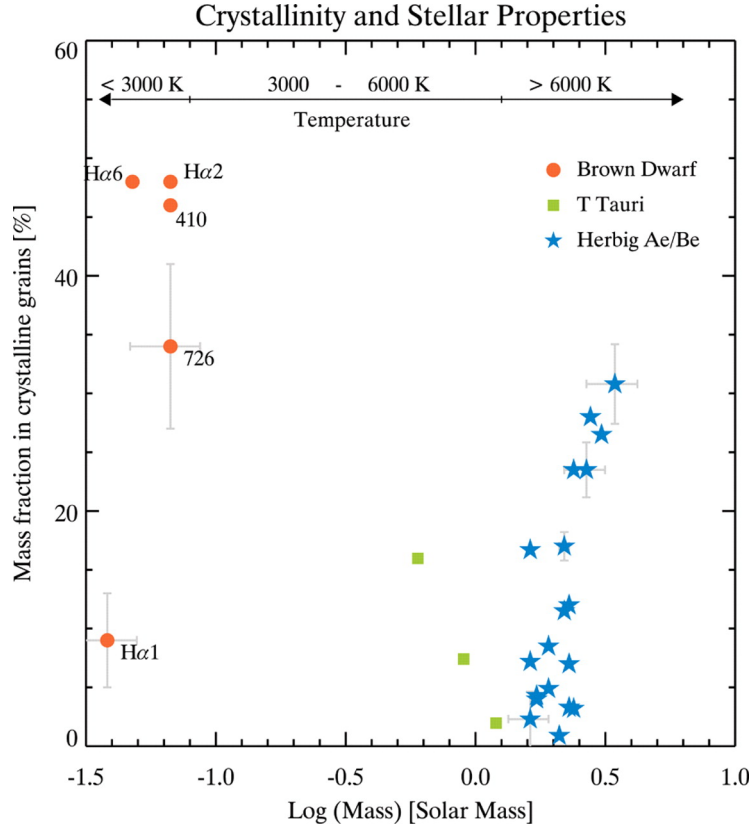


Figure 2: *Mass fraction of crystalline silicate grains as compared to the mass of the host (Apai et al., 2005)*

Thus to complete the picture of planet formation around brown dwarfs, we need to analyze transitional disks around brown dwarfs, which are the intermediate stage between a protoplanetary disk and a planetary system. Transitional disks usually exhibit inner hole, gap or a cavity on their density distribution which indicates an ongoing planet formation. Due to the relatively low flux and cooler temperatures of the brown dwarf protoplanetary disks, these features are best observed at near and mid-infrared wavelengths (Typically L, M and N bands). Transitional disks around brown dwarfs have been earlier identified through analysis of their SED (Muzerolle et al. (2006), Luhman et al. (2007), Dawson et al. (2013)). The lack of excess emission at mid-infrared wavelengths (typically 5 – 8 μ m) shows the presence of an inner hole or a gap indicating an ongoing planet formation. Fig. 3 shows the SED of the first ever brown dwarf protoplanetary disk to be found with an inner hole (Muzerolle et al., 2006).

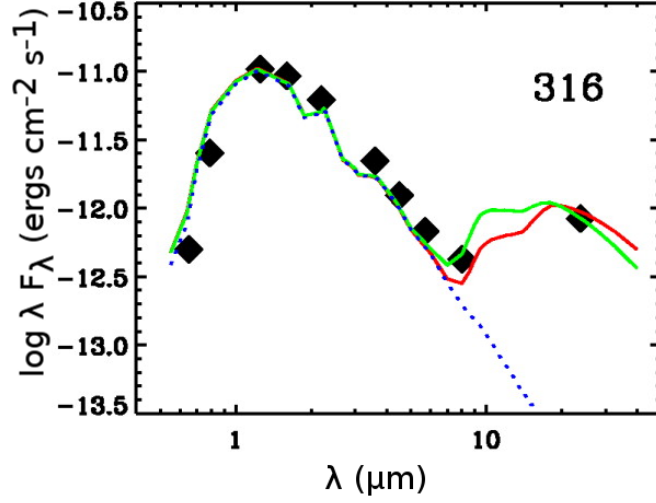


Figure 3: SED of the brown dwarf L316 with an infrared excess and mid-infrared dip showing the existence of an inner hole. The diamonds indicate the observed photometric fluxes and the solid and dotted lines shows the best fitting model (Muzerolle et al., 2006)

However, the main limitation with SED analysis is its degeneracy. Hence, it is difficult to measure the inner hole properties accurately. Alternatively, we can analyze the properties of the inner hole of the brown dwarf protoplanetary disk at high angular resolution using future mid-infrared beam combiners such as MATISSE at Very Large Telescope Interferometer (VLTI) with an external dedicated near+mid infrared fringe tracker. This enhances the sensitivity and the spatial resolution as compared to the previous mid- and far-infrared observations of such brown dwarf transitional disks.

Water ice on protoplanetary disks

One of the key molecules which plays a significant role in the process of planet formation is water ice. Water ice exists as mantles on dust grains in the disk. They help in the process of dust coagulation as they are more efficient in sticking with other grains with icy mantles through the Van der Waals force. It also adds on to the solid material accumulated through the coagulation of dust grains. Hence, the presence of water molecules plays a key role in the formation of rocky planets.

Water ices can be detected in the near infrared through their absorption feature in the L band ($3.08\mu\text{m}$). Honda et al. (2009) observed the regions of water ices on face-on Herbig Ae protoplanetary disk HD142527 through the Subaru telescope in Hawaii. By measuring the spectrum of the correlated flux of various targets using large baseline interferometers such as VLTI at the L' band ($3.5 - 4\mu\text{m}$), we can estimate the snowline of

water ices with a higher spatial resolution over a range of protoplanetary disks. This will help us understand the formation of rocky planets better.

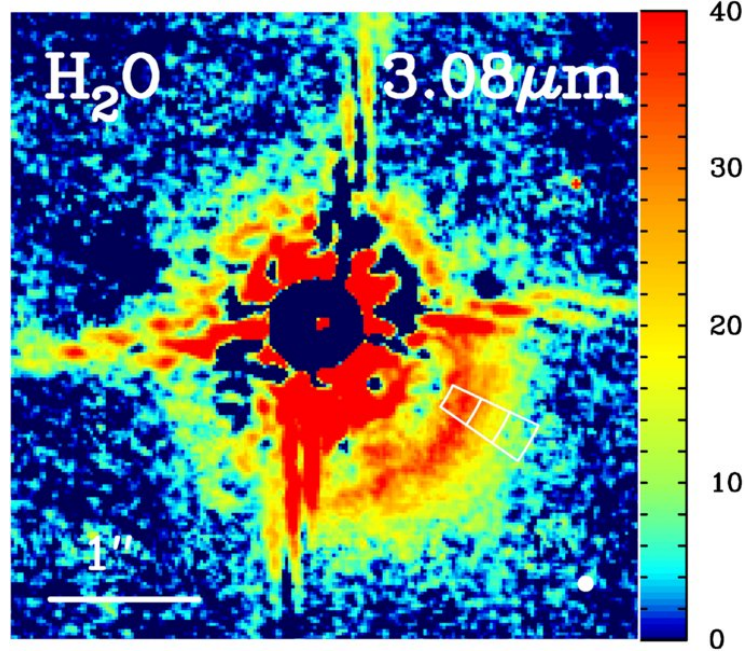


Figure 4: *HD142527* observed by *Honda et al. (2009)* using Subaru telescope at $3.08\mu\text{m}$ wavelength

1.1.2 Active Galactic Nuclei(Active Galactic Nuclei (AGN))

Most of the galaxies have a bright and compact core called as AGN which outshines the brightness of the galaxy. These AGNs are powered by the Super Massive Black Hole (SMBH) which feeds on the material around the AGN. The unified model of AGN as shown in fig. 5, consists of a central SMBH of $\sim 10^6 M_{\odot}$ having an accretion disk around it. The accretion disk is then surrounded by the broad line & narrow line region and a dusty torus.

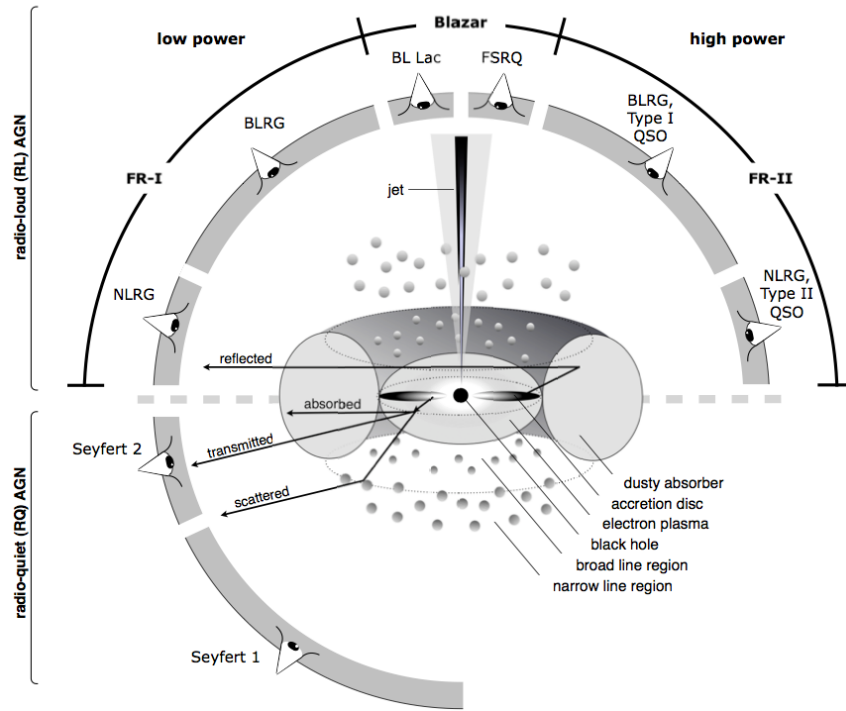


Figure 5: Unified model of an AGN (Beckmann & Shrader, 2012)

Dusty Torus

One of the major feeders of the central SMBH of an AGN is the dusty torus. The dusty torus is a key feature which separates the dichotomy between the type 1 and type 2 Seyfert galaxies. However, the nature and origins of the dusty torus around AGN is still not completely clear. The apertures of the single dish ground based telescopes are not sufficiently large enough to resolve the dusty torus to understand its morphology. However, long baseline interferometers at near- and mid-infrared wavelengths can achieve the required resolution of a few milli-arcseconds.

The VLTI/MIDI AGN Large Program Bartscher et al. (2013) cataloged the correlated flux and visibilities of the dusty torus around 23 AGNs. Observations made by Tristram et al. (2007) of the AGN environment with MIDI at VLTI showed that the central region is a thick and a torus like dusty structure around the center of Circinus galaxy. However, some of the data collected by Tristram et al. (2007) showed that the dusty torus could also be clumpy in nature. Bartscher & Tristram (2013) realized that the morphology of the dusty torus differs for different galaxies and doesn't follow the dependency of the viewing angles. Hence, a more analysis of the dusty torus around AGN using near and mid-IR interferometry can help us to understand its structure to a greater detail.

1.1.3 Dusty S-Cluster Object- Galactic Center

The center of Milky way is an excellent laboratory to understand the nature of active galactic nuclei. Galactic center harbors sources where a significant near-infrared excess has been detected (Gillessen et al., 2012). These objects are termed as Dusty S-Cluster Object (DSO) (Eckart et al., 2013) due to their dust emission and near-infrared excess. One of the most studied object is the DSO/G2, which has been proposed to be a YSO with a protoplanetary disk (Trani et al., 2016). Zajaček et al. (2017) predicts that the DSO/G2 source should belong to the class 1 category of YSO. Fig. 6 shows the mid-infrared part of the DSO/G2 SED fitted with a blackbody of 4200K for the stellar component and a 874K blackbody fit for the interferometric fluxes (Zajaček et al., 2017).

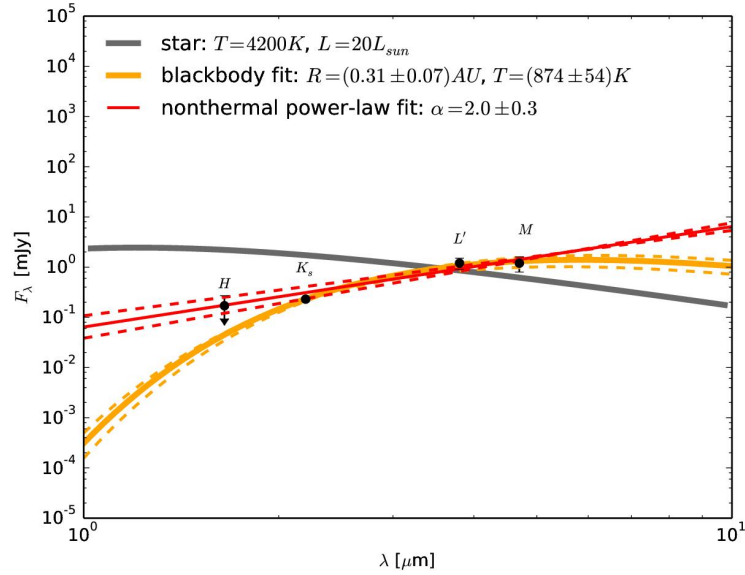


Figure 6: mid infrared SED of DSO/G2 with a stellar black body of $T = 4200\text{K}$ and a $T = 874\text{K}$ blackbody for the infrared thermal emission of dust (Zajaček et al., 2017)

The dusty environment around the DSO/G2 is still unresolved. Hence, with large baseline interferometric measurements in the near- & mid-infrared wavelengths we can estimate the nature of the protoplanetary disk around DSO/G2 source. This will further improve our understanding on planet formation around such dynamic environments.

The flux of DSO/G2 in the K band is 0.23 mJy (16.08 magnitude) (Shahzamanian et al., 2016) and 1.2 mJy (13.28 magnitude) in the L' band (Gillessen et al., 2012). Thus these objects need a dedicated near and mid-infrared fringe tracker aided interferometric observations to achieve such high sensitivities required.

1.2 INTERFEROMETRY

The principle of interferometry was first demonstrated by Thomas Young in 1802. The fundamental principle behind the experiment is the Fresnel-Huygens principle of propagation of electro-magnetic waves.

1.2.1 Young's double slit experiment

The Young's experiment involves in uniformly illuminating a screen with two narrow pinholes of diameter d , separated by a baseline B . The spherical wave-fronts emanating from the pinholes interfere and produce alternating bright and dark bands on the detector as shown in fig. 7. The alternating bright and dark bands is called inteferometric fringes.

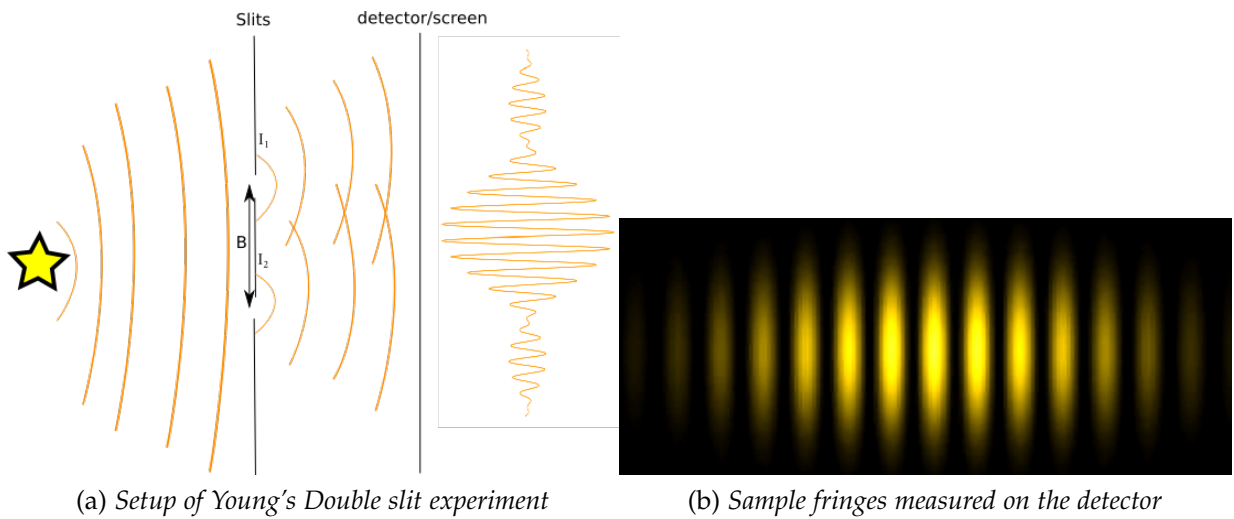


Figure 7: Young's Double slit experiment

The intensity pattern of two interfering monochromatic spherical wave-fronts of intensities I_1 and I_2 , a phase difference of $\Delta\phi = \phi_1 - \phi_2$ is,

$$I = I_1 + I_2 + 2\sqrt{I_1 I_2} \cos(\phi) \quad (3)$$

1.2.2 Michelson's interferometer

Michelson's interferometer is an alternative technique for combining wavefronts to form interferometric fringes. On contrary to the Young's double slit experiment which

combines the incoming beam on the image plane, the Michelson's interferometer combines the incoming beam on the pupil plane. This is achieved by a combination of two plane mirrors separated by a beam splitter on which the Optical Path Difference (OPD) can be applied by modulating the position of one of the mirrors. This is shown in fig. 8, where the OPD is modulated with the mirror M_1 .

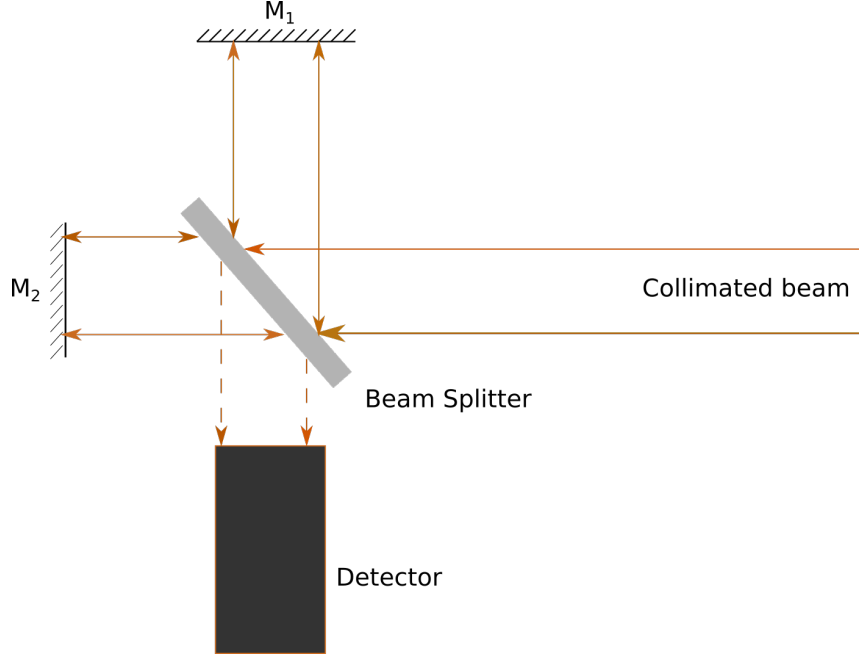


Figure 8: Schematic of a typical Michelson interferometer

The interferometric fringes can be then recorded by modulating M_1 with the corresponding OPD.

1.2.3 Stellar interferometry

To understand the advantages of using interferometry for astronomical observations, we need to first understand the property of coherence. Two waves are said to be coherent if they have a constant phase difference (spatial coherence) and the same frequency (temporal coherence). This property is important for astronomy as it sets the condition for a stable set of interferometric fringes.

The Mutual Coherence Function (MCF) of two wave-fronts (\hat{I}_1, \hat{I}_2) is defined as,

$$\Gamma(x, t) = \langle \hat{I}_1(x_1 + x, t + \tau) \hat{I}_2^*(x_1, t) \rangle \quad (4)$$

where,

$$\hat{I}_1 = I_1 e^{-i\phi_1}$$

$$\hat{I}_2 = I_2 e^{-i\phi_2}$$

The complex visibility of the astronomical source is defined as the Fourier transform of the object intensity distribution (Van Cittert-Zernike Theorem) (Zernike, 1938). Thus the complex visibility can be computed by normalizing the MCF by the intensities of the wave-front

$$\mu = \frac{\Gamma(x, t)}{I_1 I_2} \quad (5)$$

In the case of optical and infrared interferometry, it is hard to estimate the MCF as the frequencies are high as compared to the available computer clock rates. Hence, the fringe visibility amplitude is computed from the fringe intensities in equation 3 by,

$$V = \frac{I_{\max} - I_{\min}}{I_{\max} + I_{\min}} \quad (6)$$

For an unresolved astronomical source which has high spatial coherence, the value of V will be 1. For a super resolved astronomical source the value of V will be close to 0. Hence, it is easier to measure the coherence of the source through the visibility amplitude.

1.3 VERY LARGE TELESCOPE INTERFEROMETER

VLTI is a long baseline optical/infrared interferometer consisting of 4 Unit Telescopes (UT) of 8.2 meters in diameter with baselines ranging between 47m – 130m and 4 Auxiliary Telescopes (AT) of 1.8 meters and baselines ranging between 8m – 200m. Fig.9 shows the different baseline configurations of the UTs and ATs.

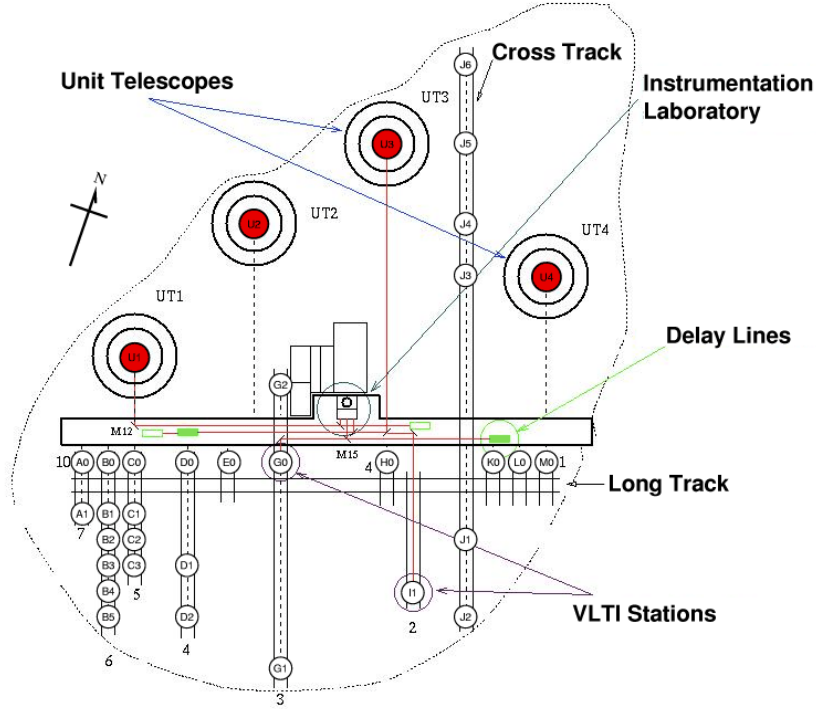


Figure 9: different baseline configurations at VLT

Instruments currently on board of the VLT are,

- AMBER: 3 telescope, near infrared instrument operating in J, H and K band. (Petrov et al., 2007)
- PIONEER: 4 telescope Integrated Optics (IO) based beam combiner operating in the H band. (Benisty et al., 2009)
- GRAVITY: 2nd generation 4 telescope IO based beam combiner operating in the K band with dedicated fringe tracker. (Gravity Collaboration et al., 2017)

1.4 ATMOSPHERIC TURBULENCE

Another important parameter of measurement in stellar interferometry to consider is the phase of the incoming wave-front. In the case of optical and infrared observations, the Earth's Atmosphere plays a key role in the propagation of light. Turbulence in the atmosphere arises due to climatic variations of temperature and pressure which causes fluctuations in the optical densities of the medium. These fluctuations results in a change in the path length and thus the phase of the incoming wave-front. The physical and analytic treatment of the Atmospheric turbulence will be discussed in detail in

Chapters 2 & 3.

These phase fluctuations can be characterized by the Zernike Polynomials (Noll, 1976). Zernike polynomials categorizes various optical aberrations that are caused due to atmospheric turbulence. The zernike polynomials has two components, the radial component $R(r)$ and the angular component Θ . The polynomials is then divided into n orders and m frequencies.

$$Z_{\text{even}}(r, \Theta) = \sqrt{n+1} R_n^m(r) \sqrt{2} \cos(m\Theta) \quad (7)$$

$$Z_{\text{odd}}(r, \Theta) = \sqrt{n+1} R_n^m(r) \sqrt{2} \sin(m\Theta) \quad (8)$$

Equations 7 & 8 are odd and even functions respectively and is only for non-zero frequencies ($m \neq 0$). At $m = 0$ the polynomial is given by,

$$Z(r) = \sqrt{n+1} R_n^0(r) \quad (9)$$

Fig. 10 shows the standard shapes of different orders and frequency Zernike polynomials .

Most of the aberrations on the incoming stellar wave-front can be corrected by using Adaptive Optics (AO) and spatial filters. AO system measures the phase errors on the incoming wave-front through a wave-front sensor, which then estimates the weights of each Zernike component. A wave-front model is then computed based on the Zernike modes. A deformable mirror then takes the negative shape of the wave-front model, which after reflection corrects for the shape of the wavefront and thus resulting in a plane wave.

Another alternative is to use spatial filters. The most effective and commonly used spatial filters in stellar interferometry are single mode fibers. An optical fibre typically consist of a core with a high optical density (high refractive index) and a cladding with a relatively lower optical density. When an Electro Magnetic (EM) wave is passed through an optical fibre, the wave is guided through the core by total internal reflection. The waveguides have a discrete set of spatial distributions of the EM wave that can be guided. This is called the mode of the wave guide. The mode of a waveguide can also be defined as the spatial pattern of the EM field. A single mode fibre has only one mode of propagation.

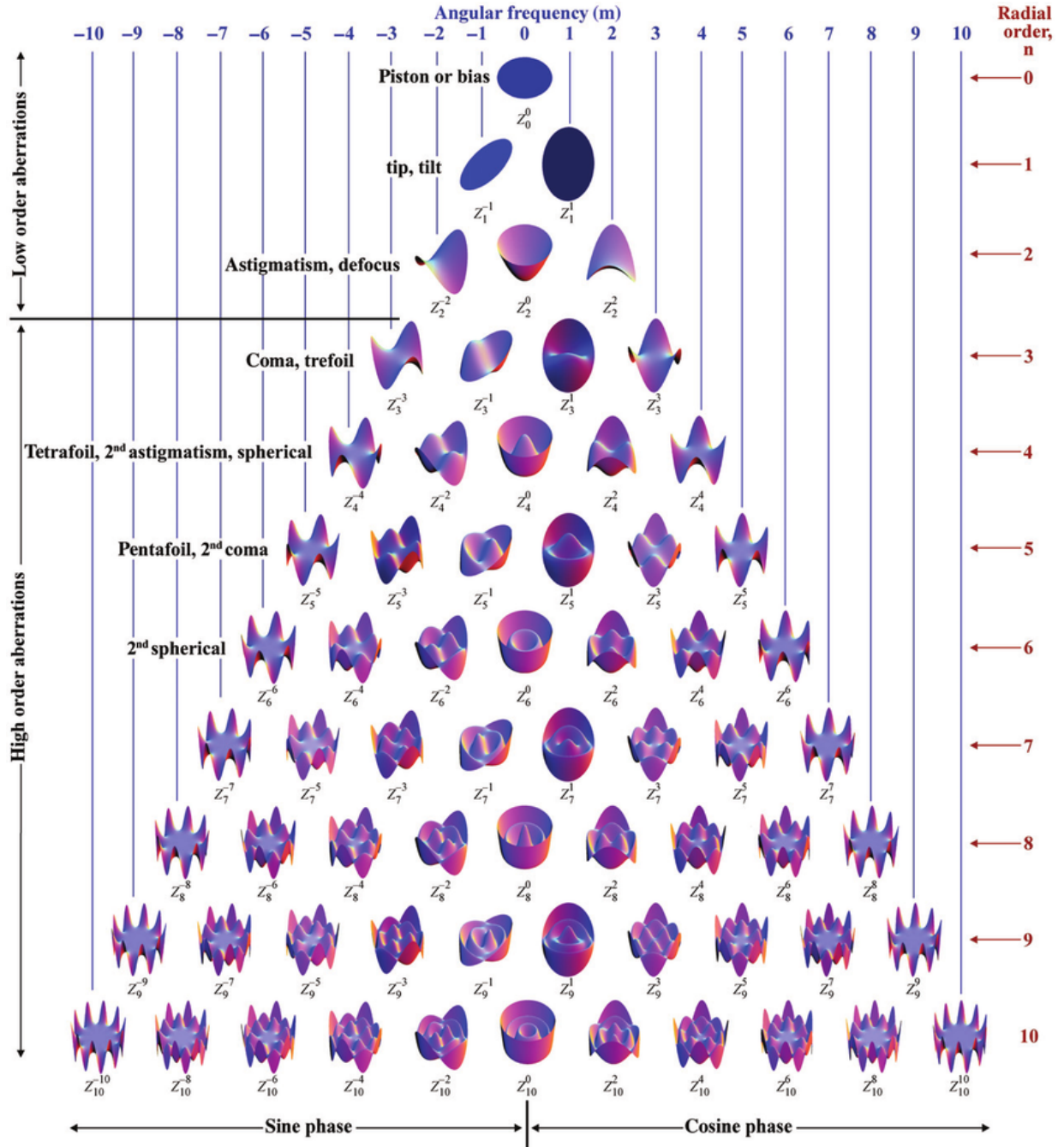


Figure 10: Standard shapes of wavefronts for n order and m frequency Zernike polynomials (Lakshminarayanan & Fleck, 2011)

When an incoming corrupted wavefront is coupled into a single mode fibre, only the fundamental mode of the fibre is allowed to pass through the core. All other modes are reflected or dissipated through the cladding. Thus, when a corrupted wave front is coupled into a single mode fibre, all the phase aberrations are lost and the output will be a plane wavefront.

Beam couplers based on IO devices can also act as a spatial filters. Single mode waveguides can be etched on silica based IO chips with photolithography (GRAVITY, PIONEER) (Benisty et al., 2009), or it can be written on Gallium Lanthanum Sulphide (GLS) based IO chips using ultra-fast laser inscription (Tepper et al., 2017). X-shaped and Y-junction couplers written on an IO chip does a dual purpose of beam combination as well as spatial filtering.

1.5 FRINGE TRACKING

Even though adaptive optics and spatial filters correct for most of the wavefront aberrations, the zero order zernike mode (piston) is not corrected. This is because the AO systems and spatial filters considers only the local phase fluctuations and result in a flat wavefront. However, the global phase difference between the two telescopes of the interferometer plays a significant role in the position of the fringes on the detector. Over long integration time, the fringe shift due to piston fluctuations results in a degradation of the fringe contrast and thus the visibility estimation. Hence, it is essential to have a fringe tracker on top of the adaptive optics system to stabilize the position of the fringes and thus increasing the sensitivity of the instrument. A fringe tracker is a second beam combiner instrument which works alongside the main science beam combiner measuring and stabilizing the position of the central fringe (zero OPD) or the center of the fringe envelope.

1.5.1 Phase delay tracking (Co-phasing)

Co phasing is to track the individual fringe phases. Co-phasing involves tracking at the rate of atmospheric turbulence time scale (coherence time) at the corresponding wavelength. In K band a typical time scale is about 12ms and 20ms for the L band. For more precise tracking, the sample rate should be smaller than this time scale.

Currently at VLTI Gravity fringe tracker, FINITO, Prima FSU does phase delay tracking in the H and K bands. Phase delay tracking produces high accuracy on the position on the detector (\sim fraction of λ on the OPD). Due to high processing rates and low integration time, phase delay tracking is restricted highly by the sensitivity of the instrument.

Gravity can perform co-phasing on the K band with a sensitivity of 10 in magnitude with an accuracy of 350nm (with a 10th magnitude phase reference) with the unit telescopes (Choquet et al., 2014).

1.5.2 Group delay tracking (Coherencing)

The broadband interferometric fringes has two major components, the fringes and the fringe envelope as shown in fig. 11. Cophasing involves in tracking the fringe phases at the atmospheric coherence time. However, due to the dispersion of water vapor content of the atmosphere, each wavelength channel has its own corresponding path delay. This makes phase tracking harder, as a typical phase delay tracker has to estimate the phases in each wavelength channel by dispersing the fringes, thus losing the flux and sensitivity. However, if the science case doesn't require the precision of a phase delay tracker, the fringe packet can be tracked instead of the individual phases. The main advantage of group delay estimation is the ability to integrate the faint stellar fringes over longer period than that required by a phase delay tracker (~100ms-2 seconds). This increases the signal to noise ratio and thus the fringes in the science channel can be coherenced by 2-3 magnitudes fainter reference.

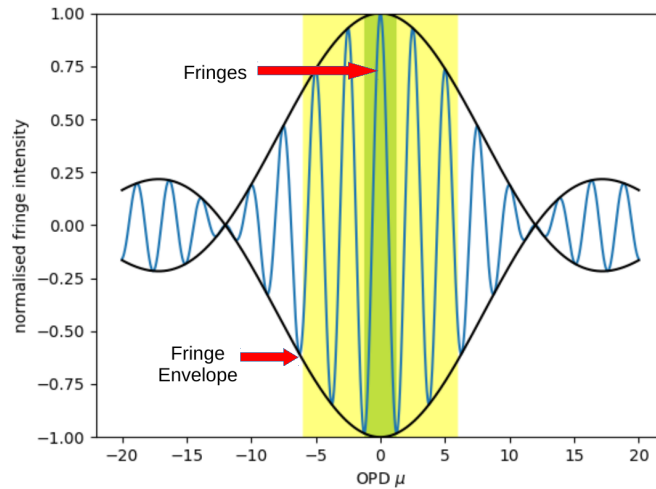


Figure 11: Representation of broadband fringes and fringe envelope. The green shaded region shows the region of accuracy in which the cophasing is done. The yellow region shows the accuracy in which coherencing is done.

1.6 CLOSURE PHASE

Another technique in estimating the phase of the astronomical source is to combine the phases from 3 baselines of the interferometer. The phases at the three baselines are given by,

$$\Phi_{12} = \phi_{12} + \Delta\phi_{12} = \phi_{12} + \phi'_1 - \phi'_2$$

$$\Phi_{23} = \phi_{23} + \Delta\phi_{23} = \phi_{23} + \phi'_2 - \phi'_3$$

$$\Phi_{31} = \phi_{31} + \Delta\phi_{31} = \phi_{31} + \phi'_3 - \phi'_1 \quad (10)$$

Where, ϕ_{12} , ϕ_{23} & ϕ_{31} are the phase differences of the source between baselines 12,23 & 31 respectively and ϕ'_1 , ϕ'_2 & ϕ'_3 are the piston induced by the atmospheric turbulence and instrumental vibrations. Thus adding the phase differences at the three baselines,

$$\begin{aligned} \Phi_{123} &= \Phi_{12} + \Phi_{23} + \Phi_{31} = \phi_{12} + \phi_{23} + \phi_{31} + \phi'_1 - \phi'_2 + \phi'_2 - \phi'_3 + \phi'_3 - \phi'_1 \\ &= \phi_{12} + \phi_{23} + \phi_{31} \quad (11) \end{aligned}$$

Thus, by adding the phase differences at the three baselines, we can completely remove the atmospheric contribution and retrieve the pure phase differences of the source. This is known as closure phase Φ_{123} .

1.7 FRINGE TRACKING FOR INFRARED TARGETS

Fig. 12 shows the comparison of K and L band magnitudes of class 1 and class 2 YSOs in embedded clusters. The vertical blue line shows the K band phase delay tracking sensitivity of Gravity fringe tracker (Choquet et al., 2014). The horizontal red and green dashed lines shows us the L band sensitivity of MATISSE at low spectral resolution without and with an external fringe tracker respectively (Matter et al., 2016).

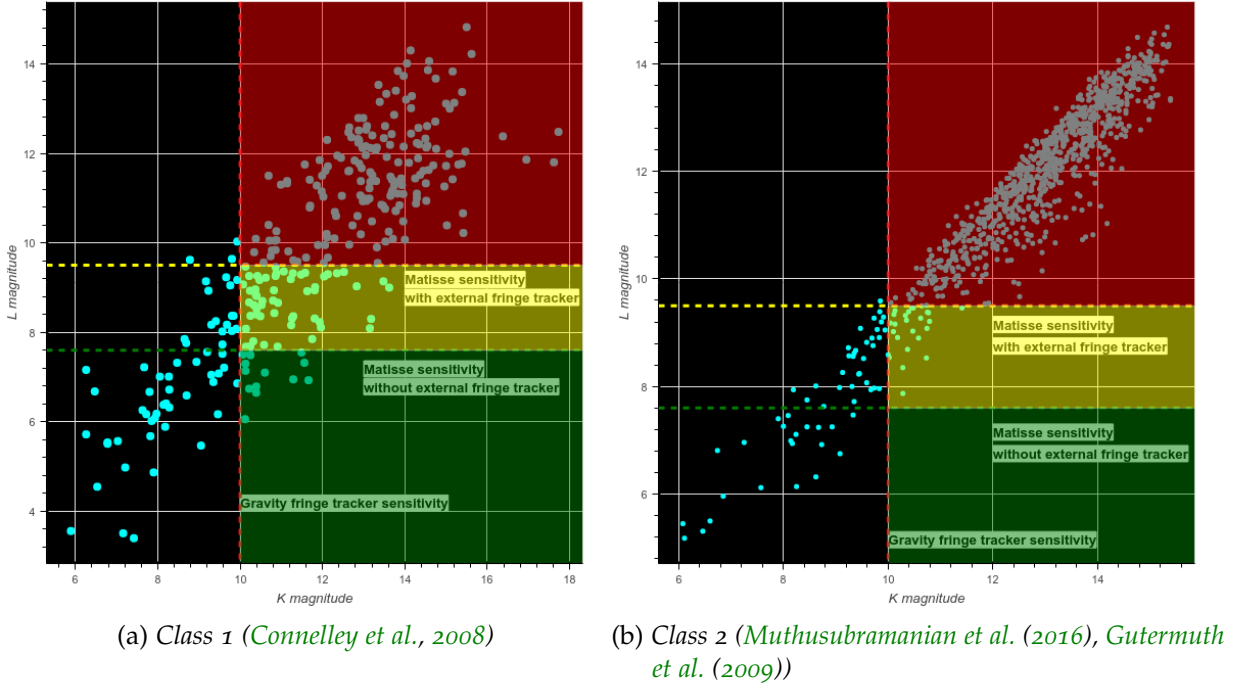


Figure 12: Comparison of K and L band magnitudes of YSOs in embedded clusters. The vertical red line shows the K band sensitivity limit of Gravity fringe tracker. The horizontal green and yellow dashed lines show the L band sensitivity of MATISSE operating without and with an external fringe tracker respectively. The green and yellow shaded region contains targets which are too faint to be detected with Gravity fringe tracker in the K band but are bright enough to be detected by MATISSE without and with an external fringe tracker respectively

Objects in yellow and green shaded regions in fig. 12 are YSOs that cannot be tracked by Gravity fringe tracker, but they are still within the L band sensitivity limits of MATISSE at low spectral resolution. It would be beneficial to observe these targets by performing on source fringe tracking in the L band.

The objects in the lower left quadrant of the plots are within the current sensitivity limits at K and L bands. Hence, it would be beneficial to perform fringe tracking by referencing in both K and L bands simultaneously.

1.8 GOALS OF THE THESIS

In this work, I have explored the possibilities in performing group delay tracking in the L band alongside the K band for red targets including YSOs, AGN & DSO, which are brighter at longer wavelengths. This adds another advantage of longer coherence time

in the L band while comparing to shorter wavelengths and thus a longer integration time for the group delay estimates. We analyze the possibility to increase the sensitivity (as compared to the values shown in fig. 12) in estimating the visibility amplitude in the science channel by stacking the individual fringe frames through their power spectra, while maintaining the fringes within the coherence length (Coherencing). This increases the sensitivity in both the fringe tracking as well as the science channel in observing at such long wavelengths.

We also explore the possibility in coherencing mid-infrared fringes (M and N bands) by feed forwarding the group delay estimates using K and L band group delay measurements.

ATMOSPHERIC TURBULENCE

Big whorls have little whorls
Which feed on their velocity
And little whorls have lesser whorls,
And so on to viscosity.

– Lewis Fry Richardson, *Weather prediction by Numerical Models* (1922).

2.1 KELVIN-HELMHOLTZ INSTABILITY

To understand the turbulence in Earth's atmosphere, we have to understand the flow of different layers of fluids in the atmosphere. The motion of a fluid in a medium can be characterized by the Reynold's number. The Reynold's number is defined as the ratio of inertial forces and the viscous forces and is given by,

$$Re = \frac{VL}{\nu} \quad (12)$$

where,

- $V \rightarrow$ Maximum velocity of the fluid (m s^{-1})
- $L \rightarrow$ Characteristic length scale of the fluid (m)
- $\nu \rightarrow$ Kinematic viscosity (m^2s^{-1})

At low values of Re ($< 10^6$), the fluid exhibits a laminar flow. At larger values of Re ($> 10^6$) the fluid is said to exhibit turbulent behavior. The typical parameters for atmosphere are,

- $L = 22 \text{ m}$
- $V = 10 \text{ ms}^{-1}$
- $\nu = 15 \times 10^{-6} \text{m}^2\text{s}^{-1}$

This results in a Reynold's number of $Re = 1.46 \times 10^7$. This corresponds to a fully developed turbulent flow. The turbulence of the atmosphere is dominated by Kelvin-Helmholtz instability. Kelvin-Helmholtz instability occurs in a turbulence fluid when there is a velocity shear on the layers of the fluid. This occurs due to the gradient of the wind velocity over the altitude of the layers of atmosphere.

2.2 KOLMOGOROV THEORY OF ATMOSPHERIC TURBULENCE

Kolmogorov's theory of atmospheric turbulence (Kolmogorov, 1941) deals with the cascade of the kinetic energy transfer from large scale to smaller scale turbulence vortices. There are three major assumptions of the Kolmogorov's theory of turbulence. The turbulent fluid (atmosphere) is homogeneous and isotropic. In other words, the physical processes that occurs at different spatial points and directions in space are the same. The third major assumption is that the fluid is incompressible and can be characterized by the Navier-Stokes continuity equation,

$$\nabla \cdot \vec{U} = 0 \quad (13)$$

Where \vec{U} is the velocity vector (U_x, U_y, U_z) which has zero divergence and can be characterized by irregular eddy motions given by the non-zero vorticity,

$$\vec{\omega} = \nabla \times \vec{U} \quad (14)$$

The velocity vector can be represented as the sum of laminar flow velocity \vec{u} and the turbulent component \vec{u}' . We can thus define the velocity correlation tensor of the turbulent component as,

$$R_{ij} = \langle \vec{u}'_i(\vec{x}) \vec{u}'_j(\vec{x} + \vec{r}) \rangle \quad (15)$$

Since the turbulent field is homogeneous and isotropic, the velocity correlation tensor depends only on the separation between the spatial points \vec{r} and not the position vector \vec{x} of the measuring points. To understand the cascade of kinetic energy from large eddies to smaller ones, we have to estimate the energy spectrum tensor which is the Fourier transform of the velocity correlation tensor. The energy spectrum tensor is thus given by,

$$\phi_{ij}(\vec{k}) = \frac{1}{(2\pi)^3} \int_0^\infty R_{ij}(\vec{r}) e^{-i\vec{k}\vec{r}} d^3\vec{r} \quad (16)$$

Where, \vec{k} is the spatial frequency and is defined as,

$$\vec{k} = (2\pi)/(\vec{r}) \quad (17)$$

The energy spectrum function is thus calculated by the trace of $\phi_{ij}(\vec{k})$ as,

$$E(k) = 2\pi k^2 \sum_i \phi_{ii}(\vec{k}) \quad (18)$$

During the energy cascade, the kinetic energy of the large scale eddies is dissipated to the smaller scale eddies through viscous heating. The turbulent energy dissipated by viscosity is given by,

$$\epsilon_d = 2\nu \int_0^\infty k^2 E(k) dk \quad (19)$$

To have a steady cascade of energy transport from large to small scale eddies which then dissipates through viscous heating, there needs to be a constant supply of kinetic energy at the large scales. This energy supply for atmospheric turbulence comes from the solar radiation.

Kolmogorov assumes a self-similarity model, where there is a dissipation free cascade of kinetic energy through the eddies. Thus, we can define a length scale beyond which the viscous dissipation dominates. The self similarity model states that a fully developed turbulence model depends only on ν and ϵ_d . ν has the dimensions of L^2T^{-1} and ϵ_d has the dimensions of L^2T^{-3} . The characteristic length scale (inner/ Kolmogorov/ dissipational length scale) can thus be derived through dimensional analysis as,

$$l_0 = \left(\frac{\nu^3}{\epsilon_d} \right)^{1/4} \quad (20)$$

for dry air in earth's atmosphere, the value of l_0 is 0.1cm and we can define an associated velocity of the vortice at l_0 as,

$$u_0 = (\nu \epsilon_d)^{1/4} \quad (21)$$

The Kolmogorov's self similar turbulence model has a power spectrum given by,

$$E(k) = u_0^2 l_0 E_*(l_0 k) \quad (22)$$

Where E_* is a dimensionless scaling factor. Since, the main range in which Kolmogorov's self similar model operates is purely dominated by inertial dispersion and no viscous dispersion, the power spectra must be scale free and should not depend on the kinematic viscosity ν . Thus, the scaling function can be defined as,

$$E_*(l_0 k) = C \times (l_0 k)^n \quad (23)$$

Where C is a dimensionless constant of proportionality of order unity. Thus, substituting the values of l_0 , u_0 and E_* from equations 20, 21 & 23 respectively into equation 22.

$$E(k) = \nu^{1/2} \epsilon_d^{1/2} \nu^{3/4} \epsilon_d^{-1/4} C \nu^{3n/4} \epsilon_d^{-n/4} k^n \quad (24)$$

As the power spectrum is purely inertial, it should have no dependence on ν . Thus solving for n to remove the dependence on ν , we get,

$$E(k) = C \epsilon_d^{2/3} k^{-5/3} \quad (25)$$

This is known as the Kolmogorov's power spectrum of atmospheric turbulence. The $-5/3$ exponent is derived for 2 dimensional turbulence behavior. However, in the case of 3D turbulence simulations the exponent is then $-11/3$ (Tatarski et al., 1961).

2.2.1 Outer scale

To estimate the velocity correlation tensor, we can estimate the total velocity vector and subtract the laminar component. However, it is difficult to decouple and estimate the laminar component in laboratory experiments and other real time scenarios. Hence, it is easier to estimate the trace of the velocity correlation tensor defined as,

$$R(r) = \sum_i R_{ii}(\vec{r}) \quad (26)$$

The velocity correlation breaks as $R \rightarrow 0$ by $R(r) \rightarrow \langle |u|^2 \rangle$. Thus, we can define a characteristic length scale at which this correlation breaks as,

$$L_0 = \frac{1}{R(0)} \int_0^\infty R(r) dr \quad (27)$$

L_0 is the characteristic upper limit beyond which the kinematic energy cannot sustain an eddy anymore and thus the spatial points which are separated beyond L_0 is completely uncorrelated. This is also known as the outer scale of earth's atmosphere.

The outer scale at Paranal, Chile measured using the Generalised Seeing Monitor (GSM) is 22 meters (Martin et al. (2000) Dali Ali et al. (2010)). However, the value of L_0 is too low to match the OPD fluctuations measured in the K band with PRIMA (Sahlmann et al., 2009) and in the H band with FINITO (Le Bouquin et al., 2008). Thus Choquet et al. (2014) uses a value of 100 meters which matches the measured OPD fluctuations than the models at 22 meters.

2.2.2 von Karman power spectrum

To account for the decorrelation beyond the outer scale, von Kármán (1948) suggested a power spectrum of atmospheric turbulence which includes the outer scale (L_0) as,

$$E(k) \propto \left(k^2 + \left(\frac{1}{L_0} \right)^2 \right)^{-11/6} \quad (28)$$

Fig. 13 shows the turbulence power spectrum measured in the laboratory experiment (Champagne, 1978).

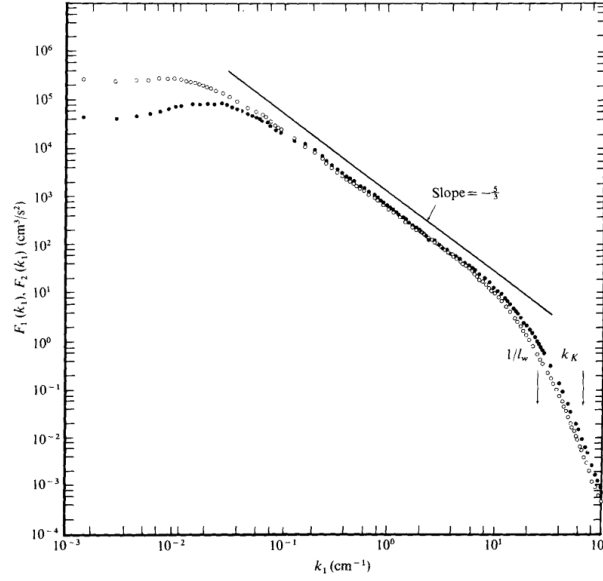


Figure 13: Power spectrum of a laboratory turbulence (*Champagne, 1978*)

2.3 NUMERICAL SIMULATIONS OF ATMOSPHERIC TURBULENCE

2.3.1 white noise

White noise is a signal where there is no correlation between the sample points of the signal. In other words they have a flat power spectrum at all frequencies. Such signals are termed as stochastic and are only defined by statistical quantities such as mean and standard deviation. Figure 14 shows an example random white noise with amplitudes in arbitrary units with a mean of zero and a standard deviation of unity.

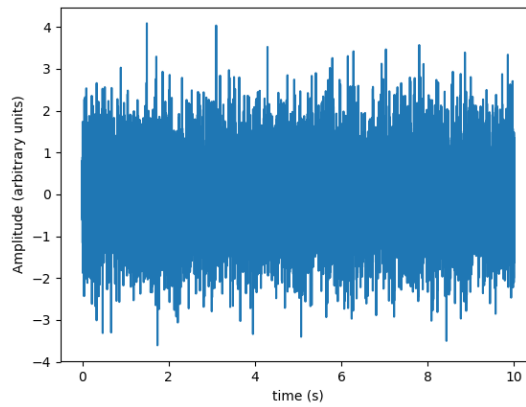


Figure 14: Sample random white noise over time

The amplitudes of the random white noise signal follows a Gaussian distribution. Fig. 15 shows the histogram of the values in the random white noise from fig. 14.

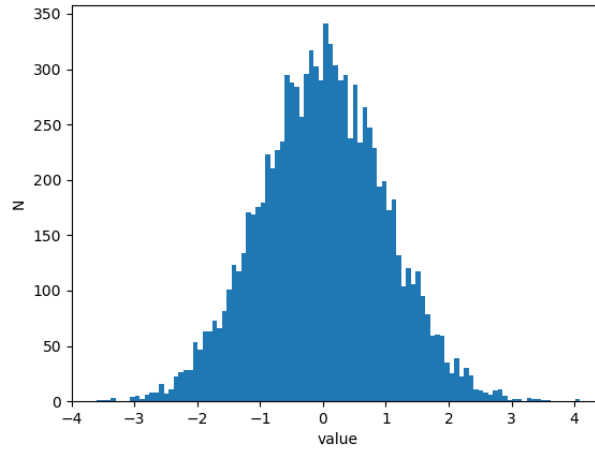


Figure 15: *Distribution of the values in the random white noise*

The power spectrum of the white noise from fig. 14 is shown in fig. 16. The power spectrum of the white noise is flat as the values are completely uncorrelated.

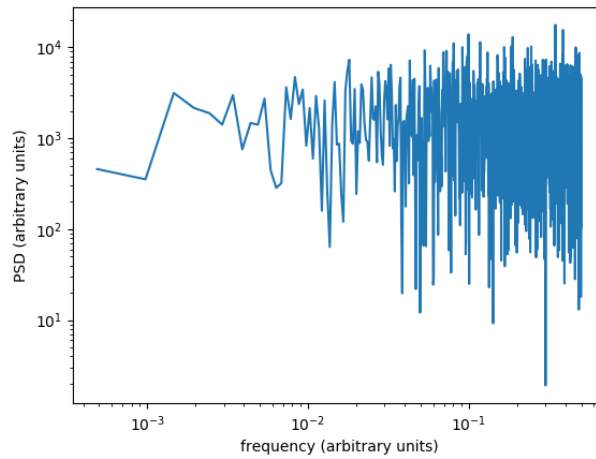


Figure 16: *Power spectrum of the random white noise*

We can see that from the flat power spectrum and the Gaussian distribution of the values, the white noise is perfect initial random distribution to play with different models of atmospheric turbulence.

2.3.2 Generating random turbulence screens

Kolmogorov screens are more efficient and computationally less expensive for turbulence fields smaller than the outer scale of the atmosphere. Hence for a single telescope AO simulations (where $D < L_0$), Kolmogorov screens are preferred over von Karman screens. However, for interferometry using long baselines (where $B > L_0$), the decorrelation beyond the outer scale becomes important.

The fluctuations caused due to atmospheric turbulence is a random Gaussian process. Hence, to generate a random realization of the atmosphere, the selected power spectrum (Kolmogorov/von Karman) is multiplied to the power spectrum of a random white noise which is centered around zero and has a standard deviation of unity. Figure 17 shows a sample random realization of a 2D white noise and the 2D Kolmogorov power spectrum.

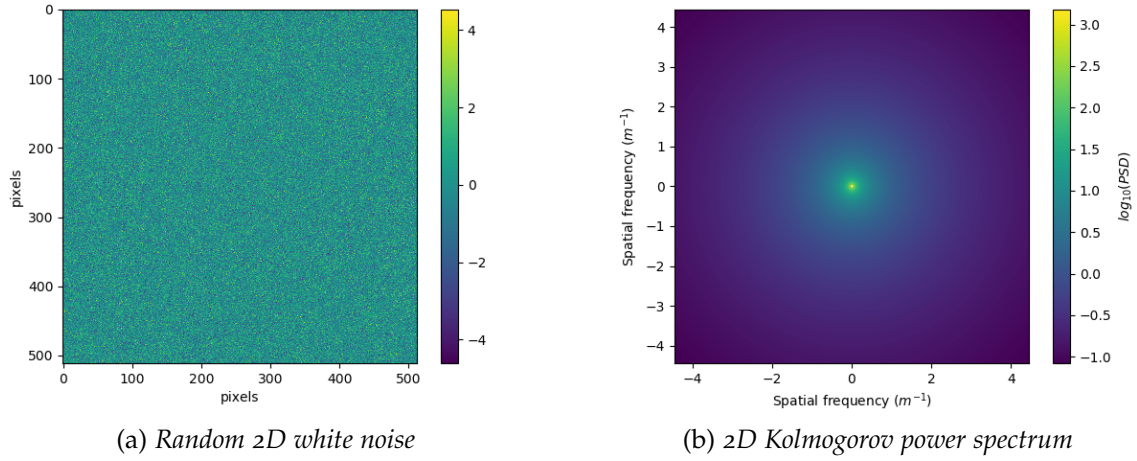


Figure 17: initial conditions for generating a Kolmogorov turbulence screen on refractive index

Figure 18 shows the final simulated turbulence screens. Fig. 18a shows a Kolmogorov screen with infinite outer scale and fig. 18b shows a von Karman screen with an outer scale of 25 meters.

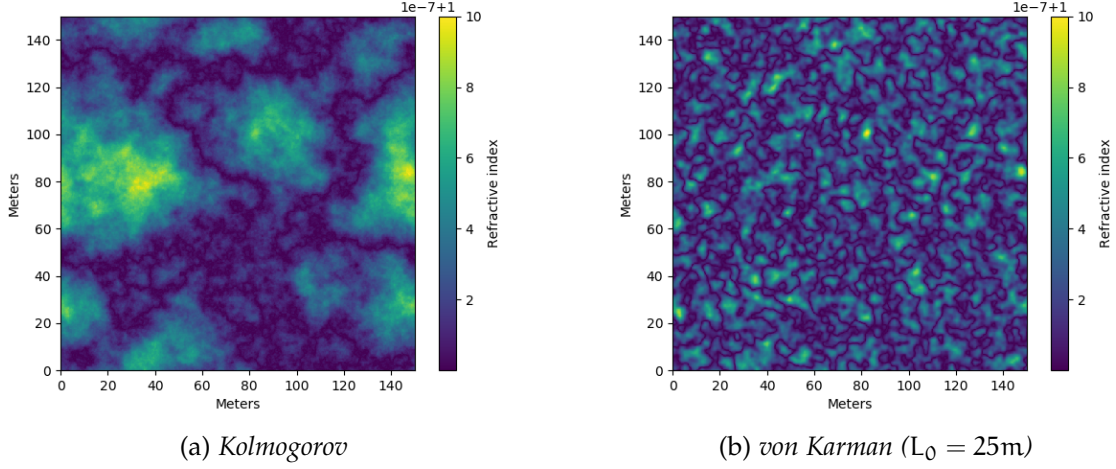


Figure 18: A random realization of Kolmogorov turbulence screen on refractive index

2.4 CHARACTERIZING TURBULENT SCREENS

Once the phase screen is simulated, we can derive some physical parameters from it. The most fundamental function to analyze is the structure function (correlation function). The structure function of an atmospheric turbulence parameter is defined as the averaged squared difference of the parameter at two sample points separated by a distance 'r'. The structure function of a parameter 'X' is thus defined by,

$$D_x(r) = \langle |X(r_1) - X(r_1 - r)|^2 \rangle \quad (29)$$

Thus the structure function measures the auto-correlation of the input phase screen. It also describes the expected difference of the parameter 'X' in a turbulence field separated by a distance 'r'.

2.4.1 Kolmogorov-Obhukov statistics

Kolmogorov's self-similar model follows only the dissipation free cascade of kinetic energy from large to smaller scale eddies. Hence, to understand the energy cascade in the simulated turbulence screen, we can first look into the structure function of the turbulence velocity field. Hence, from equation 29, the velocity structure function can be defined as,

$$D_v(r) = \langle |v(r_1) - v(r_1 - r)|^2 \rangle \quad (30)$$

As the energy cascade is dissipation free we can rewrite equation 31 as an arbitrary function $f(r/l_0)$ by dividing the into cells of the size of the inner scale length. As the structure function $D_v(r)$ has the dimensions of squared velocity and $f(r/l_0)$ is a dimensionless function, equation 31 becomes,

$$D_v(r) = \alpha f(r/l_0) \quad (31)$$

Where, α is a constant which has the dimensions of squared velocity. Due to self similarity model, the parameter α should depend only on ν and ϵ_d . Thus from equation 21, α can be represented as,

$$\alpha = (\nu \epsilon_d)^{1/2} \quad (32)$$

The dimensionless function can be defined as,

$$f(r/l_0) = k \left(\frac{r}{l_0} \right)^n \quad (33)$$

Where, k is a dimensionless constant. Thus the structure function from equation 31 can be rewritten as,

$$D_v(r) = k\alpha \left(\frac{r}{l_0} \right)^n \quad (34)$$

from equations 32 and 20,

$$D_v(r) = k\nu^{1/2}\epsilon_d^{1/2}\nu^{-3n/4}\epsilon_d^{n/4}r^n \quad (35)$$

As the system is in the inertial range, the structure function shouldn't depend on the kinematic viscosity ν . Thus the value of n should be $2/3$ in order to remove the dependence of ν from equation 35, making it,

$$D_v(r) = k\epsilon_d^{2/3}r^{2/3} = C_v^2 r^{2/3} \quad (36)$$

Where C_v^2 is defined as the structure function coefficient and is given by,

$$C_v^2 = k\epsilon_d^{2/3} \quad (37)$$

The value of the structure function parameter is important for different instruments and telescope site characterization as it is a measure of the strength of the atmospheric turbulence at that location.

2.4.2 Other structure functions

The velocity field transports the kinetic energy in parcels of eddies. As these parcels are in pressure equilibrium, the fluctuations are mainly on temperature and densities (thus on the refractive index). Therefore, the structure functions on temperature and refractive index also follows the Kolmogorov-Obhukov law. Hence, the structure function on temperature and refractive index is,

$$D_T(r) = C_T^2 r^{2/3} \quad (38)$$

$$D_n(r) = C_n^2 r^{2/3} \quad (39)$$

Using ideal gas laws and as the refractive index (n) is directly proportional to the density (ρ), the structure function coefficients C_n & C_T are related as, (Quirrenbach, 2014)

$$C_n = (7.8 \times 10^{-5} P[\text{mbar}] / T^2[\text{K}]) C_T \quad (40)$$

Fig. 19 shows the two point correlation function estimated from the Kolmogorov phase screen (fig. 18a) and the analytical fit from eq.39.

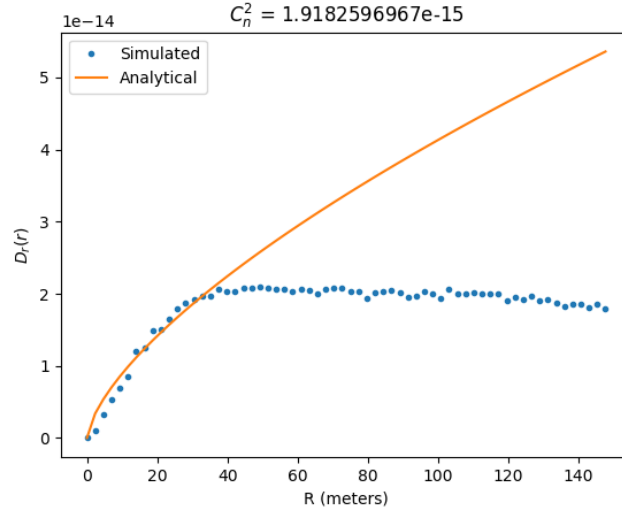


Figure 19: Structure function estimated from the Kolmogorov screen (fig. 18a) and the analytical fit given by eq. 39. We see a divergence between the analytical and the numerical correlation functions at a distance of $0.26 \times$ box size. This is mainly computational issue due to the limited box size of the simulated refractive index screen.

The correlation function computed from the phase screen breaks off from the theoretical prediction at a point which is 0.26 times the box size. In the case of fig. 19, the break off occurs at a point of 40 meters. This effect is mainly due to computational restrictions. As the separation between the points goes above this distance, the number of sample data point reduces drastically. Hence, the signal appears highly decorrelated. In our simulations we chose a box size which is slightly larger than 3.75 times the baseline of the interferometer to be within the correlated part.

2.4.3 Phase Structure function

The phase structure function plays an important role in understanding the propagation of light through a turbulent screen. The phase structure function can be defined through eq. 29 as,

$$D_{\phi}(r) = \langle |\phi(x) - \phi(x+r)|^2 \rangle \quad (41)$$

The phase of a light wave propagating through a medium of refractive index n and thickness δh is given by,

$$\phi = \frac{2\pi}{\lambda} n \delta h \quad (42)$$

A similar approach can be used to relate the phase structure function and the refractive index structure function through equations 39 & 41. Thus for a incoming stellar wavefront traveling through a layer of atmosphere of thickness δh_i and a refractive index structure function coefficient $C_{n,i}$, the phase structure is given by,

$$D_{\phi,i}(r) = 2.91 \left(\frac{2\pi}{\lambda} \right)^2 \delta h_i C_{n,i}^2 r^{5/3} \quad (43)$$

For an atmosphere with multiple layers of different refractive index turbulence screens, the phase structure function is given as,

$$D_{\phi}(r) = 2.91 \left(\frac{2\pi}{\lambda} \right)^2 \sec \zeta \int C_n^2(h) dh r^{5/3} \quad (44)$$

Where ζ is the hour angle of the observing target. The further the object is away from the zenith, the longer is the path traveled by the light through the turbulent medium. Hence, the larger the hour angle the more wave gets abberated.

There is a minimum value of r , where the effect of atmospheric turbulence on the wavefront aberrations is the least. This length is called the Fried's parameter (r_0). The Fried's parameter is the maximum value of r where the rms of phase fluctuations is less than 1 radian. Thus plugging in 1 radian and solving for r in eq. 44, the value of r_0 can be computed as,

$$r_0 = \left(0.423 \left(\frac{2\pi}{\lambda} \right)^2 \sec \zeta \int C_n^2(h) dh \right)^{-3/5} \quad (45)$$

For example, an incoming K-band wavefront ($2.0 - 2.4 \mu\text{m}$) will have a Fried parameter (r_0) of 60 centimeters.

The phase structure function can thus be redefined as,

$$D_\phi(r) = 6.88 \left(\frac{r}{r_0} \right)^{5/3} \quad (46)$$

Applying the same 1 radian rms limit on eq. 43, the Fried parameter (r_0) for a single layer of atmosphere with a thickness δh is given by,

$$r_0 = 2.361 \left(\left(\frac{2\pi}{\lambda} \right) \delta h C_n^2 \right)^{-3/5} \quad (47)$$

2.4.3.1 Turbulence profile of atmosphere

The dependence of C_n^2 over altitude or the C_n^2 profile is a key information to understand the nature of turbulence at an astronomical observatory site. There are a few analytical and empirical models for the C_n^2 profile for different altitudes.

Kaimal model

This model proposed by [Kaimal et al. \(1976\)](#) is a simple analytic relation that relates the C_n^2 at any arbitrary height h_0 to that of another height h by,

$$\frac{C_n^2(h)}{C_n^2(h_0)} = \left(\frac{h}{h_0} \right)^{-4/3} \quad (48)$$

Walters-Kunkel model

The Kaimal model however doesn't include the effect of temperature inversion in the atmosphere. This inversion layer in temperature will affect the evolution C_T^2 over height and thus C_n^2 . The Walters & Kunkel model (Walters & Kunkel, 1981) estimates the evolution of C_n^2 vertically by,

$$\frac{C_n^2(h)}{C_n^2(h_0)} = \begin{cases} \left(\frac{h}{h_0}\right)^{-4/3} & h_0, h \leq 0.5h_i \\ \left(\frac{0.5h_i}{h_0}\right)^{-4/3} & 0.5h_i \leq h \leq 0.7h_i \\ 2.9 \left(\frac{0.5h_i}{h_0}\right)^{-4/3} \left(\frac{h}{h_i}\right)^3 & 0.7h_i \leq h \leq h_i \end{cases} \quad (49)$$

Where h_i is the height of the inversion layer in the atmosphere.

Hufnagel-Valley model

Unlike Kaimal and Walters-Kunkel model which are analytically estimated, the Hufnagel-Valley model (Lawson & Carrano, 2006) is an empirical fit to high altitude measurements of C_n^2 . The Hufnagel-Valley relation is given by,

$$C_n^2(h) = 5.94 \times 10^{-53} (v/27)^2 h^{10} e^{(-h/1000)} + 2.7 \times 10^{-16} e^{(-h/1500)} + C_{n0}^2 e^{(-h/100)} \quad (50)$$

Where, v is the velocity of wind at that altitude and C_{n0}^2 is the structure function constant near the ground level.

The wind velocities can be estimated for major observatory sites by an empirical fit model given by Roberts & Bradford (2011). Fig. 20 shows the wind velocities at Antofagasta base which is about 150kms from the VLT during the month of July.

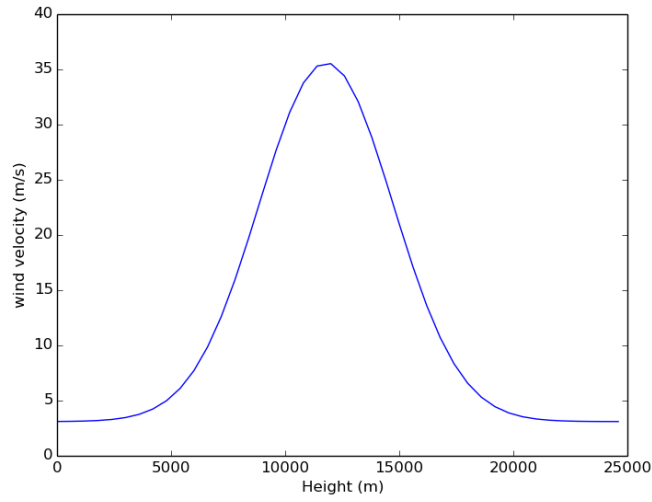


Figure 20: Wind velocity as a function of height at Antofagasta base during the month of July

Fig. 21 shows the C_n^2 tracks of the three models over height.

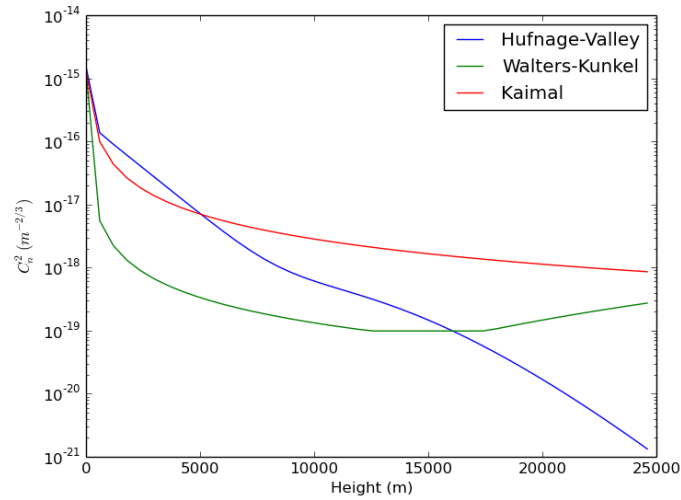


Figure 21: Comparison of the three C_n^2 models

Figure 22 shows us the turbulence strength of the atmosphere measured above Cerro Paranal, Chile (Quirrenbach, 2014). In our models we implement the Hufnagel-Valley model of C_n^2 profile which matches with the observed data more precisely.

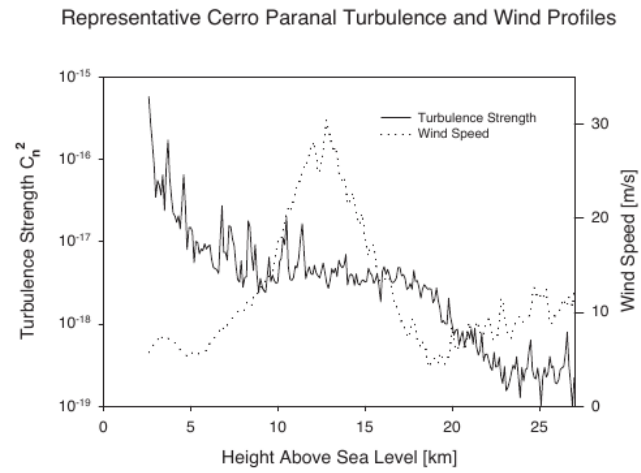


Figure 22: Turbulence strength measured at Cerro Paranal, Chile ([Quirrenbach, 2014](#))

3.1 GDSIM

In our study, we investigate the effects of atmospheric turbulence and the differential dispersion of atmospheric water vapor on K and L band fringes. Hence, I have constructed a simulator (GDSIM) based on the first principles that involves propagation of light waves through a turbulent medium. Currently, simulators such as SOAPY (Reeves, 2016), YAO (Rigaut & Van Dam, 2013), TurSim (Thomas, 2004), etc. simulates the atmospheric turbulence over a single telescope and their response on the adaptive optics wavefront sensor. In the case of long baseline optical/infrared interferometry, the decorrelation of the turbulent energy transport between distances greater than the outer scale of the atmosphere becomes important. Simulators such as Choquet et al. (2014) were developed to simulate the instrumental stabilities and control system in order to control the atmospheric turbulence using GRAVITY fringe tracker. I have developed a python based atmospheric turbulence simulator GDSIM, which simulates the piston fluctuations at VLTI due to atmospheric turbulence and instrumental vibrations. GDSIM also includes the chromatic effects of differential dispersion on the OPD due to the atmospheric water vapor at near- and mid- infrared wavelengths.

3.2 TAYLOR'S FROZEN TURBULENCE FLOW HYPOTHESIS

After generating the atmospheric turbulence screen, we shall now discuss about the temporal evolution of these screens over a telescope aperture. Over short timescales and a steady wind flow, the turbulence can be assumed to be static (Taylor, 1938). Hence, to analyze the evolution of a turbulent screen over an aperture, we can simply blow the screen over an aperture mask. Figure 23 shows a sample Kolmogorov screen blown over a circular telescope aperture.

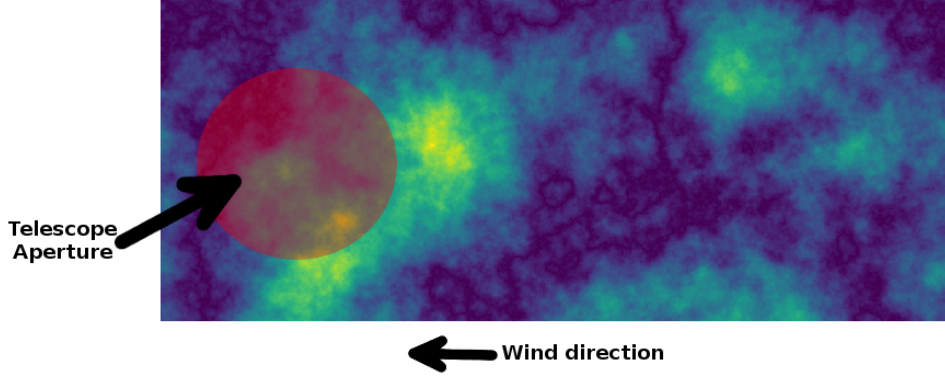


Figure 23: Description of a Kolmogorov turbulent screen blown over a telescope aperture with a specific wind velocity (v)

3.3 PHASE STRUCTURE FUNCTION

To understand the temporal coherence of the phase of the incoming wavefront, we need to understand the phase structure function over different timescales. For a spatial scale r and wind velocity V , the temporal phase structure function can be defined by substituting time scale $t = r/V$ on equation 46 as,

$$D_{\phi}(t) = 6.88 \left(\frac{V t}{r_0} \right) \quad (51)$$

We can thus define a time scale within which the Root Mean Squared (RMS) of phase fluctuations is 1 radian. This is known as the coherence time of the atmosphere. The coherence time of the atmosphere (τ_0) is thus given by,

$$\tau_0 = 0.314 \left(\frac{r_0}{V} \right) \quad (52)$$

A typical coherence time in the K band assuming a wind velocity of 10m/s and a Fried parameter of 60cm is 18.8ms. However in the case of interferometry, the phase fluctuations at both the telescopes needs to be optimized to 1rad RMS. Hence, the coefficient in the structure function (eq. 46) will then be 2×6.88 . Thus we can define a separate inteferometric coherence time as,

$$\tau_0 = 0.207 \left(\frac{r_0}{V} \right) \quad (53)$$

The temporal phase structure function can thus be defined as,

$$D_\phi(t) = \left(\frac{t}{\tau_0} \right)^{-5/3} \quad (54)$$

3.4 TEMPORAL POWER SPECTRUM

Wiener-Kinchin theorem states that the structure function and the power spectrum are a Fourier pair. So the power spectrum can be derived by performing a Fourier transform of the phase structure function in equation 54. However the Fourier integral of equation 54 is non-trivial, the function has to be integrated in certain intervals. The resulting power spectrum is given by (Nightingale & Buscher, 1991),

$$\Phi_\phi(k) = 5.60 \times 10^{-3} \tau_0^{-5/3} k^{-8/3} [\text{rad}^2/\text{Hz}] \quad (55)$$

Equation 55 is the power spectrum of phase fluctuations over a single telescope. However in the case of interferometry, the phase difference between both the telescopes is the key parameter to understand. Hence, the power spectra of the Phase/OPD (as the phase and OPD can be transformed by a multiplicative factor of $2\pi/\lambda$) difference fluctuations between the two telescopes can be computed by convolving the phases with two delta functions corresponding to each arm of the interferometer. Thus the phase power spectrum will be,

$$\Phi_{\text{OPD}}(k) \propto (\text{FT}(D_\phi(r, t)) \times \text{FT}(\delta(r - B/2) - \delta(r + B/2)))^2 \quad (56)$$

Where B is the baseline of the interferometer. The above Fourier transform can be simplified into two regimes. At high temporal frequencies, the OPD fluctuations between the two telescopes are highly uncorrelated thus the power spectrum behaves as in that of a single telescope with a power law exponent of $-8/3$. However, at lower frequencies the fluctuations depends on the model of turbulence used. In the case of a Kolmogorov turbulence, the power spectrum goes with a power law exponent of $-2/3$. Whereas in the case of von Karman power spectrum with a definite outer scale, the power spectrum behaves as an asymptote. Hence, the temporal power spectrum for the phase/OPD fluctuations for an interferometer is given by,

$$P_t(f) \propto \begin{cases} f^{-8/3} & f > f_1 \\ f^{-2/3} & \text{(or)} f^0 \quad f < f_1 \end{cases} \quad (57)$$

Where f_1 is the cut-off frequencies between the two regimes of the power spectrum given by,

$$f_1 = 0.2V/B \quad (58)$$

Where V is the wind velocity. At small baselines (where $B < L_0$), the phase/OPD fluctuations becomes highly spatially correlated hence a Kolmogorov temporal power spectrum will be more applicable. At long baselines (where $B > L_0$), the spatial decorrelation becomes more significant hence the von Karman temporal power spectrum will be applicable. Fig. 24 shows the temporal power spectrum of an interferometer with a baseline 80meters and a wind velocity of 10m/s. [Buscher et al. \(1995\)](#) measured the power spectrum of the OPD fluctuations on the Mark III interferometer at Mt.Wilson and confirmed the two exponent behavior for both Kolmogorov and von Karman like temporal power spectrum. Fig. 25 shows the Kolmogorov and von Karman like two exponent behavior of the power spectrum.

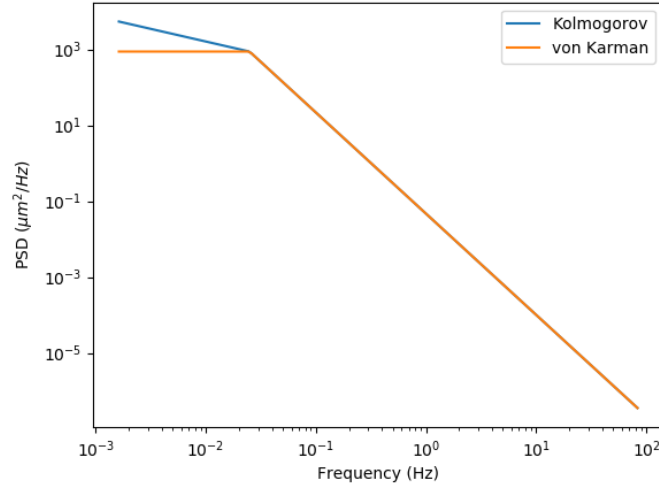


Figure 24: Temporal power spectrum of an interferometer with baseline of 80 meters and wind velocity of 10m/s

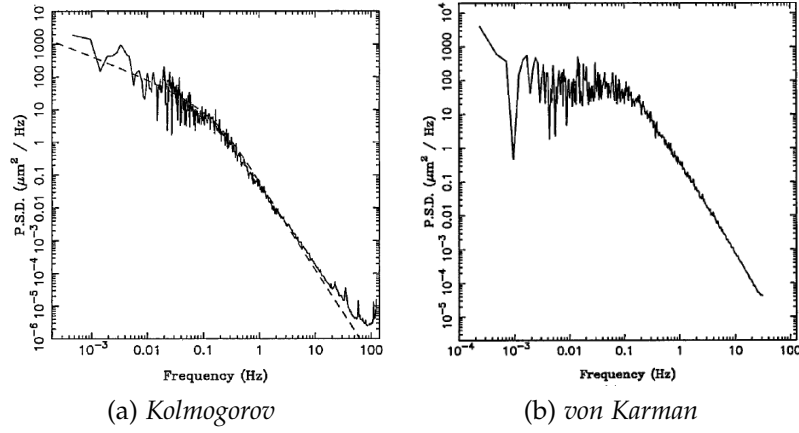


Figure 25: Power spectra of OPD fluctuations measured on Mark III interferometer at Mt. Wilson (Buscher et al., 1995). Both the observations were done at 31.5 meter baseline, but on different observing nights. The effect of the outer scale is clearly visible below 0.1 Hz. On the left plot, the $-2/3$ asymptotic behavior characteristic of the Kolmogorov model is clearly noticeable. On the right plot, the outer scale of that night was smaller and a flat behavior of the power spectrum with a 0 exponent is visible.

Temporal power spectrum from Taylor's hypothesis

Following the Taylor's frozen turbulence flow hypothesis from §3.2, we can now place two masks of 8 meters in diameter separated by a baseline B ($B = 80\text{m}$) on the turbulence screen to derive a temporal power spectrum. The turbulence screen is blown perpendicular to the baseline to avoid the same phase screen crossing the both the apertures. This is shown in fig. 26.

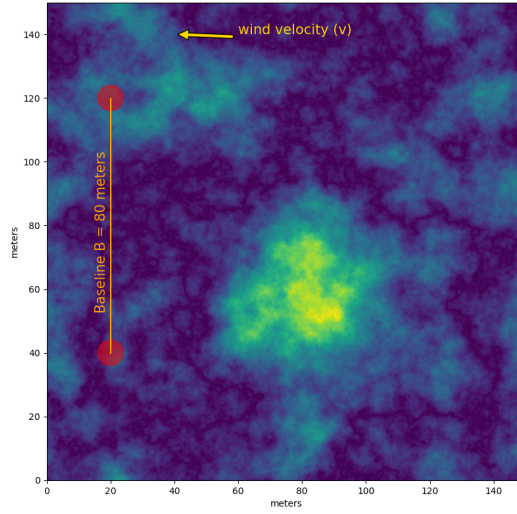


Figure 26: Representation of the Taylor's frozen turbulence flow over an interferometer with 8 meter apertures and a baseline $B = 80\text{m}$

After measuring the piston difference between the two apertures, we can estimate the resulting power spectra of the OPD fluctuation. The power spectrum of the OPD is shown in fig. 27 with a comparison of the analytical power spectrum from eq. 57.

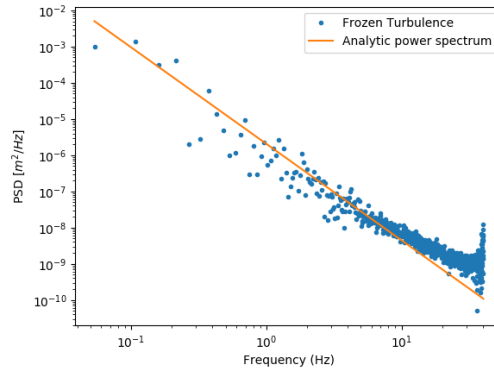


Figure 27: Temporal power spectrum of OPD fluctuations derived with Taylor's frozen turbulence hypothesis compared with the analytical power spectrum. The entire signal was simulated for 18.63 seconds with a 10m/s wind speed

However, Taylor's frozen turbulence hypothesis still lacks sufficient experimental evidences. Caccia et al. (1987) states that the average time scale of evolution of a turbulent cell which is of few centimeters is 60ms. A frozen turbulence to blow over an aperture with an average 10m/s wind velocity can only survive to a distance of 60 centimeters. Hence, for an interferometer with a few tens of meters to a hundred meter

baseline (VLTi), baseline the frozen turbulence hypothesis cannot be used to simulate the temporal fluctuation of the atmosphere.

3.5 INSTRUMENTAL VIBRATION

Another key parameter to consider on top of atmospheric turbulence on the piston fluctuations for an interferometer is the instrumental vibrations. Even though the construction of the VLTi is highly stable for mechanical vibrations, few small scale vibrations to the order of the wavelength of observation can cause fluctuations on the OPD. The vibration at VLTi can be represented by the following differential equation (Choquet et al., 2014)

$$\frac{d^2 p_v}{dt^2} + 4\pi k f_0 \frac{dp_v}{dt} + 4\pi^2 f_0^2 p_v(t) = \frac{v(t)}{T^2} \quad (59)$$

Where,

- $p_v \rightarrow$ random Gaussian signal of the piston vibrations
- $v(t) \rightarrow$ initial Gaussian noise at an instant t
- $f_0 \rightarrow$ natural frequency of the oscillator
- $k \rightarrow$ damping coefficient
- $T \rightarrow$ sampling frequency

Equation 59 results in a power spectrum given by,

$$P_{vib}(f) = \frac{\sigma_v^2 T / (16\pi^4 T^4)}{f^4 + 2f_0^2 f^2 (2k^2 - 1) + f_0^4} \quad (60)$$

Where σ_v is the variance of excitation. The vibration RMS were measured by Mérand et al. (2012) for the AMBER instrument at VLTi. However, the currently the instrumental vibrations at the VLTi have been suppressed to <300nm (Choquet et al., 2014). Tables 1 & 2 lists the values of the parameters for the UT at VLTi.

| | UT ₁ | UT ₂ | UT ₃ | UT ₄ |
|-----------------|-----------------|-----------------|-----------------|-----------------|
| UT ₁ | 377nm | 411nm | 445nm | 738nm |
| UT ₂ | | 215nm | 402nm | 548nm |
| UT ₃ | | | 287nm | 580nm |
| UT ₄ | | | | 542nm |

Table 1: OPD RMS induced by instrumental vibrations of the UTs at VLT (M  rand et al., 2012)

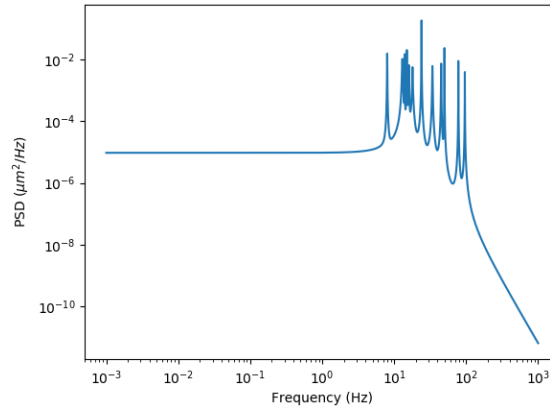


Figure 28: OPD fluctuation power spectrum due to instrumental vibrations at UT₁-UT₂ with a total vibration $\sigma_{\text{OPD,vib}} = 300\text{nm}$

| | f_0 (Hz) | k | σ_v (nm) | | f_0 (Hz) | k | σ_v (nm) |
|-----|------------|-------|-----------------|-----|------------|-------|-----------------|
| UT1 | 8 | 0.003 | 0.25 | UT2 | 13 | 0.01 | 1.8 |
| | 14 | 0.002 | 0.5 | | 15 | 0.003 | 1.0 |
| | 16 | 0.006 | 1.3 | | 18 | 0.02 | 2.5 |
| | 18 | 0.006 | 1.5 | | 24 | 0.002 | 3.0 |
| | 24 | 0.001 | 2.5 | | 34 | 0.004 | 3.0 |
| | 34 | 0.006 | 5.0 | | 45 | 0.003 | 5.0 |
| | 45 | 0.003 | 4.0 | | 96 | 0.001 | 6.0 |
| | 50 | 0.001 | 4.0 | | | | |
| | 78 | 0.001 | 6.0 | | | | |
| | 96 | 0.003 | 7.0 | | | | |
| UT3 | 14 | 0.002 | 1.4 | UT4 | 5 | 0.05 | 0.8 |
| | 17 | 0.01 | 2.5 | | 10 | 0.002 | 0.5 |
| | 24 | 0.001 | 3.7 | | 18 | 0.001 | 2.8 |
| | 34 | 0.003 | 2.0 | | 24 | 0.002 | 5.0 |
| | 46 | 0.002 | 2.7 | | 34 | 0.003 | 4.0 |
| | 49 | 0.001 | 3.0 | | 45 | 0.004 | 6.2 |
| | 86 | 0.003 | 11.0 | | 52 | 0.005 | 9.0 |
| | 94 | 0.002 | 15.0 | | 68 | 0.007 | 13.0 |
| | | | | | 76 | 0.006 | 15.0 |
| | | | | | 85 | 0.002 | 12.0 |
| | | | | | 96 | 0.005 | 18.0 |
| | | | | | 107 | 0.002 | 11.0 |

Table 2: vibration model parameters (Choquet et al., 2014)

3.6 SIMULATING PHASE/OPD FLUCTUATION TIME SERIES

Phase/OPD fluctuation time series can be produced for an interferometer with a white noise and the power spectrum described in eq. 57 using the same technique described in §2.3. A sample random simulated OPD time series is shown in fig. 29 and fig. 30 shows the corresponding power spectrum. Fig. 31 shows a simulated OPD time-series simulated by Choquet et al. (2014).

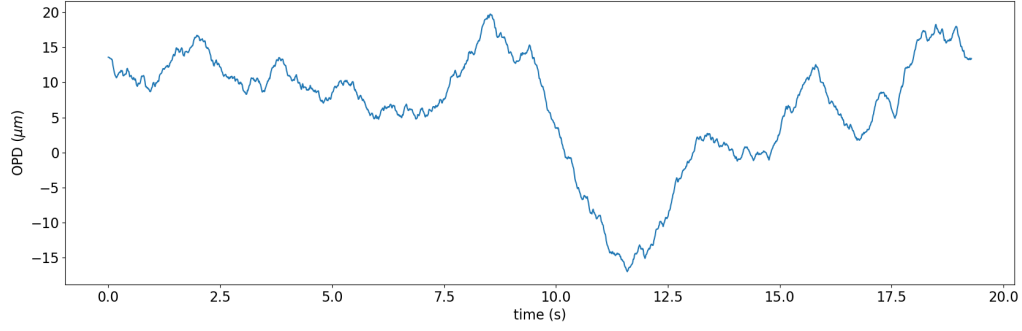


Figure 29: Simulated OPD time-series for an 80 meter baseline including both atmospheric turbulence and instrumental vibrations of UT1-UT2 combination

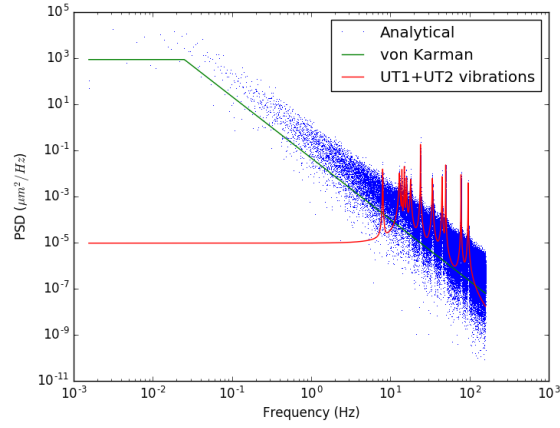


Figure 30: power spectrum of simulated OPD time-series shown in fig. 29

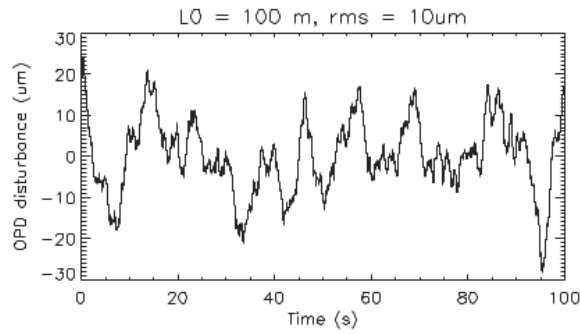


Figure 31: OPD time-series simulated by Choquet et al. (2014) for a 100m baseline including instrumental vibrations at VLTI

3.7 VARIANCE OF OPD FLUCTUATIONS

To understand the effect of interferometric baselines on the OPD fluctuations, we have to first understand the variance of the OPD fluctuations. As a power spectrum of any signal is a measure of the variance of the signal at a particular frequency, the variance of OPD fluctuations can be computed by integrating the temporal OPD power spectrum over $-\infty$ to ∞ . For a Kolmogorov like turbulence, the variance of OPD as a function of baseline is given by (Roddier, 1981),

$$\sigma_{\text{OPD}}^2(B) = 0.17\lambda^2 \left(\frac{B}{r_0} \right)^{5/3} \quad (61)$$

In the case of a von Karman power spectrum with a finite outer-scale (L_0), the variance of OPD as a function of the baseline is given by (Glindemann, 2011),

$$\sigma_{\text{OPD}}^2(B) = 0.00876\lambda^2 \left(\frac{L_0}{r_0} \right)^{5/3} \left(1 - \left(\frac{2\pi B}{L_0} \right)^{5/6} K_{5/6} \left(\frac{2\pi B}{L_0} \right) \right) \quad (62)$$

Where $K_{5/6}$ is a modified Bessel function of the second kind and $5/6$ order, also known as Macdonald function. Fig. 32 shows the influence of baselines, model of turbulence and outer scale on the variance of OPD. Here, one key thing to note is that even though the observing wavelength λ appears on the both the equations (eq. 61 & 62), the final OPD variance is independent of the observing wavelength. This is due to the fact that the Fried parameter (r_0) depends on the wavelength as,

$$r_0 \propto \lambda^{-6/5} \quad (63)$$

Hence, the λ dependence cancels each other out. The OPD variance depends mainly on the baseline (B), outer scale (L_0) and the Fried parameter (r_0).

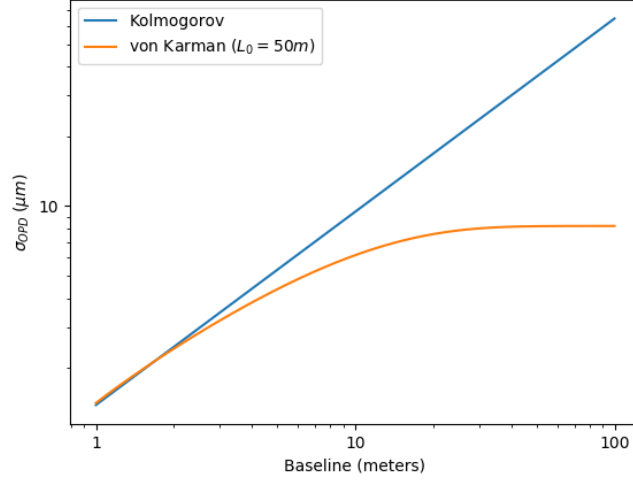


Figure 32: *Standard deviation of OPD fluctuation in an interferometer as a function of baseline, model of turbulence and outer scale*

Hence, the fluctuations on OPD keeps rising as the baseline increases in the case of Kolmogorov turbulence. In the case of von Karman turbulence, the OPD fluctuations saturates to an asymptote at baselines which are larger than the outer scale ($B \geq L_0$). Hence, the von Karman model of atmospheric turbulence with a limited outer scale (L_0) becomes important for interferometers with baselines larger than the outer scale and for a single telescope AO simulations, we can still be in the Kolmogorov regime.

Another important parameter to consider is the growth of the variance of OPD fluctuations over time. The variance of OPD fluctuations over different integration time can be estimated by applying a sliding top-hat window over the time series with a width of the integration time. Another way to estimate the OPD variance is by integrating the temporal power spectrum of the time series from the frequency corresponding to the integration time to the sample rate of the OPD signal. However, as we use a sliding top-hat filter in the time domain to estimate the OPD variance it corresponds to a convolution of the Fourier transform of the filter function on power spectral domain. Thus a top hat function with a width of T will result in a filter function on the power spectrum as shown in eq. 64.

$$F(k) = 1 - \text{sinc}^2(\pi T k) \quad (64)$$

Figure 33 shows the filter function for a 1 second wide top-hat filter on a Kolmogorov power spectrum for a baseline of 80 meters. The blue curve shows the Kolmogorov

power spectrum for a baseline of 80 meters with a wind velocity of 10m/s, the orange curve shows the filter function for 1 second integration time through eq. 64 and the green curve shows the filtered power spectrum. Hence, the variance or the RMS of the OPD fluctuations can be estimated by integrating the filtered power spectrum over all the frequencies. Fig. 34 shows the comparison of the rise in the RMS of OPD over integration time by estimating it from both temporal and power spectral domains.

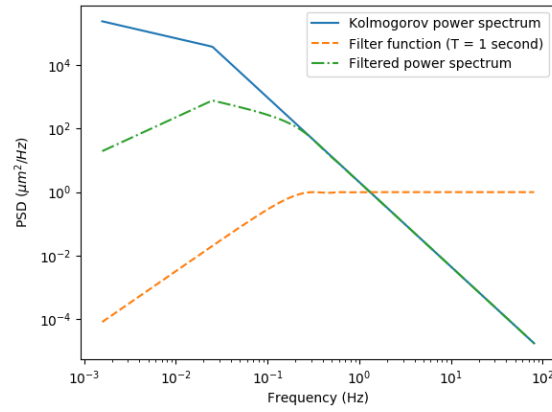


Figure 33: Filtered and unfiltered Kolmogorov temporal power spectrum for a baseline of 80 meters and integration time of 1 second. The orange dashed curve shows the filter function for a box width of one second. The solid blue curve shows a typical Kolmogorov power spectrum. The green dashed dotted lines shows the filtered Kolmogorov power spectrum.

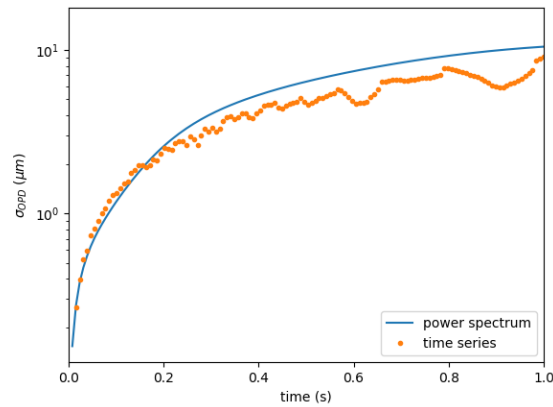


Figure 34: Growth of σ_{OPD} over integration time estimated in both temporal and power spectral domain.

3.8 STREHL RATIO - MARÉCHAL'S APPROACH

The strehl ratio is defined as the ratio of the peak of the observed PSF to the theoretical Intensity peak of the PSF. The strehl ratio is useful in understanding effects of atmospheric turbulence on the observed data. In the case of interferometry, the strehl ratio represents the loss in fringe contrast (visibility amplitude) due to the atmospheric turbulence. Maréchal (1947) used a Taylor series approximation and derived a relation between the Strehl ratio and σ_{OPD} .

There are two ways to derive the loss of strehl ratio due to atmospheric turbulence. The first approach is suggested by Ross (2009), which uses the Fourier propagation of the wavefront. If $\hat{I}_\sigma(k_x, k_y)$ & $\hat{I}(k_x, k_y)$ are the Fourier transforms of the aberrated and theoretical PSF of an incoming wavefront given by,

$$E(x, y) = U(x, y) \exp(-2\pi j \phi(x, y)) \quad (65)$$

Where $U(x, y)$ is the amplitude and $\phi(x, y)$ is the phase of the wavefront. The Strehl ratio can then be represented as,

$$S = \frac{I_\sigma(0, 0)}{I(0, 0)} \quad (66)$$

Substituting, the incoming wavefront from eq. 65 on eq. 66,

$$S = \frac{|\int U(x, y) \exp(-2\pi j \phi(x, y)) dx dy|^2}{|\int U(x, y) dx dy|^2} \quad (67)$$

Assuming a uniform illumination (U) over both the telescope apertures,

$$S = \frac{|U \int \exp(-2\pi j \phi(x, y)) dx dy|^2}{|U \int dx dy|^2} \quad (68)$$

Substituting, the total area of both the apertures given by $A = \int dx dy$.

$$S = \left| \frac{1}{A} \int \int \exp(-2\pi j \phi(x, y)) dx dy \right|^2 \quad (69)$$

Applying a Taylor's expansion on the exponential function and neglecting terms higher than the 2nd order,

$$S = \left| \frac{1}{A} \iint (1 + 2\pi j \phi(x, y) + \frac{1}{2} (2\pi j \phi(x, y))^2) dx dy \right|^2 \quad (70)$$

Assuming,

$$\Phi_n = \frac{1}{A} \iint \phi^n(x, y) dx dy \quad (71)$$

Hence eq. 70 becomes,

$$S = |1 + 2\pi j \Phi_1 - 2\pi^2 \Phi_2| = (2\pi \Phi_1)^2 + (1 - 2\pi^2 \Phi_2)^2 = 4\pi^2 \Phi_1^2 + 1 + 4\pi^2 \Phi_2^2 - 4\pi^2 \Phi_2 \quad (72)$$

We neglect the term $(4\pi^2 \Phi_2^2)$ as it represents the small variations due to the square of the 2nd order fluctuations. Hence we can simplify the above equation to,

$$S = 1 - 4\pi^2 (\Phi_2 - \Phi_1^2) \quad (73)$$

The RMS on phase can be defined as a function of the independent phase at a point (x,y) and the average phase Φ_1 as,

$$\begin{aligned} \sigma_\phi^2 &= \frac{1}{A} \iint (\phi - \Phi_1)^2 dx dy \\ &= \frac{1}{A} \left(\iint \phi^2 dx dy + \Phi_1^2 \iint dx dy - 2\Phi_1 \iint \phi dx dy \right) \\ &= \Phi_2 + \Phi_1^2 - 2\Phi_1^2 = \Phi_2 - \Phi_1^2 \end{aligned} \quad (74)$$

Combining eq. 72 & eq. 74,

$$S = 1 - 4\pi^2 \sigma_{\text{phi}}^2 = \exp(-2\pi\sigma_{\phi})^2 \quad (75)$$

Figure 35 shows the Maréchal's approximation on the loss of visibility amplitude of a point (unresolved) source due to atmospheric turbulence for a Kolmogorov like turbulence on an interferometer with 80 meters baseline.

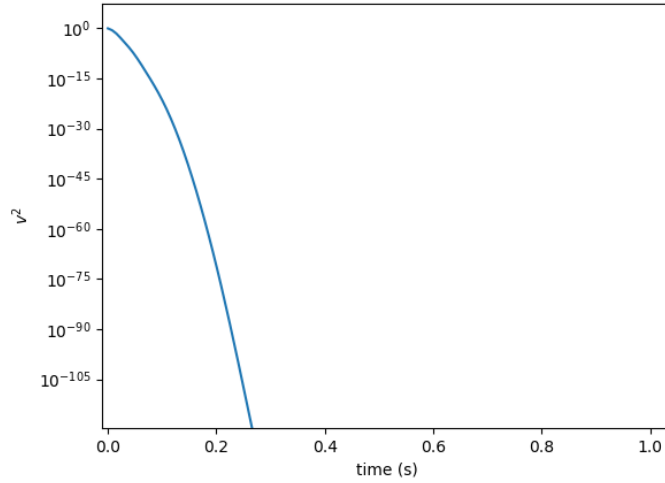


Figure 35: Maréchal's approximation of the loss in visibility amplitude due to atmospheric turbulence of a spatially unresolved source in the K band at a baseline of 80 meters.

3.9 DEVIATION FROM MARÉCHAL'S APPROXIMATION

3.9.1 Random walk model

The Maréchal approximation works for shorter integration times ($t_{\text{int}} \leq 1.78\tau_0$) (Buscher & Longair, 2015). However, numerical simulations shows us that at longer timescales the decorrelation on the temporal phase structure due to the outer scale of the atmosphere dominates. Hence, the phase fluctuations over the two telescopes behaves independently. We can thus model the loss in fringe contrast due to such decorrelation by a random walk model. Due to the temporal decorrelation of the phase difference between the telescopes, the phase fluctuations at such timescales is randomly distributed. Thus the contrast degradation (Strehl loss) due to the phase fluctuations can be described by rewriting eq. 69 as,

$$S = \frac{1}{n} \sum_{k=1}^n e^{i\phi_k} \quad (76)$$

Where n is the total number of sample points on the phase difference time series and ϕ_k is the phase difference in the time interval $k\tau_0$. Each sample of ϕ_k is from a Gaussian distribution between -2π and 2π with its center around 0. Hence, the loss in contrast goes as $1/\sqrt{n}$ or in the time domain as,

$$S = \sqrt{\frac{\tau_0}{t}} \quad (77)$$

Where t is the integration time. Figure 36 shows the comparison of the loss of contrast due to Maréchal's approximation and due to random walk model with a numerical simulation of loss of contrast of a K band broadband fringes for a baseline of 80m.

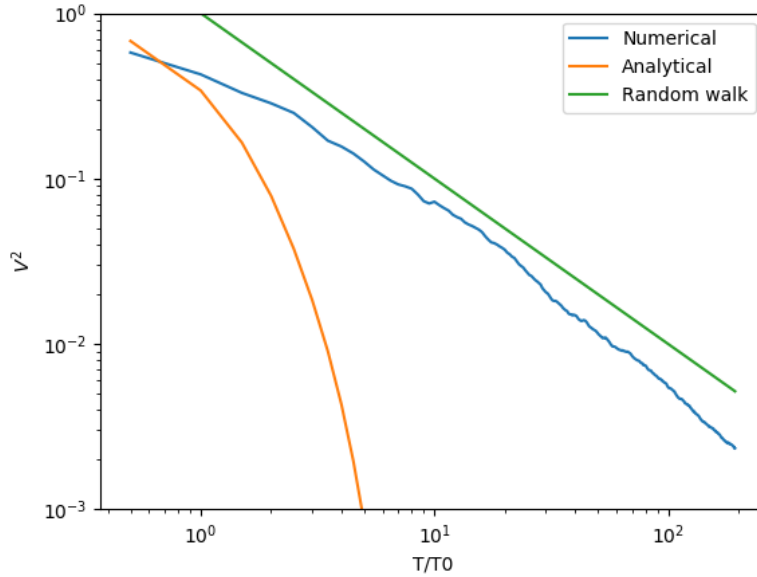


Figure 36: *Loss of visibility amplitude due to Maréchal (analytical) approximation and random walk model with simulated numerical K band broadband fringe contrast loss*

3.9.2 Longer time scale OPD drift

At even longer integration time ($t_{\text{int}} \gg 1\text{s}$), the errors on the telescope pointing models and the geometric delay correction at VLTI propagate into the OPD errors on the fringes. These drifts are constantly monitored at the VLTI (Štefl et al., 2012). These are linear drifts on the OPD time-series and the evolution of the Strehl ratio (fringe contrast) depend on the integration time as,

$$S = \frac{\tau_0}{t} \quad (78)$$

However, these linear drifts on the OPD occur at time scales larger than what is used in the GDsim. Hence, we neglect these longer time scale OPD errors in the simulations.

3.10 EFFECTS OF ATMOSPHERIC DISPERSION

On top of the atmospheric turbulence, the water vapor content of the atmosphere also plays a significant role in the fringe motion. The difference in dispersion between the two arms of the interferometer causes an additional path/phase delay difference on the incoming wavefront. The phase delay of a wavefront with wave number k ($\lambda/2\pi$), passing through a medium with refractive index n is given by,

$$\phi = nLk \quad (79)$$

Where L is the vacuum path length. The group delay (τ_g) due to the dispersion is defined as,

$$\tau_g = \frac{d\phi(\nu)}{d\nu} \quad (80)$$

The corresponding OPD is,

$$x_g = c\tau_g = \frac{d\phi(k)}{dk} \quad (81)$$

Combining eq. 79 & eq. 81, group delay OPD can be re-written as,

$$x_g = \frac{d(nLk)}{dk} = nL + Lk \frac{dN}{dk} \quad (82)$$

Where N is the refractivity of the medium and it is given by,

$$N = n - 1 \quad (83)$$

Thus by knowing the refractivities of each component of the atmosphere for different wavelength channels, we can estimate the dispersed path lengths.

3.10.1 water vapor refractivities

Colavita et al. (2004) calculated the water vapor and dry air refractivities by adding all the infrared resonances of water vapor and dry air from the HITRAN database. The values reported by Colavita et al. (2004) match with the refractivity models of Ciddor (1996) and Matsumoto (1982) with a 0.3% and 1.0% accuracy. However, they are off by 2.3% accuracy from the Mathar (2004) models of water vapor refractivities. This is due to the fact that Colavita et al. (2004) ignores the influence of the UV resonances of atmospheric water vapor molecules, which affects the refractivities in the second order of the Taylor expansion of the Erickson's equation.

The total refractivity(N) at a wavelength(λ) can be defined as,

$$N(\lambda) = n - 1 = \sum_i R_i(\lambda) \rho_i \quad (84)$$

Where, R_i is the specific refractivity of the component and ρ_i is the vertical column density of the component above the telescope. Using ideal gas laws the refractivity can be rewritten as,

$$N_i(\lambda) = R_i(\lambda) a_i p_i / T \quad (85)$$

Where, p_i is the partial pressure of the component and T is the temperature. Table 3 shows the ideal gas parameters for the dry air and water vapor during the observation of Colavita et al. (2004). The amount of precipitable water vapor during observations was $3 \mu\text{mm}^{-1}$.

| Parameter | Water vapor | Dry air |
|--|-------------|---------|
| $a \text{ (g m}^{-3} \text{ mbar}^{-1} \text{ K)}$ | 216.6 | 348.5 |
| Partial pressure (p) (mbar) | 1009.15 | 4.1 |
| Temperature (T)(K) | 293.16 | 293.16 |

Table 3: Ideal gas parameters for dry air and water vapor during the observation of Colavita et al. (2004)

Using the values of partial pressure and temperatures from table 3 with eq. 85 on the measured refractivities by Colavita et al. (2004), we can estimate the specific refractivities at near- & mid-infrared wavelengths. Table 4 lists the estimated specific refractivity per molecule of dry air and water vapor.

The phase delay can be written as,

| Wavelength λ (μm) | Specific refractivity of water vapor R_q (cm^2) | Specific refractivity of dry air |
|--|--|----------------------------------|
| 2.00 | 9.05e-24 | 5.312e-24 |
| 2.05 | 9.04e-24 | 5.312e-24 |
| 2.10 | 9.02e-24 | 5.312e-24 |
| 2.15 | 9.01e-24 | 5.311e-24 |
| 2.20 | 8.99e-24 | 5.311e-24 |
| 2.25 | 8.97e-24 | 5.311e-24 |
| 2.30 | 8.95e-24 | 5.310e-24 |
| 2.35 | 8.92e-24 | 5.310e-24 |
| 2.40 | 8.89e-24 | 5.310e-24 |
| 3.50 | 8.84e-24 | 5.307e-24 |
| 3.60 | 8.81e-24 | 5.307e-24 |
| 3.70 | 8.77e-24 | 5.306e-24 |
| 3.80 | 8.74e-24 | 5.306e-24 |
| 3.90 | 8.70e-24 | 5.306e-24 |
| 4.00 | 8.67e-24 | 5.305e-24 |
| 9.00 | 7.41e-24 | 5.305e-24 |
| 9.50 | 7.10e-24 | 5.305e-24 |
| 10.00 | 6.79e-24 | 5.305e-24 |

Table 4: Specific refractivities of dry air and water vapor at infrared wavelengths

$$x_\phi(\lambda) = N(\lambda)L \quad (86)$$

Equation 82 can be rewritten to wavelength as,

$$x_g = NL - L\lambda \frac{dN(\lambda)}{d\lambda} \quad (87)$$

Thus we can define a dispersion parameter, which is the difference between phase and group delay at a wavelength (λ) as,

$$D(\lambda) = x_\phi - x_g = \lambda \frac{dN(\lambda)}{d\lambda} L = \lambda \frac{dR(\lambda)}{d\lambda} \Sigma_{vv} L \quad (88)$$

The key parameter to consider in fringe tracking is the differential dispersion between the arms of the interferometer. The difference in the path delay between both the arms of the interferometer caused due to the difference in densities of water vapor plays a key role. Hence, difference in the refractivities between the arms of the interferometer is represented as $N(\lambda) = R(\lambda)\Sigma$. Where, Σ is the differential water vapor column density.

As we have the specific refractivities of water vapor and dry air for different near- & mid-infrared wavelengths, which is a static parameter, we have to simulate the fluctuations on differential water vapor column density. [Lay \(1997\)](#) suggested that the fluctuations of the water vapor column densities behaves as a Kolmogorov turbulence with a large outer scale. The outer scales of water vapor layers was measured by [Lay \(1997\)](#) to be ~ 10 kms. As the baselines of optical/infrared interferometers that are currently operational are small compared to the outer scale of water vapor turbulence, we can assume the water vapor turbulence to follow the Kolmogorov turbulence models. [Colavita \(2010\)](#) measured the differential water vapor column density fluctuations and estimated the power spectral coefficients by comparing phase and group delay measurements at Keck Interferometer. Figure 37 shows the Kolmogorov like power spectrum at low frequencies for dry air and water vapor measured at the Keck interferometer ([Colavita, 2010](#)).

As the effective wind speed is lower for water vapor as compared to that of the dry air, the coherence time (τ_0) of water vapor fluctuations is a factor of 65 times larger than that of the dry air ([Colavita, 2010](#)). The measured power spectral parameters for water vapor and dry air is tabulated in table 5.

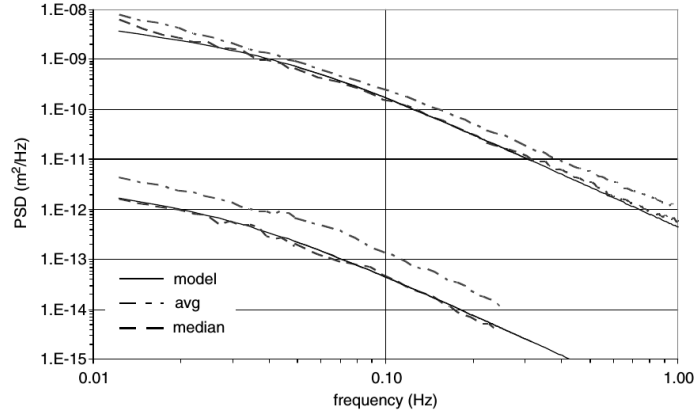


Figure 37: Dry air and water vapor temporal power spectral densities measured at Keck interferometer at a baseline of 82meters (Colavita, 2010). The upper curves are for dry air and the lower curves are water vapor fluctuations

| Parameter | dry air | water vapor |
|--|-----------------------|-----------------------|
| Power spectral coefficient ($\text{m}^3\text{Hz}^{5/3}$) | 4.5×10^{-13} | 1.1×10^{-16} |
| cut-off frequency (Hz) | 0.046 | 0.032 |
| Coherence time at $0.05\mu\text{m}$ (s) | 0.008 | 1.20 |

Table 5: Power spectral parameters for water vapor and dry air measured at the Keck Interferometer at a baseline of 82 meters and a wind velocity of 10m/s (Colavita, 2010)

Hence to simulate the effects of dispersion due to water vapor in our simulations, we simulated a second time series for the fluctuations of the differential column densities of the atmospheric water vapor. Figure 38 shows the simulated water vapor differential column density fluctuations.

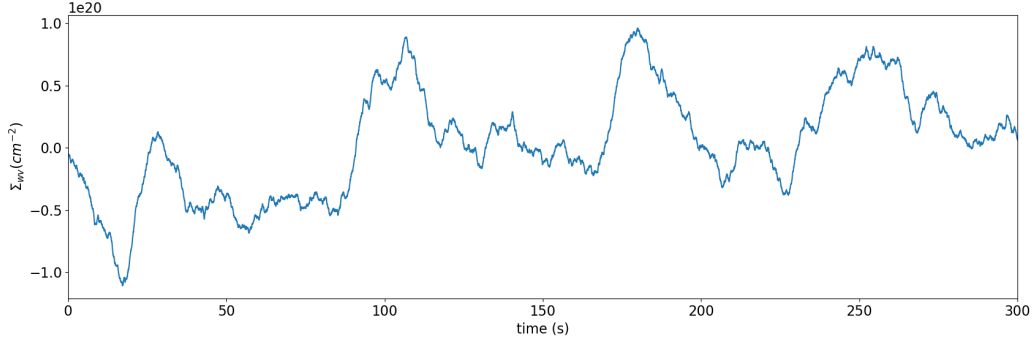


Figure 38: *Simulated differential water vapor column density fluctuations between two arms of an interferometer separated by a baseline of 80m*

Masson (1994) measured the differential water vapor column density fluctuations at Mauna Kea for a 100 meter baseline and found the rms of Σ_{wv} for a period of 15 minutes to be,

$$\sigma_{15}(\Sigma_{wv}) = 3.7 \times 10^{19} \text{ cm}^{-2} \quad (89)$$

Hence, we scaled the value to an 80 meter baseline with eq. 61. Fig. 39 shows the water vapor differential column density fluctuations measured at Keck interferometer (Koresko et al., 2006).

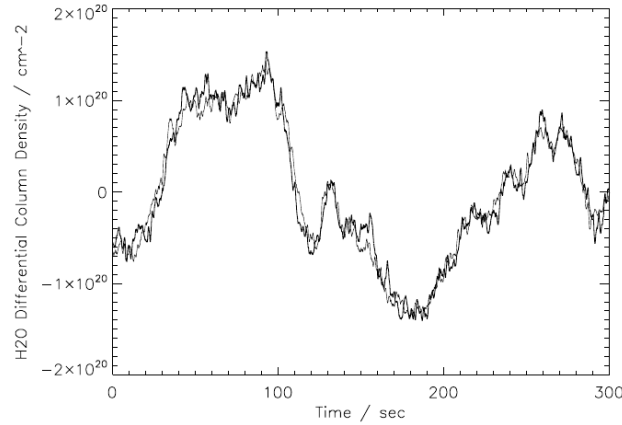


Figure 39: *Measured water vapor differential column density fluctuations at Keck interferometer (Koresko et al., 2006) on a relatively larger humidity as compared to the observation of Masson (1994).*

Another key parameter to analyze is the RMS of the OPD fluctuations at each wavelength channel with reference to the dry air OPD. This is known as intra-band dispersion.

For example, monochromatic fringes at $2.2\mu\text{m}$ will fluctuate due to water vapor seeing as,

$$\sigma_{2.2}^{wv} = (R_{2.2}^{wv} - R_{2.2}^{\text{dry}}) \sigma_{15}(\Sigma_{wv}) = -0.6\mu\text{m} \quad (90)$$

The effects of the differential dispersion due to water vapor in the atmosphere can thus be integrated to the simulator by using the dry air time series as the undispersed time series of OPD and applying the differential dispersion through eq. 88.

3.11 NON-KOLMOGOROV TURBULENCE

There can be significant deviations from the standard Obukhov-Kolmogorov model of atmospheric turbulence (Kerr, 1972). These deviations are highly inhomogenous and anisotropic in nature. There are various ways in which the atmospheric turbulence can vary from the standard, some of them are,

- Energy transport by convection between different layers of the atmosphere.
- Deviations in the stratospheric and free tropospheric turbulence from the Obukhov-Kolmogorov model
- Localized thermal fluctuations due to the geography of the telescope site

The Kolmogorov model of turbulence assumes that the initial supply of thermal energy into turbulent eddies is fed through solar radiation. However, there are other sources of thermal energy for turbulent eddies. The ground layer of the atmosphere can attain higher thermal energy from geothermal sources and human activities. Buildings and human settlements around the telescope site can add to the thermal energy source to the ground layer. This makes the lower layers of the atmosphere convectively unstable causing convective transfer of heat between the layers. These convections cause localized deviations from the standard Obukhov-Kolmogorov model.

The troposphere can be separated into two regions separated by the thermal inversion layer, the Atmospheric Boundary Layer (ABL) or also known as Planetary Boundary Layer (PBL) is the layer of troposphere below the inversion layer and the layer above the inversion layer is called as the free troposphere. The free troposphere and the stratosphere is also strongly affected by the tidal forces due to the gravity of moon and the sun (as compared to the tides on the ocean) (Gurvich & Belen'kii, 1995). These changes on the density of different layers of the atmosphere causes shifts on the optical path difference.

Zilberman et al. (2008) measured the anisotropic power spectrum of the non-Kolmogorov turbulence with a three layer turbulence. However as the models are computationally extensive, GDsim uses a homogeneous and isotropic Kolmogorov/von Karman model of atmospheric turbulence.

3.12 COMPARISON WITH FINITO DATA

Fringe-tracking Instrument of NIce and TORino (FINITO) is a first generation fringe tracker at VLTI which does simultaneous 3 telescope fringe tracking. FINITO uses bulk optics to estimate the group and phase delay using four $\pi/2$ phase shifted measurements (ABCD) in the H band. Fig. 40 shows the layout design of FINITO.

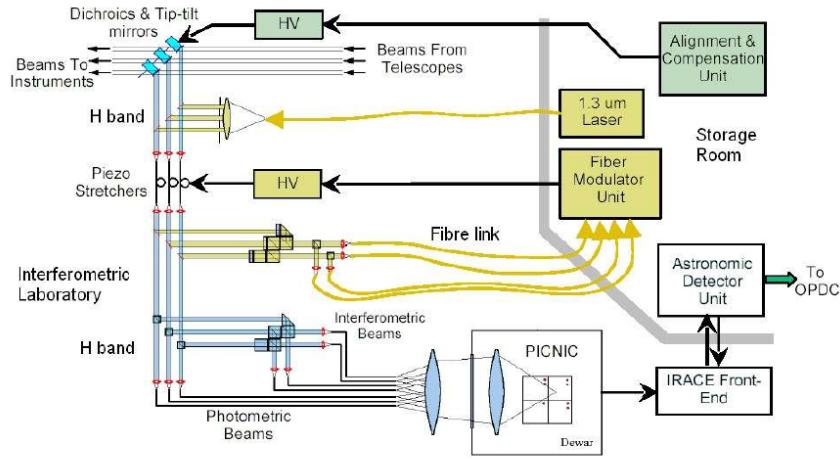


Figure 40: design layout of FINITO fringe tracker at VLTI (Gai et al., 2004)

I used the calibration data of Amber instrument (Program ID: 094.D-0572(A) & 094.D-0572(C)) which was fringe tracked by FINITO and retrieved the closed-loop group and phase delay data. The observations were done with the Auxiliary telescopes of VLTI at the stations A1, G1, K0, B2, C1 and baselines,

- A1-G1: 80.01 meters
- G1-K0: 63.98 meters
- A1-K0: 129.0 meters
- A1-B2: 11.31 meters
- A1-C1: 15.99 meters
- B2-C1: 11.30 meters

The Amber observations were made to measure the angular diameters of 21 stars which will be later used by Gaia mission as a golden standards to estimate the effective temperatures of the star with higher accuracy. The calibrators chosen for the observation were 31Ori (HIP27288) and α -Tau. Fig. 41 shows the on-source H band closed-loop group delay of 31Ori measured with baselines A1-G1-K0. Fig. 42 shows the on-source H band closed-loop group delay of α -Tau measured with baselines A1-B2-C1.

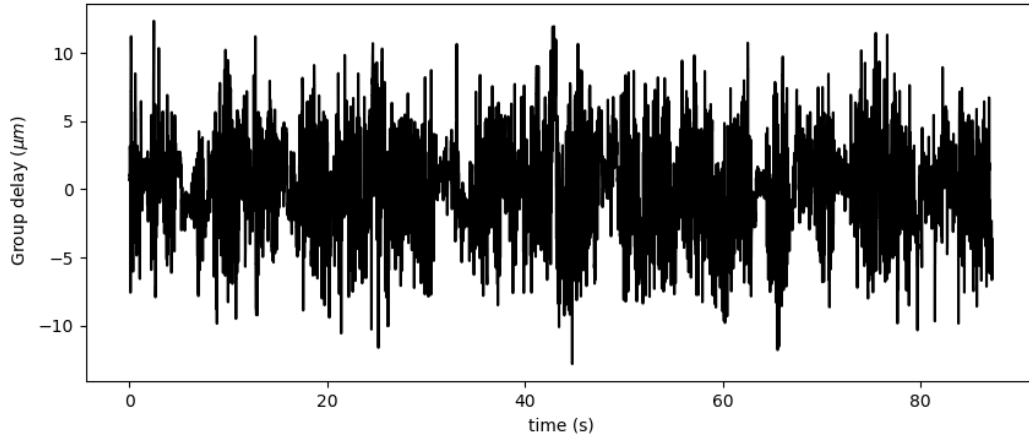


Figure 41: *H band closed-loop group delay measurements of 31Ori measured with FINITO fringe tracker at VLT*

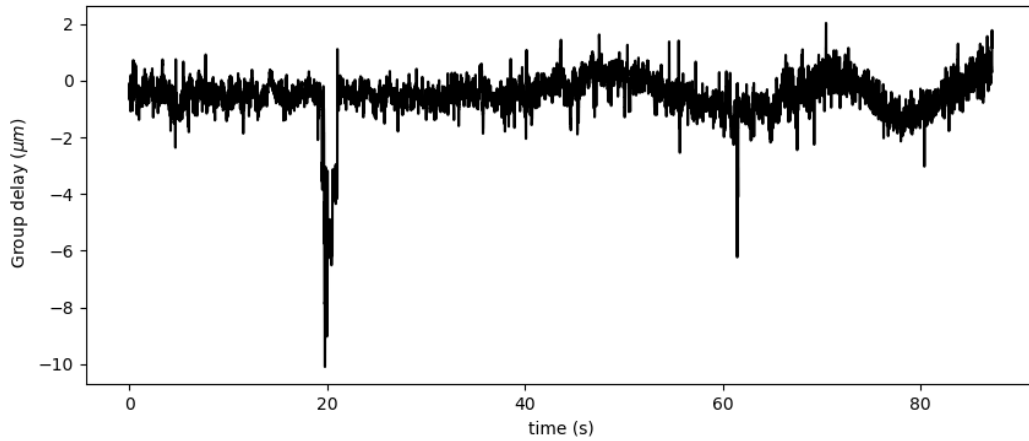


Figure 42: *H band closed-loop group delay measurements of α -Tau measured with FINITO fringe tracker at VLT*

Figures 43 & 44 shows the power spectra of the group delay time series shown in figures 41 & 42. The closed-loop power spectra shows a von Karman like power

spectra. However, as the time series is that of a closed-loop system and the analytical Kolmogorov/von Karman power spectra is for an uncorrected atmospheric turbulence we cannot directly fit the analytical power spectra with the measured power spectra.

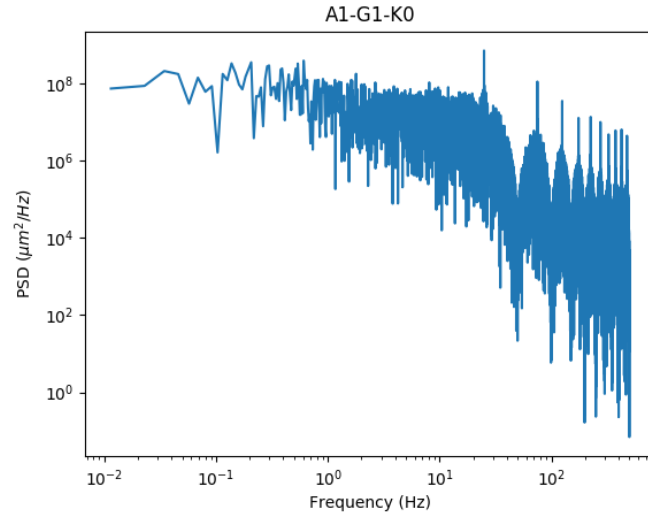


Figure 43: Normalized power spectrum of group delay fluctuations shown in fig. 41.

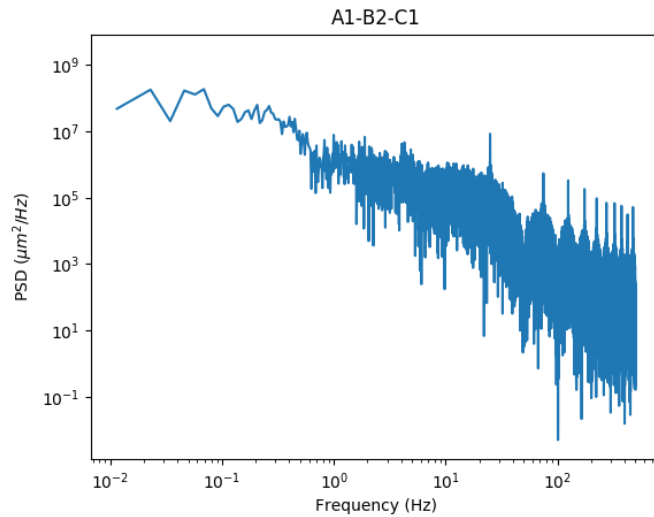


Figure 44: Normalized power spectrum of group delay fluctuations shown in fig. 42.

In fig.42, we can note two sharp deviations from the group delay time series at 20 seconds and at 63 seconds. These two sharp features could arise from the non-Kolmogorov like turbulence or a control system error.

3.13 BIREFRINGENCE

Another property of light that reduces the fringe contrast is the polarization of the incoming stellar light. When the two beams of the light combined in the interferometer has different angles of polarization resulting in difference in refractive indices and thus a change in the phase of the wavefront which then reduces the contrast of the fringes. This property is known as Birefringence. In the case of a typical stellar interferometer, the contribution of atmospheric turbulence on the polarization of the light is insignificant (Ji & Pu, 2009). However, the polarization effects of the instruments at VLTi can reduce the resulting fringe contrast significantly. The effect of birefringence at VLTi for the Gravity instrument has been extensively modeled by Lazareff et al. (2014). As the effect of birefringence is purely instrumental, it can be calibrated on the resulting fringes. Thus, we have excluded the polarization effects from our simulations.

SIGNAL TO NOISE RATIO AND SENSITIVITY

Signal to Noise Ratio (SNR) is the best measure to estimate the sensitivity of an astronomical instrument. But before understanding the ratio, let us first understand the different noise involved in any astronomical observation.

4.1 NOISE

4.1.1 *Photon/Shot Noise*

Charge Coupled Device (CCD) acts as a light collecting bucket with an array of photo-receptors which converts the incoming photons into photo-electrons. The photon counting method has a Poisson distribution with the peak at the total number of photons (N) collected and a standard deviation of \sqrt{N} . This noise is known as photon noise or shot noise. This noise can be overcome by increasing the integration time or by stacking multiple frames.

4.1.2 *Detector Noise*

Read Noise

The read noise of a detector is an inherent noise that is specific to the detector. During the readout of the photo-electrons, the detector has other sources which can contribute to the noise on the final count of photo-electrons. This is known as the read noise of the detector. The read noise contributes to the total noise as,

$$\sigma_{RN}^2 = N_{pix} \times RN^2 \quad (91)$$

The read noise of the GRAVITY fringe tracker detector is 3e[−] RMS and about 15e[−] RMS for MATISSE L band detector.

Dark Current

Dark current mainly affects the infrared observations. Even in the absence of incoming photons the detector and its associated electronics can emit radiation which can then be read by the detector. The dark current for the GRAVITY fringe tracker at 80 Kelvin is 100e[−] /s/pixel.

4.1.3 Thermal Background

Near- and mid- infrared wavelengths are also affected by the thermal background of the atmosphere and the instruments. The atmosphere at 300K acts as a blackbody and radiates in the near- and mid-infrared wavelengths given by the Planck's blackbody radiation law given by,

$$B(\lambda) = \frac{2hc^2}{\lambda^5} \frac{1}{\exp\left(\frac{hc}{\lambda K_B T}\right) - 1} \quad (92)$$

Where,

- $h \rightarrow$ Planck's constant
- $c \rightarrow$ Velocity of Light
- $T \rightarrow$ Temperature of the black body
- $K_B \rightarrow$ Boltzmann constant

The thermal background at near- and mid-infrared wavelengths for a typical Paranal atmospheric conditions which includes the atmospheric transmission is shown in fig. 45. The typical values of the background radiation in the K band is about 10^{-2} Jy/as² and 5 Jy/as² in the L band.

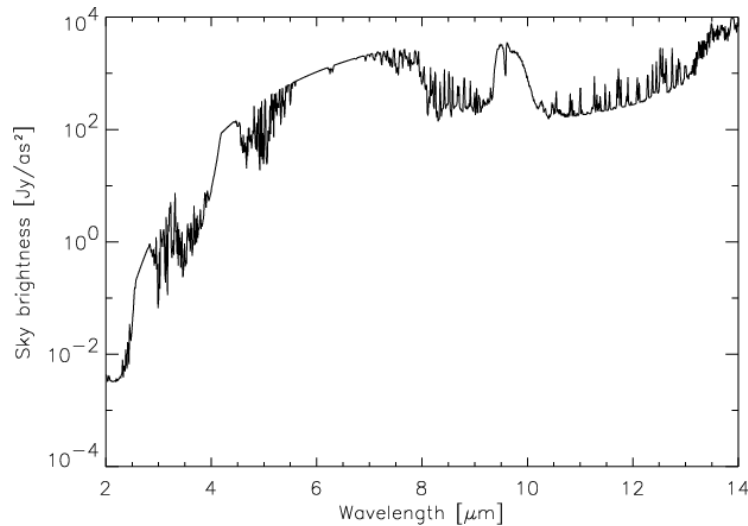


Figure 45: Thermal background for Paranal, Chile (*Absil et al., 2006*)

The instrumental background at the K band for an ambient temperature of 290K is $4.5 \times 10^{-3} \text{ Jy/as}^2$ in the K band and 7.3 Jy/as^2 in the L band for the VLTI.

There are two ways to subtract background radiation at an interferometer.

Chop-nod method

The chop-nod technique uses simultaneous observations of two fields namely, Astronomical Source+Thermal background and just the Background. The pure background image can then be subtracted from the data. Typical chopping time scale is 30ms at VLTI. However, the background flux experiences temporal variations, thus the efficiency of chopping depends on the time scales. Thus by using eq.29 we can define a temporal structure function of the background flux as,

$$D_B(\tau) = \langle |n_B(t) - n_B(t + \tau)|^2 \rangle \quad (93)$$

Figure 46 shows the temporal structure function measured at VLTI using MIDI data (Matter et al., 2016).

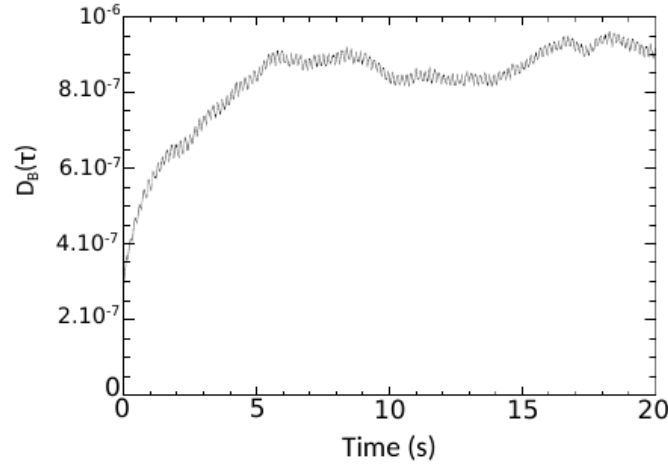


Figure 46: Thermal background structure function measured at VLTI using MIDI data (Matter et al., 2016)

This temporal structure function gives rise to a background rejection factor. The background rejection factor can be considered as a residual background noise after the chop-nod correction. The background rejection factor is given by,

$$\gamma = \frac{\sqrt{D_B(2/f_{\text{chop}})}}{\bar{B}} \quad (94)$$

Where f_{chop} is the chopping frequency and \bar{B} is the average background photons in the image.

Phase Modulation

We can overcome the problem with the background structure function by adding a phase modulation to the interferometric fringes. It is based on the fact that the thermal background radiation is spatially incoherent compared to the astronomical source. Thus, by producing two fringes with a π phase shift between them simultaneously of the same source, we can effectively remove the background by subtracting the two fringes. This will remove the spatially incoherent background radiation while improve the signal of the source. This technique has been used in the MIDI instrument at VLT (Leinert, 2003).

Currently with the development of X-shaped couplers on integrated optics beam combiners, where the two outputs of the coupler are stable π phase shifted fringes. Hence, in our simulations we have mainly considered the shot noise of the background flux which is still a dominant noise source at longer infrared wavelengths.

4.2 SNR ON THE FLUX OF THE SOURCE

The SNR on the flux of the source is a key number to estimate the sensitivity of a single telescope. The SNR on flux is the ratio of the incoming number photons (N) and the associated noises given by,

$$\text{SNR}_{\text{flux}} = \frac{N}{\sqrt{N + B + (N_{\text{pix}} \times RN^2)}} \quad (95)$$

In the case of chop-nod background subtraction, the signal to noise ratio is given by,

$$\text{SNR}_{\text{flux}} = \frac{N}{\sqrt{N + B + (N_{\text{pix}} \times RN^2) + (\gamma^2 B^2)}} \quad (96)$$

In a simple case where the data is shot noise dominated, we can neglect the effects of background and the detector noise. Thus the signal to noise ratio will evolve purely of Photon flux as,

$$\text{SNR}_{\text{flux}} = \frac{N}{\sqrt{N}} \quad (97)$$

Fig. 47 shows the evolution of the simple SNR_{flux} over time.

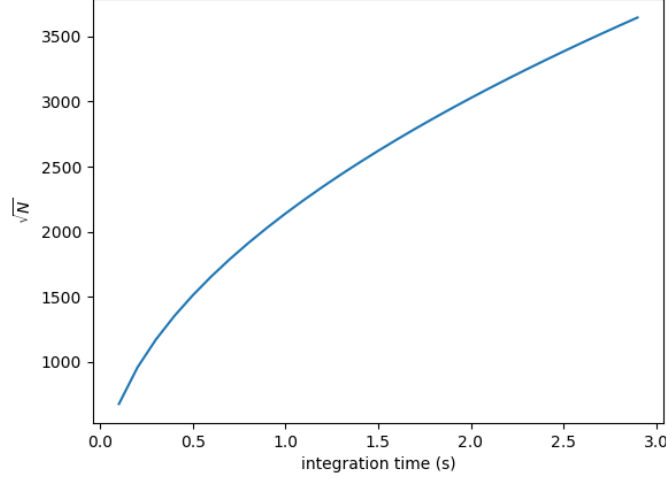


Figure 47: Evolution of simple SNR_{flux} over time for a 6th magnitude star

4.3 SNR ON THE CORRELATED FLUX

The SNR on the correlated flux is defined as the product of the SNR_{flux} and the fringe contrast (v) (Petrov et al., 2016).

$$\text{SNR}_c = \frac{Nv}{\sqrt{2N + 2B + (N_{\text{pix}} \times RN^2)}} \quad (98)$$

For a two telescope interferometer, as the shot and the background noise depends on the total number of photons collected at both the telescopes, a factor of $\sqrt{2}$ is included for the shot noise of the source and the background flux.

The typical threshold SNR on the correlated flux of 5 is assumed to mark the sensitivity limits of the instrument. To understand the evolution of SNR on the correlated flux over integration time we need to understand the evolution of fringe contrast over integration time. §3.8 describes the loss of fringe contrast due to the Kolmogorov model of the atmospheric turbulence. However, at longer integration time ($t_{\text{int}} \geq 1.78\tau_0$), the random

walk model as described in §3.9.1 dominates. Hence, the loss in fringe contrast depends on the integration time as $1/\sqrt{t}$.

The simplified signal to noise ratio on flux given by eq. 97 which depends on the integration time as \sqrt{t} , multiplied by the random walk behavior of the loss in fringe contrast which goes as $1/\sqrt{T}$ will yield an asymptote for the SNR_c . Thus the signal to noise ratio on the correlated flux becomes unreliable for estimating the sensitivity over longer integration time. The asymptotic behavior of the SNR_c over integration time using the simulated numerical fringe contrast loss is shown in fig. 48.

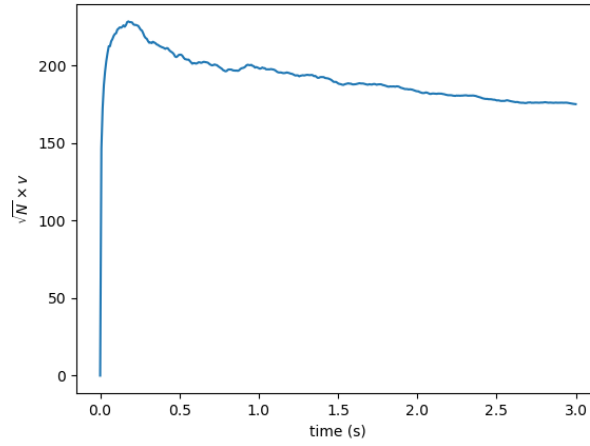


Figure 48: Evolution of simplified SNR_c over integration time using the simulated numerical fringe contrast

4.4 NOISE ON THE MEASUREMENT OF PHASE

Even though the SNR_c is not robust at large integration time, it can be used to estimate the sensitivity of various measurements at short integration times ($t < 1.78\tau_0$). One of the key measurements is the phase of fringes. The noise on the measurements of phase is given by (Petrov et al., 1986),

$$\sigma_\phi = \frac{1}{\sqrt{2}\text{SNR}_c} \quad (99)$$

The factor of $\sqrt{2}$ arises due to the cross correlation of the irradiances at both the telescopes of the interferometer.

4.5 NOISE ON THE GROUP DELAY MEASUREMENTS

Another key parameter to consider is the noise on the group delay measurement. [Lawson et al. \(2000\)](#) derived a relation between the noise on the group delay measurement and the signal to noise on the correlated flux as,

$$\sigma_{gd} = \frac{\sqrt{12}}{2\pi} \frac{1/\Delta k}{\text{SNR}_c} \quad (100)$$

Where Δk is the coherence length of the band and it is given by,

$$\Delta k = \frac{\Delta \lambda}{\lambda_c^2} \quad (101)$$

4.6 SIMULATING NOISY TWO TELESCOPE FRINGES

Now that we have the atmospheric turbulence simulated for various conditions using GDsim, the next step is to simulate two telescope interferometric fringes which includes all the different noises as described in §4.1. We have mainly concentrated in simulating K and L band fringes at the VLTI. For K band simulations, we have used the instrumental parameters of the Gravity fringe tracker ([Choquet et al., 2014](#)), and MATISSE for the L band setup. The instrumental parameters for gravity and MATISSE is tabulated in table 6. Due to the lack of water vapor refractivity data in the L band at wavelengths between $3.0\mu - 3.5\mu$ ([Colavita, 2010](#)) (Table 4), I have simulated fringes in the L' band ($3.5\mu - 4.0\mu$) for simulations which includes the dispersive nature of the atmospheric water vapor.

| Parameter | K band (Gravity FT) | L band (Matisse) |
|---|-----------------------|------------------|
| atmospheric background (Jy/as ²) | 1.4×10^{-2} | 15.16 |
| instrumental background (Jy/as ²) | 4.5×10^{-3} | 7.3 |
| total background (Jy/as ²) | 1.85×10^{-2} | 22.46 |
| baseline (m) | 80 | 80 |
| OPD scan range (μm) | [-25 μm, 25 μm] | [-60 μm, 60 μm] |
| read noise (e-) | 3 | 15 |
| total transmission (%) | 1.0 | 0.7 |
| Fried Parameter (meters) | 0.6 | 1.0 |
| Coherence time (milliseconds) | 12.4 | 20.7 |

Table 6: *Input parameters used in simulating K and L band fringes*

Broadband and dispersed fringes are produced by using eq. 3 and summing it over different wavelength channels.

$$I_{BB} = \sum_{\lambda_i}^{\lambda_f} I_1 + I_2 + 2\sqrt{I_1 I_2} \cos\left(\frac{2\pi}{\lambda} x\right) \quad (102)$$

In Fourier space, eq. 102 will be a sum of delta functions which corresponds to the cosine function at each wavelength channel. This sum of delta functions will be convolved with a top-hat filter function which corresponds to the uniform response of the filter with a bandwidth of $\Delta\lambda$. According to the convolution theorem, convolution of two functions is the product of the Fourier transform of the functions. Hence, the sum of delta functions which is convolved with a top-hat filter in the Fourier space will correspond to a product of a sinc function (Fourier transform of the Top-hat filter function) which has a central width of the coherence length of the band (given by, $\lambda_c^2/\Delta\lambda$) and a cosine function which has a frequency corresponding to the central wavelength. The simplified broadband interferogram can be represented as,

$$I_{BB} = \text{sinc}\left(\frac{\Delta\lambda}{\lambda_c^2} x\right) \cos\left(\frac{2\pi}{\lambda_c} x\right) \quad (103)$$

Equation 103 can be alternatively derived by integrating eq.102 over the spectral bandwidth. Eq. 102 can be rewritten as,

$$I_{BB} = \int_{K_i}^{K_f} I_1 + I_2 + 2\sqrt{I_1 I_2} \cos(2\pi K x) dK \quad (104)$$

Where K is the wave number and it is related to the wavelength as $K = 1/\lambda$. Assuming the intensities at both the arms of the interferometer to be equal (ignoring the photometric imbalances) ($I_1 = I_2 = I$) and ignoring the spectral dependence of the intensities,

$$I_{BB} = 2I \int_{K_i}^{K_f} (1 + \cos(2\pi K x)) dK \quad (105)$$

Integrating the above equation we get,

$$I_{BB} = 2I \left(\left| K \right|_{K_i}^{K_f} + \left| \frac{\sin(2\pi K x)}{2\pi x} \right|_{K_i}^{K_f} \right) \quad (106)$$

Rewriting the integral limits in terms of Central wave number(K_c) and the bandwidth(ΔK) as,

$$K_i = K_c - \Delta K/2 \quad (107)$$

$$K_f = K_c + \Delta K/2 \quad (108)$$

Applying the integration limits,

$$I_{BB} = 2I \left(\Delta K + \frac{1}{2\pi x} (\sin(2\pi(K_c + \Delta K/2)x) - \sin(2\pi(K_c - \Delta K/2)x)) \right) \quad (109)$$

using the trigonometric identities we can simplify the above equation to,

$$I_{BB} = 2I \left(\Delta K + \frac{2\cos(2\pi K_c x) \sin(\pi \Delta K x)}{2\pi x} \right) \quad (110)$$

The above equation can be rewritten as,

$$I_{BB} = 2I \Delta K (1 + \cos(2\pi K_c x) \text{sinc}(\pi \Delta K x)) \quad (111)$$

4.7 POISSON NOISE AND GAUSSIAN NOISE

The noises described at the earlier part of this chapter mainly follow two distributions. The noise of an independent measurement follows a normal distribution (Gaussian noise) given by,

$$P(x) = \frac{1}{\sqrt{2\pi}\sigma} \exp\left(-\frac{(x - \mu)^2}{2\sigma^2}\right) \quad (112)$$

Where x is the random noise value, σ & σ^2 are the standard deviation and variance of the measurements and μ is the expected mean value. The nature of the Gaussian white noise is described in detail in §2.3.1.

Individual photon detection/measurements can be considered as an independent events, where each measurement of the intensity of the registered photon follows a Poisson distribution given by,

$$P(x) = \frac{\mu^x e^{-\mu}}{x!} \quad (113)$$

From Poisson statistics the width of the distribution (standard deviation) is $\sqrt{\mu}$. At high flux counts a Poisson distribution tends towards a Gaussian distribution. Fig. 49 shows the Poisson distribution for mean values of 0.5, 3.0 and 10.0.

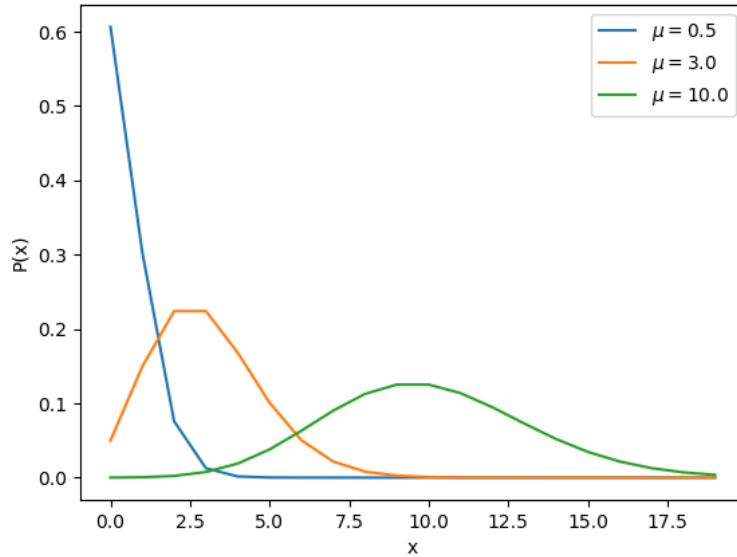


Figure 49: Poisson distributions centered around 0.5, 3.0 and 10.0

In contrast to Gaussian noise which is additive in nature, the shot noise is applied to an array of data based on the values at the corresponding pixel. In other words the Poisson noise in an image is correlated to each pixel value whereas the Gaussian noise is purely uncorrelated to the individual pixel values.

4.8 GRAVITY FRINGE TRACKER

The Gravity fringe tracker is a second generation fringe tracker at VLTI operating in the K band. It aims to co-phase the fringes to a sensitivity of $K=10$ with the UT and $K=7$ with the AT. It is the first fringe tracker on board the VLTI to use integrated optics beam combiner. Fig. 50 shows the integrated optics beam combiner of Gravity instrument and its circuit design (Gravity Collaboration et al., 2017).

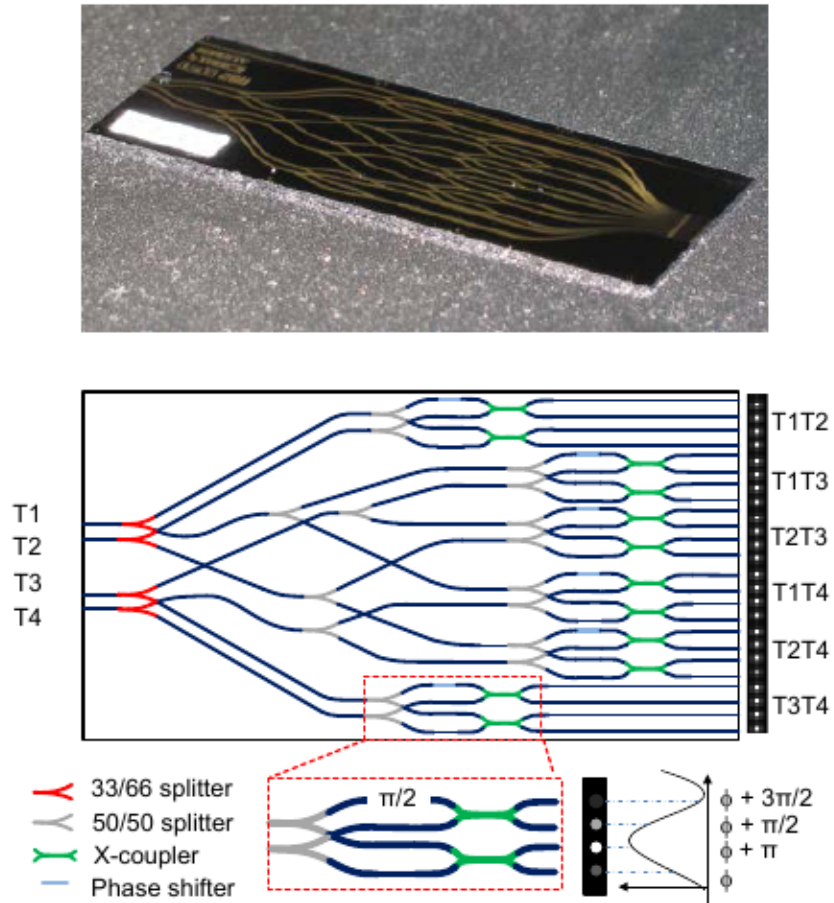


Figure 50: Integrated optics beam combiner of Gravity instrument at VLTI (Gravity Collaboration et al., 2017)

The Gravity fringe tracker estimates the phase delay from the dispersed ABCD measurements at the 6 baselines of a 4 telescope interferometer. Gravity fringe tracker uses a SELEX infrared Avalanche Photo Diode (APD) detector. The detector parameters are,

- frame rate $\rightarrow 350\text{Hz}$
- Read Noise $\rightarrow 3e^-$
- Quantum Efficiency $\rightarrow 65\%$

The fringe tracker image has a dimensions of 5×24 pixels. Each row of the detector corresponds to a spectral channel of the dispersed K band fringes. The 24 columns corresponds to the 6 baselines with 4 measurements (ABCD) each. A typical gravity fringe tracker image is shown in fig. 51.

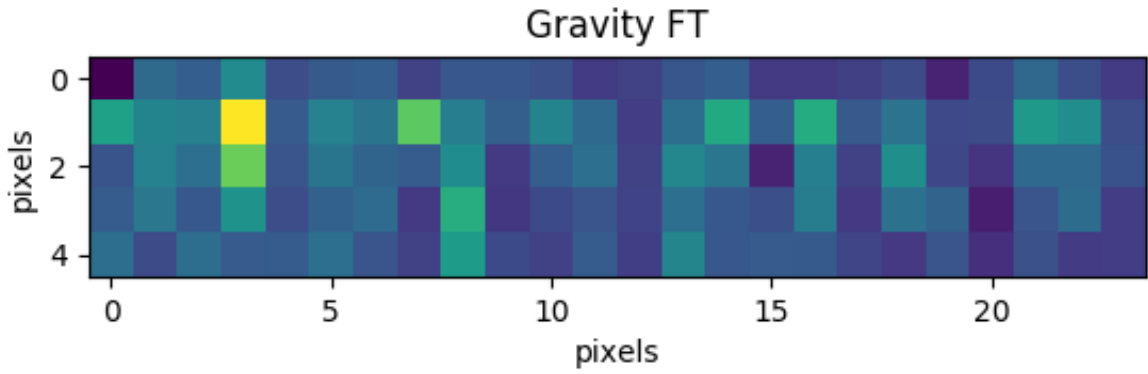


Figure 51: Sample Gravity fringe tracker image

Gravity fringe tracker can perform off-axis fringe tracking at the UT with an off-axis source at 2 arcseconds from the phase center and 4 arcseconds with the AT. Gravity can perform both group and phase delay corrections. The group delay correction is only applied when the SNR_{OPD} goes below 5. The noise on the OPD measurements between two telescopes i & j measured at a wavelength λ is given by (Houairi et al., 2008),

$$\sigma_{\text{OPD}} = \frac{\lambda}{2\pi} \frac{1}{V_{i,j}} \frac{\alpha}{\eta_{i,j} \text{SNR}_{\text{flux},i,j}} \quad (114)$$

where,

- $\eta_{i,j} \rightarrow$ Visibility attenuation factor due to photometric imbalance
- $\text{SNR}_{\text{flux},i,j} \rightarrow$ The total signal to noise ratio on the flux from both telescopes i & j as given in eq. 95
- $V_{i,j} \rightarrow$ Visibility amplitude of the source (including the losses due to atmospheric turbulence, instrumental vibrations and instrumental contrast loss)
- $\alpha \rightarrow$ coefficient depending on the beam combination technique. (ABCD - $\alpha = \sqrt{2}$, AC- $\alpha = 1$)

4.9 MATISSE

The Multi AperTure mid-Infrared SpectroScopic Experiment (MATISSE) is a next generation instrument on board of VLT. MATISSE is a 4 telescope beam combiner operating in L, M and N bands. MATISSE offers three different spectral resolutions ($R = 30, 500, 950$) for L and M bands and $R=30$ and $R = 220$ for N band observations.

On the detector MATISSE has 3 channels, 2 photometric channels and 1 interferometric channel. MATISSE observations can be done in 3 modes,

- 4TSiPhot mode \rightarrow 4 telescope simultaneous photometric and interferometric channels. Where 65% of the incoming light goes to the interferometric channel ($\alpha_i = 0.65$) and 35% of the incoming light goes to the photometric channels ($\alpha_p = 0.35$) (Matter et al., 2016).
- 2THighSens mode \rightarrow 2 telescope pure interferometric measurements. Where $\alpha_p = 0$.
- 4THighSens mode \rightarrow 4 telescope pure interferometric measurements. Where $\alpha_p = 0$.

The detector layout and sample 4 telescope fringes with the MATISSE detector is shown in fig. 52.

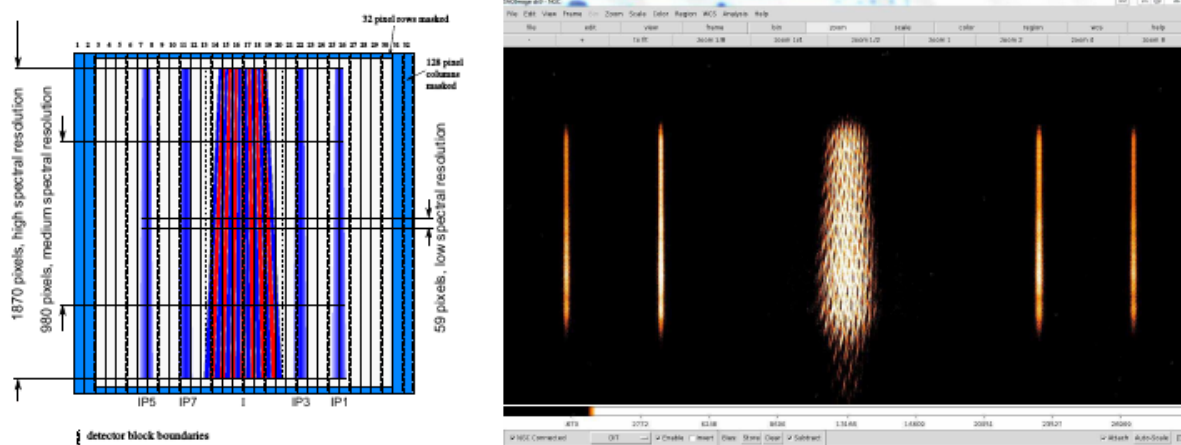


Figure 52: left: Layout of the Hawaii-2RG detector. right: Sample 4 telescope L band interferometric fringes. (Millour et al., 2016)

The parameters of the Hawaii-2RG detector used by MATISSE are,

- Read Noise $\rightarrow 15e^-$ for L and M bands & $300e^-$ for N band
- Quantum Efficiency $\rightarrow 50\%$

The PSF of each spectral channel is $1.5\lambda/D$ in size for the L and M bands and $2\lambda/D$ in size for the N band. In the spatial direction each λ/D element occupies 72 pixels on the detector in the interferometric channel and 12 pixels in the photometric channel. In the spectral direction each λ/D element occupies 3 pixels on the detector. Hence, the interferometric channel around central wavelength in the L band occupies 1550 pixels and 2977 pixels in the N band. The limiting magnitudes of MATISSE for the L band operating without a fringe tracker for different spectral resolutions and operating modes are tabulated in table 7

| R | 4TSiPhot | 4THighSens | 2THighSens |
|-----|----------|------------|------------|
| 30 | 7.6 | 8.0 | 8.1 |
| 500 | 4.95 | 5.4 | 5.45 |
| 950 | 4.25 | 4.7 | 4.25 |

Table 7: L band sensitivity (in magnitudes) of MATISSE without an external fringe tracker (Matter et al., 2016)

4.10 SIMULATED NOISY FRINGES

Using eq. 102, I have simulated broadband and dispersed fringes in K and L bands using the instrumental parameters of Gravity fringe tracker and MATISSE from table 6. In my simulations, I assumed a perfect background subtraction (using the phase modulation technique in §4.1.3), hence I have only included the shot noise of the background flux in the simulations. Figures 53 & 54 shows sample noisy broadband fringes in K and L bands respectively.

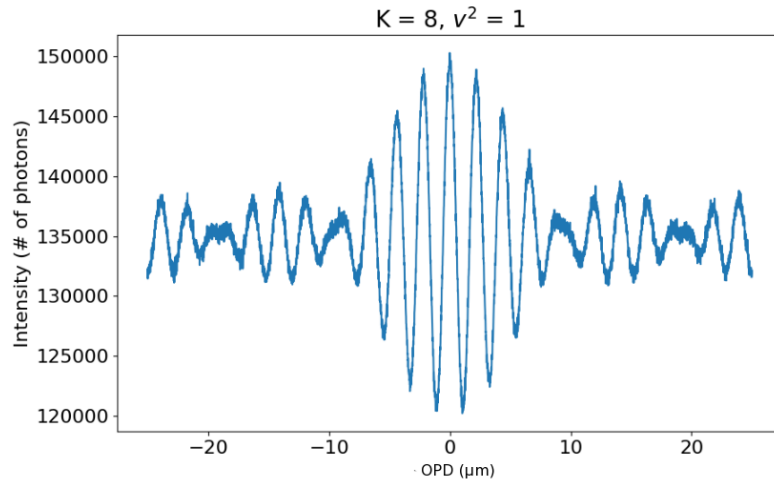


Figure 53: Sample K band noisy fringes for a 8th magnitude source with an integration time of 10ms

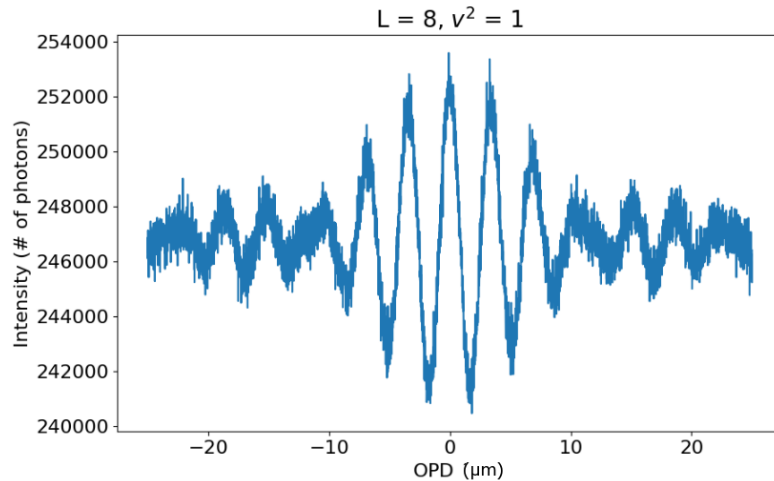


Figure 54: Sample L band noisy fringes for a 8th magnitude source with an integration time of 10ms

Figure 55 shows a sample image of dispersed($R=500$) L band noisy fringes of a 5th magnitude unresolved source.

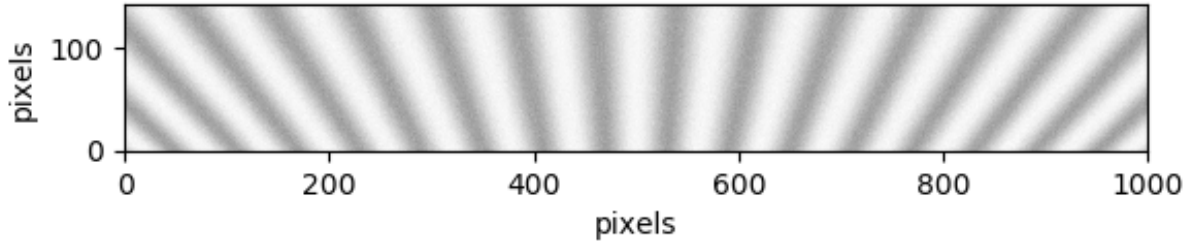


Figure 55: *Simulated dispersed fringes ($R=500$) for an unresolved source of 5th magnitude in the L band.*

4.11 LOSS IN FRINGE CONTRAST

Once the fringes are simulated, they are modulated by the corresponding OPD from the atmospheric turbulence simulator(GDsim). These individual fringe frames are then added to form the final integrated fringes which is degraded by the atmospheric turbulence and instrumental vibrations. The final fringe contrast is then estimated through equation 6. Figure 57 shows the degraded noisy fringes of a K band unresolved source of 8th magnitude after being aberrated by the simulated dry air atmospheric OPD time series shown in fig. 56. The fringes were integrated for a time of 1 second.

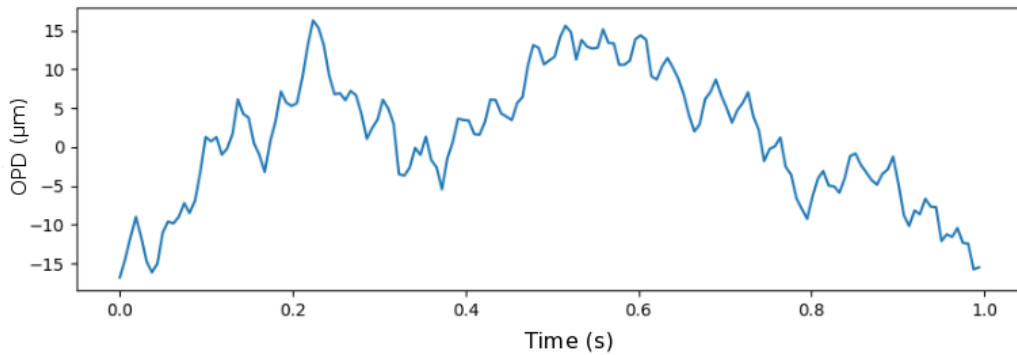


Figure 56: *Simulated dry air OPD time-series for a baseline of 80 meters and wind velocity of 10m/s*

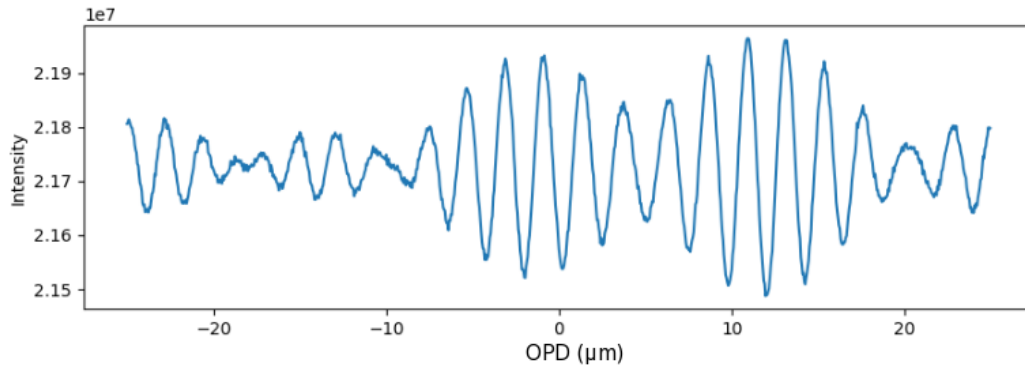


Figure 57: *K band interferometric fringes of an unresolved source of 8th magnitude, aberrated by the simulated OPD disturbance shown in fig.56 for an integration time of 1 second*

Figure 58 shows the loss in the fringe contrast over the integration time.

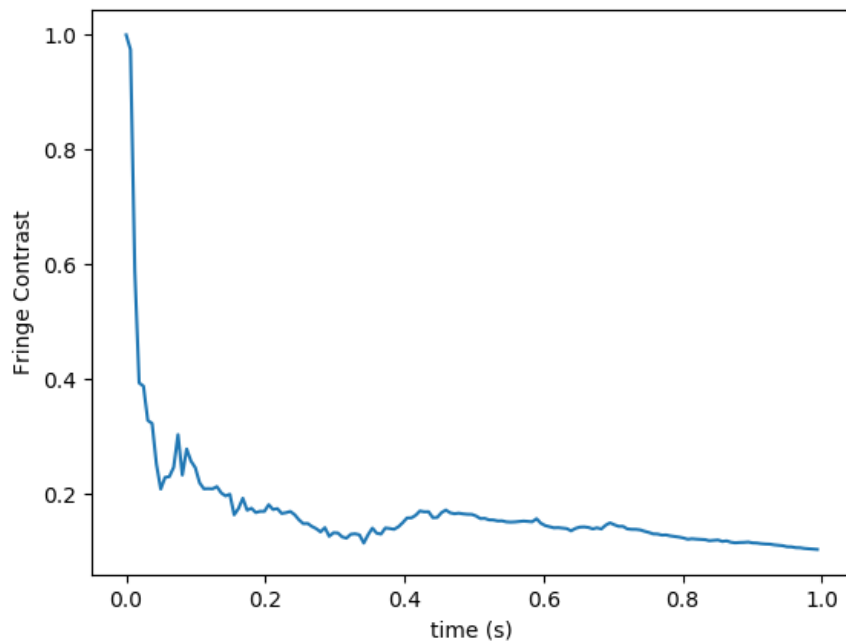


Figure 58: *Loss in fringe contrast over 1 second of integration of fringes shown in fig.57*

I have compared the fringe contrast loss with some uncorrected fringe data available within the work group. The data used was calibrator observations with AMBER instrument in K band at VLTi with the fringe tracker FINITO turned off. The sources observed were, ϵ Vir, HD170818, HD174532 and HD174240 with an integration time of 200 milliseconds. They were observed with UT1, UT2 & UT4 with baselines,

- UT1-UT3 \rightarrow 102.43 meters
- UT3-UT4 \rightarrow 62.43 meters
- UT1-UT4 \rightarrow 130.23 meters

Figure 59 shows the observed visibility amplitude using UT1-UT3 combination as compared with the simulated loss in visibility amplitude for a 100 meter baseline. As we can see that the simulated visibility amplitude matches the untracked visibility amplitude in the K band of the calibrator observations.

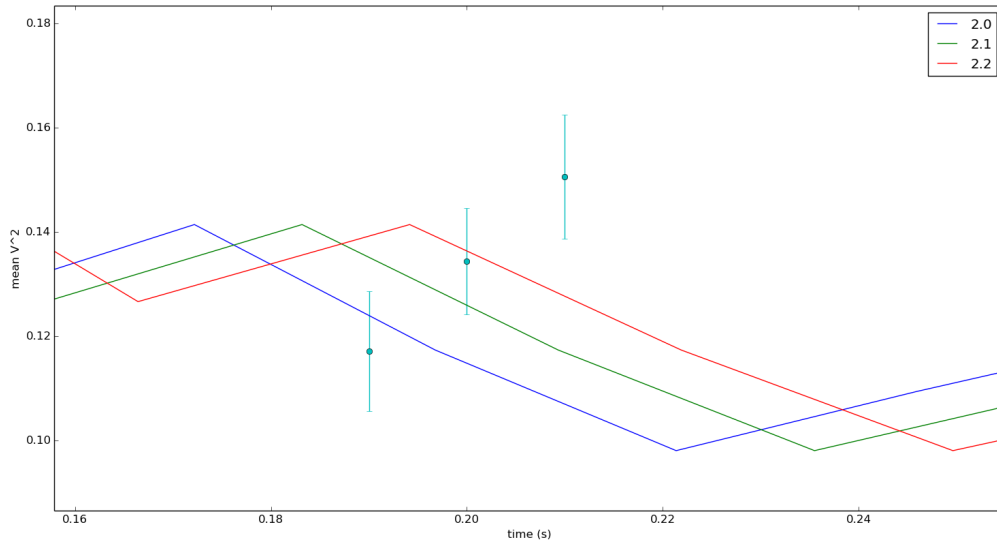


Figure 59: Comparison of observed loss in visibility amplitude for 200 millisecond integration time with UT1-UT3 combination of VLT1 with the simulated loss of visibility amplitude for a 100 meter baseline

4.12 PHASE DELAY SENSITIVITY

Although the SNR_c is not a reliable tool for long integration times ($T_{\text{int}} > 1.78\tau_0$), the required integration time to perform phase delay tracking is shorter than the atmospheric coherence time (τ_0). Hence, the SNR_c is useful to understand the sensitivity in performing phase delay tracking in K and L bands.

To perform closed loop phase delay tracking, we need to achieve a $\text{SNR}_c \geq 4$. Figures 60 & 61 shows the values of SNR_c at different stellar magnitudes in the K and L bands.

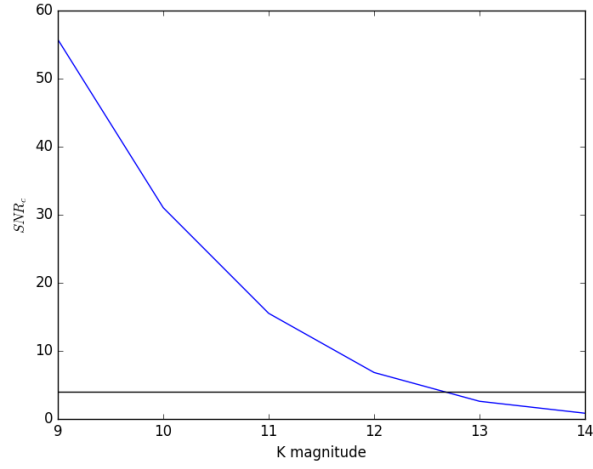


Figure 60: SNR_c vs K band magnitude for an integration time of 100ms for Gravity fringe tracker setup. The black horizontal line marks the threshold of $SNR_c = 4$.

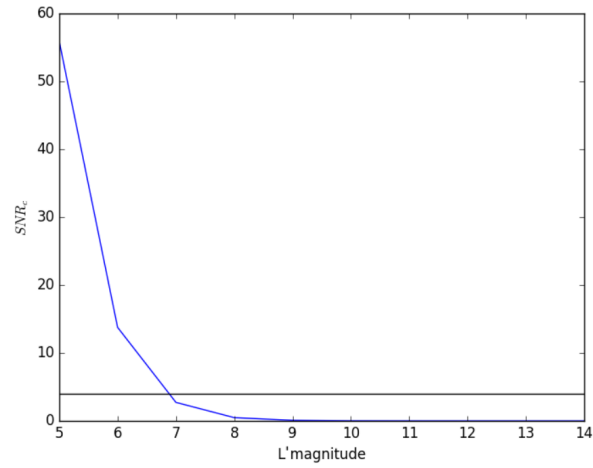


Figure 61: SNR_c vs L band magnitude for an integration time of 100ms for MATISSE L band low spectral resolution ($R=30$) setup. The black horizontal line marks the threshold of $SNR_c = 4$.

Hence the sensitivity to perform phase delay tracking in the K band ≈ 12.5 and ≈ 6.9 in the L band. These are the stellar magnitudes which provides a $SNR_c = 4$.

GROUP DELAY TRACKING

There are different techniques to estimate the group delay from stellar fringes. They are,

- ABCD on dispersed fringes (Colavita et al., 1999) (Sahlmann et al., 2009)
- Least Square fitting (Bonino et al., 2004)
- Double Fourier (Pedretti et al., 2004) (Pedretti et al., 2005)
- Sliding Window (Wilson et al., 2005)
- Sliding Template (Thureau et al., 2003)

In my work, I have mainly concentrated on the first three techniques as they are extensively used at Palomar Testbed Interferometer (PTI) & VLTI. Namely, ABCD on the dispersed fringes, Least Square fitting & Double Fourier techniques.

5.1 ABCD ON DISPERSED FRINGES

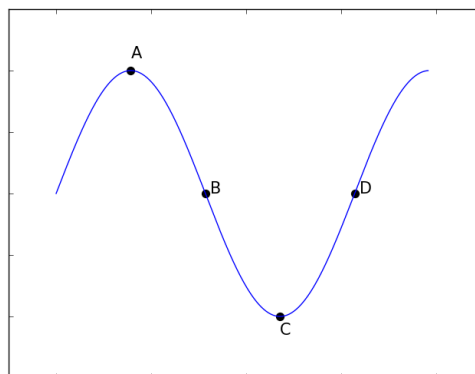


Figure 62: *Description of the ABCD fringe encoding*

To simultaneously estimate the visibility amplitude and phase of the recorded fringes, we need to estimate fringe intensities at 4 positions (A,B,C,D) simultaneously. The ABCD method was first proposed by Shao & Staelin (1977). The four positions are separated by a phase difference of $\pi/2$ from the neighboring points. From the ABCD measurements, we can estimate the fringe visibility amplitude and phase by,

$$V = \frac{\sqrt{(I_A - I_C)^2 + (I_B - I_D)^2}}{I_{\text{tot}}} \quad (115)$$

$$\phi = \tan^{-1} \left(\frac{I_A - I_C}{I_B - I_D} \right) \quad (116)$$

Where, I_{tot} is the total intensity given by, $I_{\text{tot}} = I_A + I_B + I_C + I_D$. Alternatively we can combine the ABCD intensities into the fringe quadrature defined as,

$$Q = X + iY \quad (117)$$

Where,

$$X = I_A - I_C \quad (118)$$

$$Y = I_B - I_D \quad (119)$$

The visibility amplitude is thus the absolute value of the fringe quadrature and the visibility phase is the argument of the complex fringe quadrature.

PRIMA FSU at VLTI ([Sahlmann et al., 2009](#)) and PTI ([Colavita et al., 1999](#)) uses the ABCD measurements on the dispersed fringes to estimate the group delay. The group delay is estimated by performing a Discrete Fourier Transform (DFT) over different spectral channels (λ_i) and scanning with range of OPD through,

$$F(x, t) = \sum_{i=0}^R Q(\lambda_i, t) \exp(-2\pi j k_i x) \quad (120)$$

Where R is the total number of spectral channels and $k_i = 1/\lambda_i$. The value of x at the peak of $|F(x, t)|$ is the group delay position. Figure 63 shows the absolute value of the DFT in the K band with a group delay of $-8\mu\text{m}$ for a 5th magnitude star.

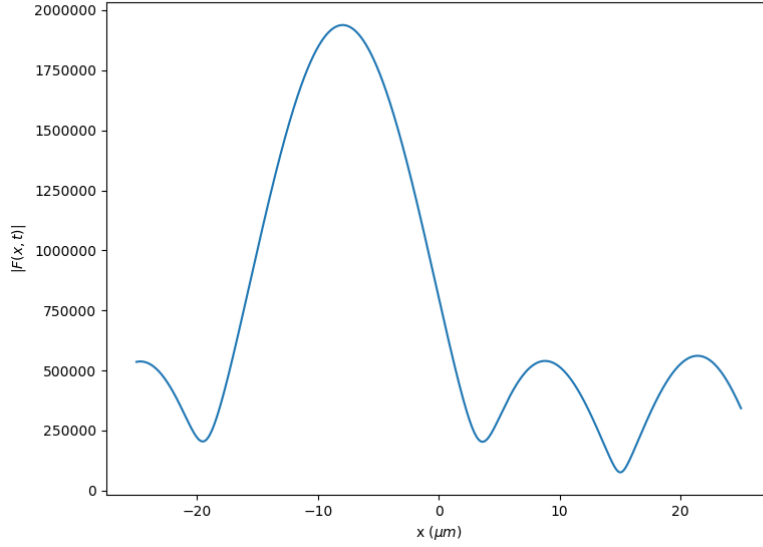


Figure 63: absolute value of the DFT described in eq. 120 for a 5th magnitude star in the K band with a group delay of $-8\mu\text{m}$

5.1.1 Dynamic range

One of the key factors to consider while performing the group delay estimation through dispersed ABCD data is the range of OPD scan during the DFT (also known as dynamic range). The dynamic range should be sufficiently large enough so that the peak of the DFT amplitudes (group delay position) stays within the range. If the scan range is smaller than the dynamic range, the DFT amplitude cycles off to the opposite polarity thus making the group delay measurements in the wrong direction. [Blind et al. \(2011\)](#) estimated that for a K band group delay tracker using ABCD encoding, the fringes have to be dispersed to a minimum of 5 spectral channels over the band to be able to achieve better results.

Rewriting eq. 104 as,

$$I_{\text{BB}} = \int_{\lambda_i}^{\lambda_f} I \exp(2\pi i x_{\text{gd}}/\lambda) \exp(-2\pi i x/\lambda) d\lambda \quad (121)$$

If we assume that $\Delta\lambda$ is the bandwidth and λ_c is its central wavelength, the width of the broadband fringe envelope (coherence length) will be,

$$L_c = \frac{\lambda_c^2}{\Delta\lambda} \quad (122)$$

we disperse the fringes over N_λ spectral channels of equal width given by,

$$\delta\sigma = \Delta\sigma/N_\lambda \quad (123)$$

Where, σ is the wave number and $\Delta\sigma$ is the bandwidth which is related to the wavelength by $\Delta\sigma = 1/L_c$. The DFT of eq. 121 using eq. 120 is,

$$F(x) = \sum_{k=1}^{N_\lambda} I \exp(-2\pi i \sigma_k (x - x_{gd})) \quad (124)$$

The squared amplitude of the DFT can be written as,

$$|F(x)|^2 = F(x)F^*(x) = I^2 \sum_{k=1}^{N_\lambda} \sum_{l=1}^{N_\lambda} \exp(-2\pi i (\sigma_k - \sigma_l)(x - x_{gd})) \quad (125)$$

As each spectral channel has equal width,

$$\sigma_k - \sigma_l = \delta\sigma(k - l) \quad (126)$$

Hence, eq. 125 can be rewritten as,

$$|F(x)|^2 = I^2 \sum_{k=1}^{N_\lambda} \sum_{l=1}^{N_\lambda} \exp(-2\pi i \delta\sigma(k - l)(x - x_{gd})) \quad (127)$$

The peak of the squared DFT amplitude occurs at the position $x = x_{gd}$ with an ambiguity of $1/\delta\sigma$. This ambiguity depends on the number of channels and hence the dynamic range as,

$$DR = N_\lambda \frac{\lambda_c^2}{\Delta\lambda} \quad (128)$$

To perform K band group delay tracking using the dispersed ABCD encoding of fringes, the excursion of OPD over the integration time is $-20\mu\text{m} - 20\mu\text{m}$. Thus the ideal number of spectral channels in the K band which corresponds to this dynamic range is 5.

Figure 64 shows the simulated input group delay time-series and the measured group delay using noisy K band fringes of a 10th magnitude source dispersed over 5 spectral channels at an integration time of 100ms. Fig. 65 shows the simulated input group delay time-series and the measured group delay time series measured with a noisy L' band fringes of a 7th magnitude source with an integration time of 100ms.

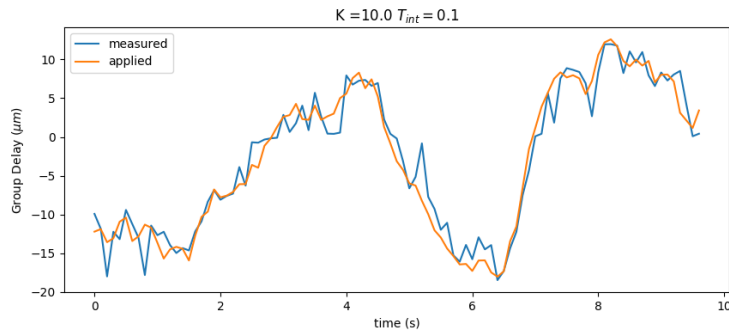


Figure 64: K band simulated and measured group delay time series using ABCD algorithm on dispersed fringes in the K band for an unresolved source with 10th magnitude and an integration time of 100ms

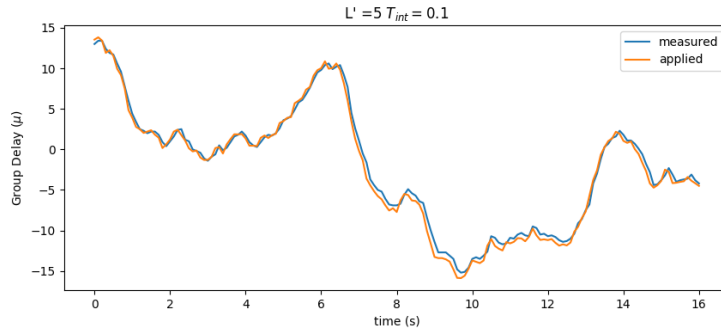


Figure 65: L' band simulated and measured group delay time series using ABCD algorithm on dispersed fringes in the L band for an unresolved source with 7th magnitude and an integration time of 100ms

Figures 66 & 67 shows the comparison of input simulated group delay and the measured group delay with ABCD encoding. The diagonal black line shows the ideal case where the input group delay is equal to the measured group delay.

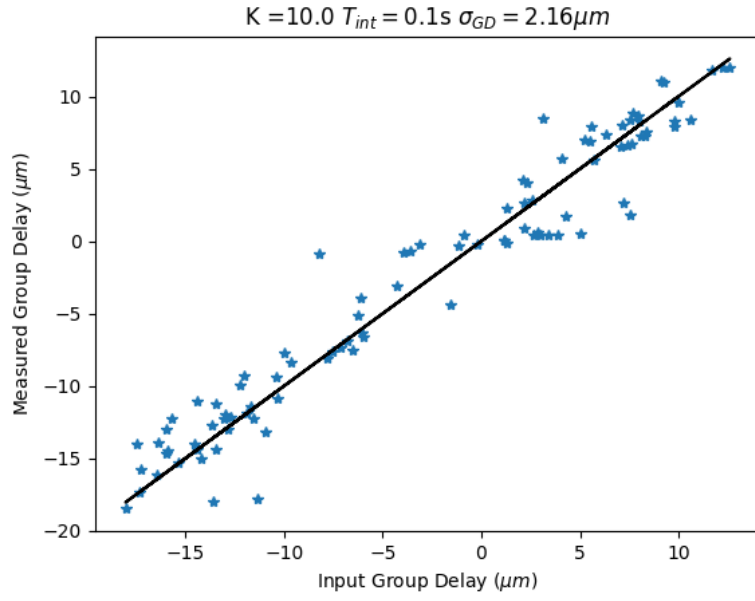


Figure 66: Comparison of the input and measured K band group delay of the time series shown in fig. 64

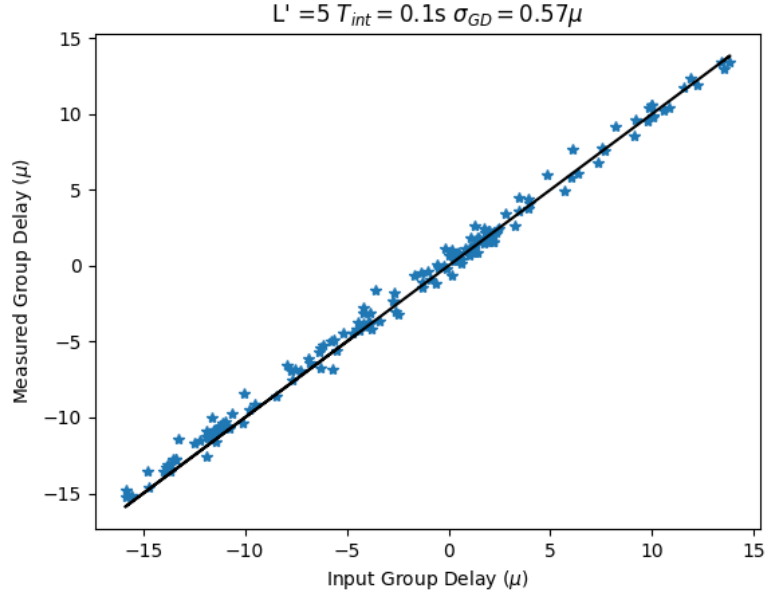


Figure 67: Comparison of the input and measured L' band group delay shown in fig. 65

5.2 LEAST SQUARE ESTIMATION

The least square estimation technique fits the noisy broadband fringes data to a standard fringe model. This technique is used in FINITO (Gai et al., 2004) and CHAMP fringe tracker. The technique was first proposed by Bonino et al. (2004) where the observed fringe signal ($O(z)$) is fitted by a fringe model ($M(x)$) by estimating the square discrepancy function given by,

$$e = \frac{(O(z) - M(x))^2}{\sigma^2} \quad (129)$$

The efficiency of the group delay estimation with the least square technique depends on the chosen envelope model. Blind et al. (2011) compared the efficiency of using a parabola model and a sinc model for the central fringe envelope. They concluded that the sinc function has a better performance than the parabola model in estimating the group delay. Hence, we adopted the model of Wilson et al. (2005) of a cosine function amplitude modulated by a sinc function. Using the equation 111, we can define a simple model for the broadband fringes as,

$$M(x) = A \text{sinc}(Bx + C) \cos(Dx + E) \quad (130)$$

Where,

- $A \rightarrow$ Fringe amplitude
- $B \rightarrow$ Coherence length ($L_c = \lambda_c^2 / \Delta\lambda$)
- $C \rightarrow$ White light fringe position
- $D \rightarrow$ fringe frequency ($1/\lambda_c$)
- $E \rightarrow$ dispersion parameter ($\sum_{wv} \frac{dR}{d\lambda}$)

To have the best fitting model, we need to fit the model with the minimum value of square discrepancy function given in eq. 129. We can rewrite equation 82 as a function of model parameters C and E as,

$$x_g = NL + Lk \frac{dN}{dk} = C + E \quad (131)$$

We can estimate C by finding the maximum intensity position of the recorded fringe and then fit the model with the observed fringes by modulating E and finding the absolute minimum using Newton-Raphson method. Fig. 68

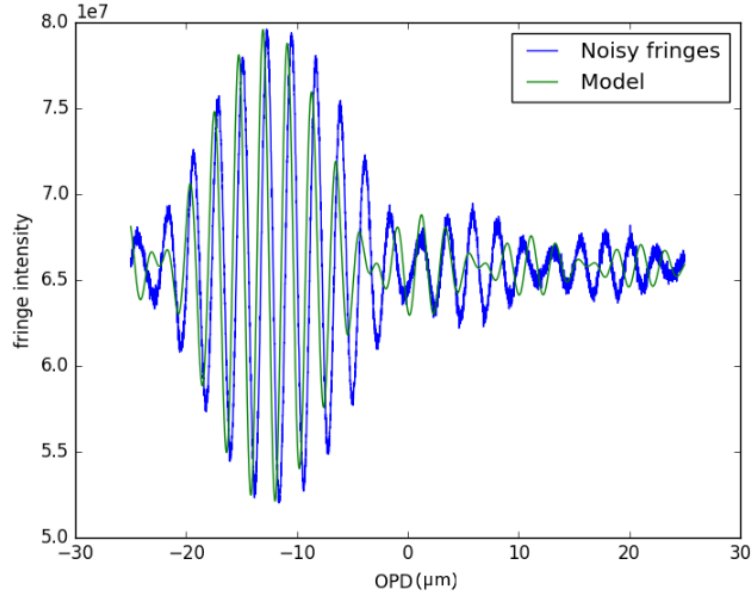


Figure 68: Sample K band simulated noisy broad band fringe of an unresolved source at 10th magnitude with a delay of $-11\mu\text{m}$ fitted with the model

Fig. 69 & 70 shows the simulated group delay time series and the measured group delay for K and L' bands.

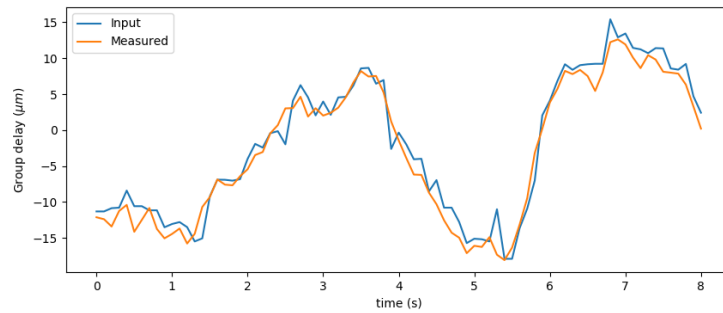


Figure 69: Simulated input and measured group delay in K band using noisy fringes of a 10th magnitude unresolved source with 100ms integration using the least squares technique

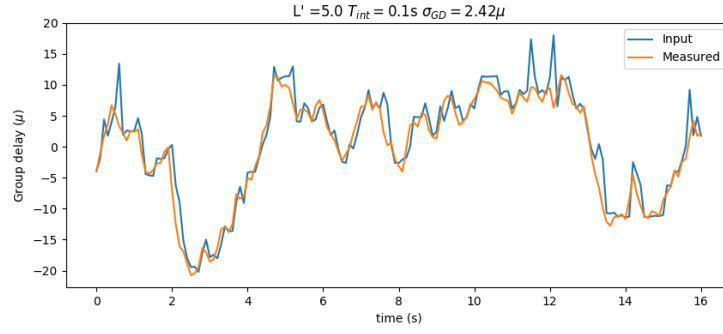


Figure 70: Simulated input and measured group delay in L' band using noisy fringes of a 5th magnitude unresolved source with 100ms integration using the least squares technique

Fig. 71 & 72 shows the direct comparison of the input group delay and the measured group delay of the time series shown in fig. 69 & 70 in K and L' bands respectively.

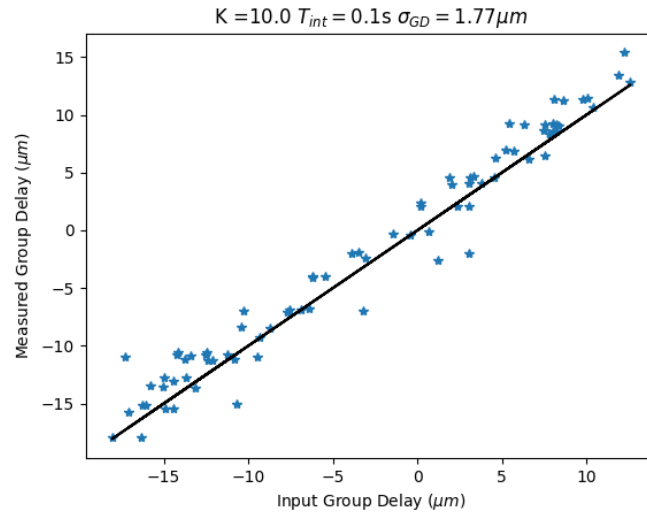


Figure 71: Comparison of K band input and measured group delay from the time series shown in fig. 69

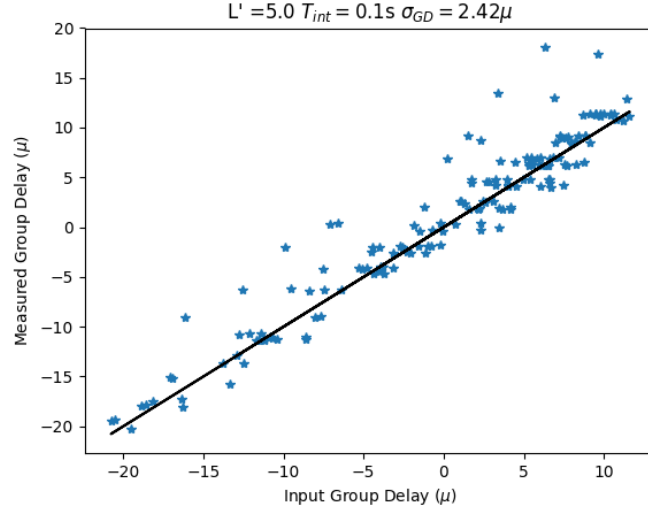


Figure 72: Comparison of L' band input and measured group delay from the time series shown in fig. 70

5.3 DOUBLE CORRELATION

The double correlation technique is used in the Infrared Optical Telescope Array (IOTA) fringe tracker (Pedretti et al., 2004). This technique involves in deriving the group delay (x_{gd}) from the auto-correlation of the broadband fringes. Using eq. 111, we can define the broadband fringes as,

$$I_{BB}(x) = I_0 \frac{\sin(\pi(x - x_{gd})\Delta m)}{\pi(x - x_{gd})\Delta m} \sin\left(\frac{2\pi(x - x_{gd})M_0}{N}\right) \quad (132)$$

Where,

- $I_0 \rightarrow$ fringe peak intensity
- $x_{gd} \rightarrow$ group delay
- $\Delta m \rightarrow$ Spatial frequency associated with the bandwidth
- $M_0 \rightarrow$ Central frequency
- $N \rightarrow$ number of samples

The fast Fourier transform of the broadband fringes described above is,

$$\hat{I}(m) = \sum_{i=1}^N I_{BB}(x) e^{-2\pi j m \frac{i}{N}} \quad (133)$$

The auto-correlation of the fringes between spatial frequencies m_1 & m_2 with a width of Δm_{12} can be written as,

$$\begin{aligned} X(m_1, m_2) &= \hat{I}(m_1) \hat{I}^*(m_2) = \left(\frac{i}{2} \exp \left(i \frac{2\pi m_1 x_{gd}}{N} \right) \right) \left(\frac{i}{2} \exp \left(i \frac{2\pi m_2 x_{gd}}{N} \right) \right)^* \\ &= \frac{1}{4} \exp(-i2\pi x_{gd}(m_1 - m_2)) \quad (134) \end{aligned}$$

We can now calculate the auto-correlation for all frequencies with a width of Δm_{12} to derive the cross spectral value with a high SNR by,

$$X(\Delta m_{12}) = \sum_{m_1} \frac{1}{4} \exp(-i2\pi x_{gd}(m_1 - m_2)) \quad (135)$$

Thus the group delay can be derived from $X(\Delta m_{12})$ as,

$$x_{gd} = \frac{N \arg(X)}{2\pi \Delta m_{12}} \quad (136)$$

The two free parameters in this technique is the number of samples (N) and the difference in the spatial frequencies (Δm_{12}). We can restrict $\Delta m_{12} = 1$ and increase the performance by adding more number of samples. The noise on the group delay measurement will then depend on \sqrt{N} .

Fig. 73 & 74 shows the input and the measured group delay time series for an unresolved source in K band with 10th magnitude and L' band with 5th magnitude with an integration time of 100ms.

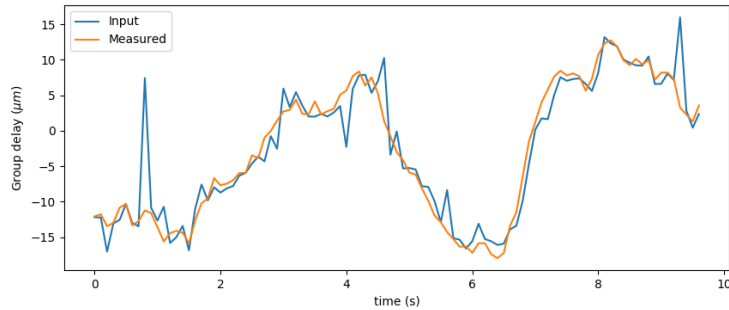


Figure 73: Input and measured group delay time series with synthetic noisy fringes of an unresolved K band source at 10th magnitude

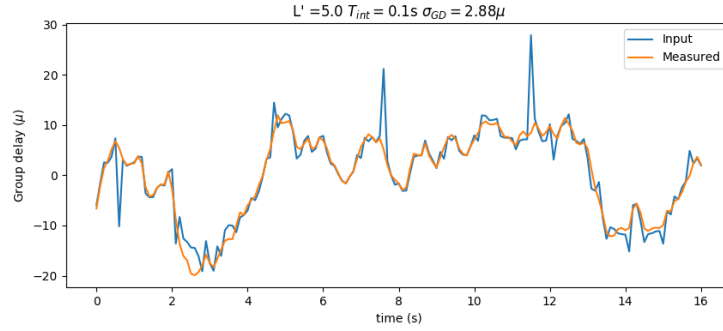


Figure 74: *Input and measured group delay time series with synthetic noisy fringes of an unresolved L' band source at 5th magnitude*

Fig. 75 & 76 shows the direct comparison of the input and measured group delay from fig. 73 & 74.

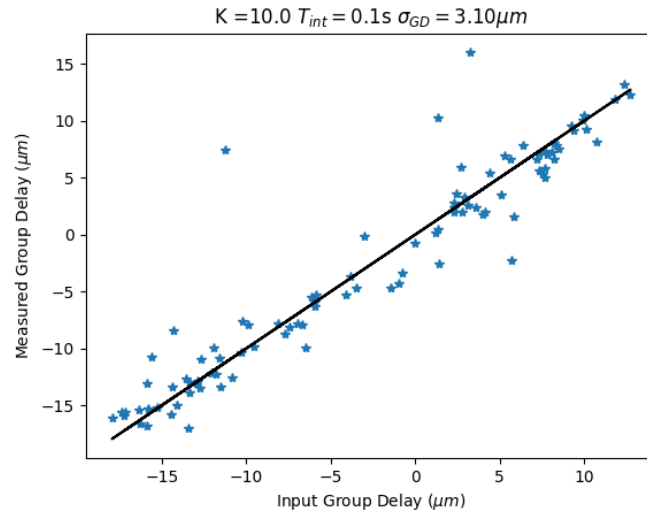


Figure 75: *Comparison of the input and the measured group delay in K band shown in fig. 73. The black diagonal line shows the ideal case where input group delay = measured group delay*

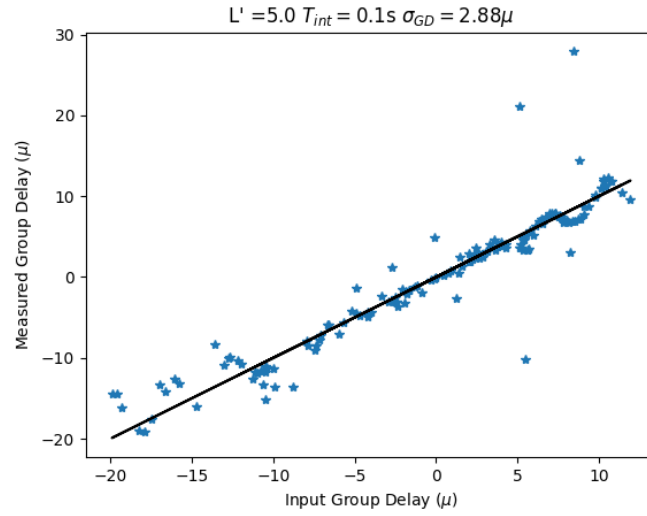


Figure 76: Comparison of the input and the measured group delay in L' band shown in fig. 76. The black diagonal line shows the ideal case where input group delay = measured group delay

5.4 OTHER TECHNIQUES

The sliding window and the sliding template techniques proposed by [Wilson et al. \(2005\)](#) and [Thureau et al. \(2003\)](#) are viable and sophisticated algorithms in measuring the group delay from noisy broadband fringes. However, [Pedretti et al. \(2004\)](#) found very little difference in their performance in comparison with the double Fourier technique. The least squares fitting and the DFT with ABCD encoding techniques are the most widely used techniques. Hence, I have concentrated mainly on the least squares, DFT with ABCD encoding and double Fourier techniques.

5.4.1 Sliding Window

The sliding window technique is used at the IOTA interferometer for coherencing ([Wilson et al., 2005](#)). This technique involves in estimating the DFT amplitudes by sliding a rectangular window of width equal to the fringe frequency. The position of the peak of the DFT amplitudes corresponds to the group delay position. However, in reality 5 different frequencies around the fringe frequency are chosen and the window width of the next scan is derived from maximum DFT amplitudes over the 5 frequencies.

5.4.2 *Sliding Template*

The sliding template technique is used at the COAST interferometer (Thureau et al., 2003). This technique involves in two orthogonal models of the broadband fringes (similar to eq. 130), where one is a cosine function modulated by a sinc function and the other one is a sine function modulated by a sinc function. Both the templates corresponds to the real and the imaginary parts of the fringe phasors. These two templates can be correlated with the observed fringe data through convolution, i.e., the template and the data are multiplied in the Fourier space and the inverse Fourier transform corresponds to the correlation function. The resulting correlation function will be a series of envelopes which can be averaged over time and the group delay position corresponds to the centroid position of this correlation function.

RESULTS AND DISCUSSION

6.1 RESIDUAL GROUP DELAY

As described in § 4.3, the value SNR_c is reliable in estimating the sensitivity only in the Maréchal regime ($t_{\text{int}} \leq 1.78\tau_0$). However, at longer time scales ($t_{\text{int}} > 1.78\tau_0$) the random walk behavior (as described in § 3.9.1) starts to dominate and SNR_c is not a reliable tool to estimate the sensitivity of the fringe tracker. However, the residual group delay from the 3 techniques described in chapter 5 is a viable alternative in estimating the sensitivity of a group delay tracker.

The residual group delay ((input/simulated group delay)-(measured group delay)) for different stellar magnitudes at K & L bands are computed by identifying the difference between the applied and the measured group delay. Fig. 77 shows the sample group delay residuals in the K band for a 100ms integration time for a 10th magnitude unresolved source.

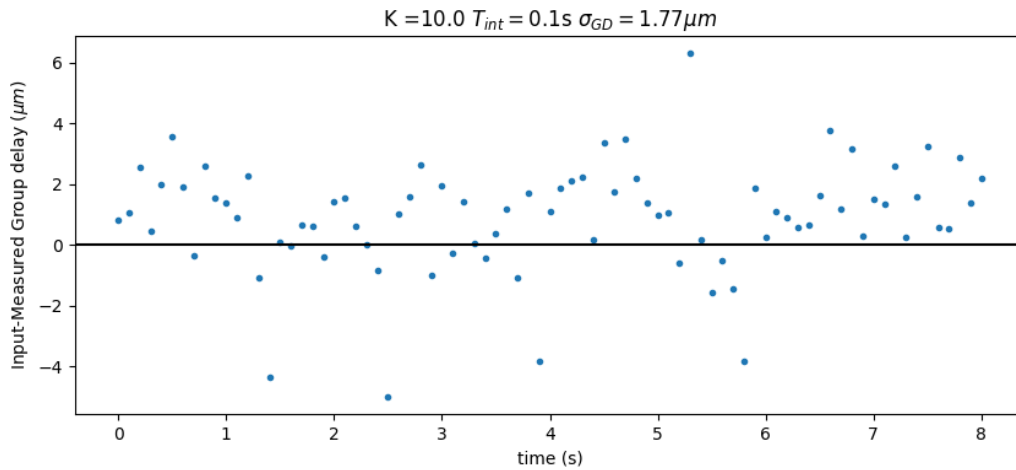


Figure 77: Sample residual group delay estimated with the least square algorithm with a K band unresolved source of 10th magnitude at an integration time of 100ms

6.2 RMS ON THE RESIDUAL GROUP DELAY

The RMS on the residual group delay is then estimated over different stellar magnitudes and integration times to estimate the sensitivity and performance of different group delay tracking algorithms. However, due to the random seed for each run of GDsim

and the random noises on the simulated fringe signal (as described in § 4.1) the RMS on the residual group delay for each iteration is limited by the random nature. Fig. 78 shows the RMS of the residual group delay for one random iteration of the GDsim run.

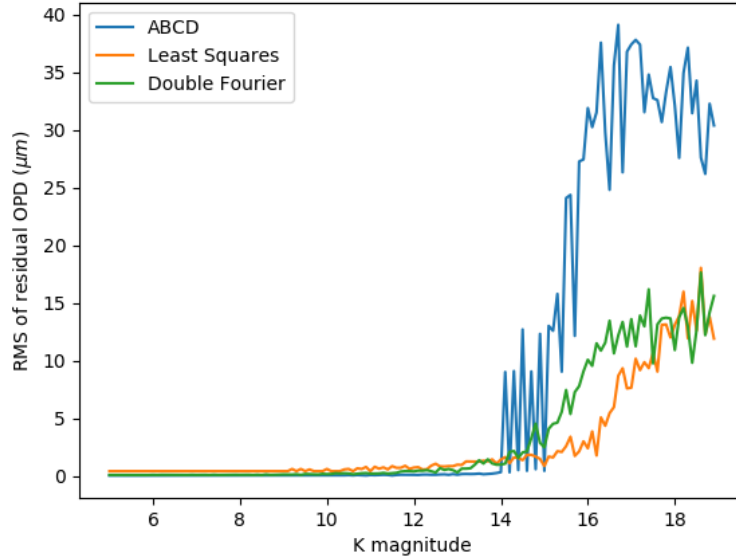


Figure 78: *RMS of the residual group delay in the K band for a Gravity fringe tracker with 100ms integration time set up for one random realization of the atmospheric turbulence*

To remove the random nature of each simulated group delay time series, the RMS of the residual group delay is estimated for multiple realizations of the atmospheric turbulence and the final RMS of the residual group delay is computed by averaging over all the different realizations. In my simulations, the RMS on the residual OPD is averaged over 20 independent iterations of the atmospheric turbulence and the noises on the interferometric signal.

Fig. 79 & 80 shows the RMS on the residual group delay in the K and L' bands respectively for different stellar magnitudes at 100ms integration time.

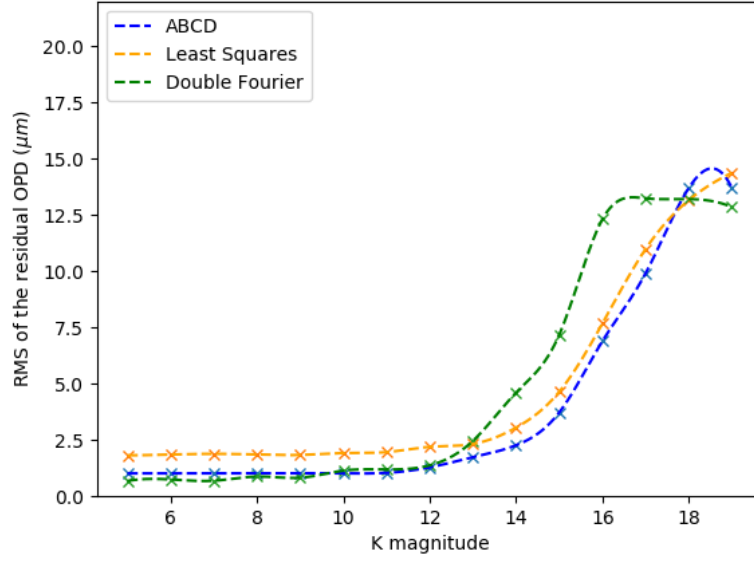


Figure 79: *RMS on the residual group delay in the K band with Gravity fringe tracker setup for different stellar magnitudes at 100ms integration time*

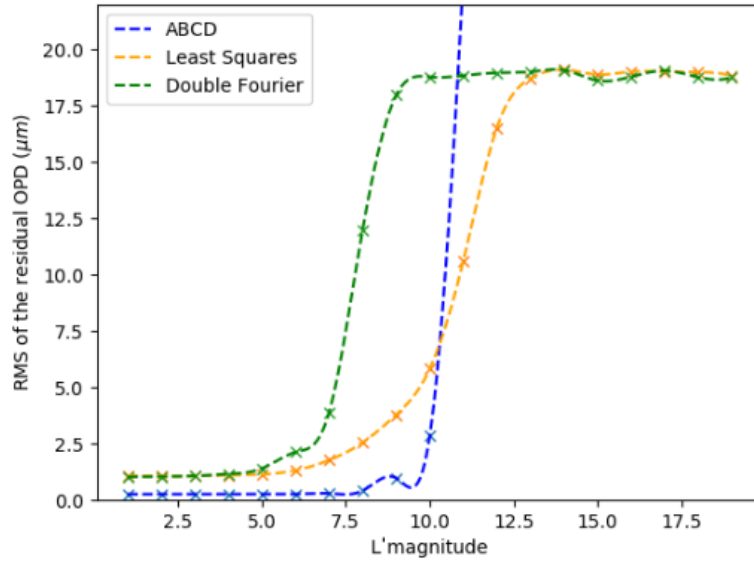


Figure 80: *RMS on the residual group delay in the L' band with Matisse L band setup for different stellar magnitudes at 100ms integration time*

6.3 IDEAL INTEGRATION TIME

To perform phase delay tracking, the independent phases should be sampled at a time scale shorter than the atmospheric coherence time (τ_0). However, we can perform group delay estimation at longer time scales. This is due to the fluctuation timescale of water vapor in the atmosphere is longer than that of the dry air (Lay, 1997).

The accuracy of group delay estimation depends on the position of the peak and the shape of the fringe envelope. If the frequency bandpass of the spectral band is related to the central frequency by,

$$\Delta\nu = \nu_c/\alpha \quad (137)$$

Where, α is a dimensionless constant. We can assume that the fringe envelope signal is lost when the envelope moves by its own width during the integration. For the envelope to move by its own width it has to move by $\alpha \times \lambda$ ($2\pi\alpha$ radians). This time scale is related to the dry air atmospheric coherence time by (Buscher, 1988),

$$T = (2\pi\alpha)^{6/5}\tau_0 \quad (138)$$

This integration time is the maximum possible integration time for a group delay tracker. For a K band group delay tracker with an average Fried parameter of 60cms and wind velocity of 10m/s, the dry air atmospheric coherence time from eq. 53 is,

$$\tau_0^K = 0.207 \left(\frac{0.6}{10} \right) = 12.4\text{ms} \quad (139)$$

In the case of L' band with an average Fried parameter of 1.0 meter and wind velocity of 10m/s, the dry air atmospheric coherence time is,

$$\tau_0^{L'} = 0.207 \left(\frac{1}{10} \right) = 20.7\text{ms} \quad (140)$$

The K band spans between $2.0\mu\text{m} - 2.4\mu\text{m}$ and a bandpass of $3.09 \times 10^{13}\text{Hz}$, thus resulting in the value of $\alpha_K = 4.4$. In the case of L' band ($3.5\mu\text{m} - 4.0\mu\text{m}$), a bandpass of $1.09 \times 10^{13}\text{Hz}$ results in $\alpha_{L'} = 7.4$. Thus the maximum K and L band integration time for group delay estimation is given in eq. 141 & 142 respectively.

$$T_{\text{int}}^{\text{GD},K} = (2\pi\alpha_K)^{6/5}\tau_0^K = 53.69\tau_0^K = 0.7\text{seconds} \quad (141)$$

$$T_{\text{int}}^{\text{GD},L'} = (2\pi\alpha_{L'})^{6/5}\tau_0^{L'} = 102.935\tau_0^{L'} = 2.1\text{seconds} \quad (142)$$

Fig. 81 & 82 shows the comparison on the RMS on the residual group delay for 100ms and the T_{int} for K and L' bands respectively.

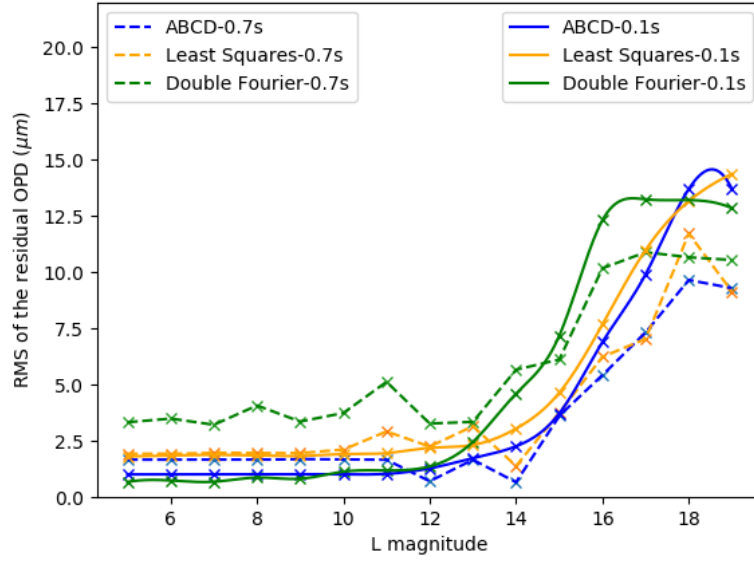


Figure 81: Comparison of RMS on the residual group delay for 100ms and 700ms integration time with different group delay estimation techniques in the K band

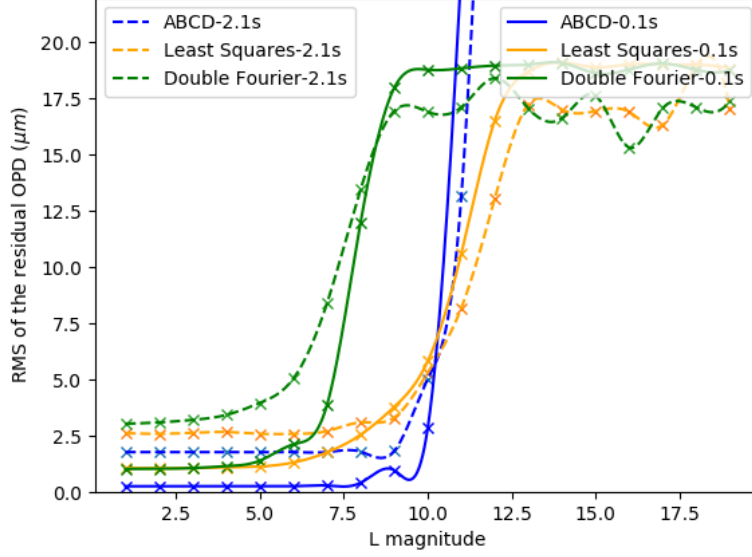


Figure 82: Comparison of RMS on the residual group delay for 100ms and 2.1 seconds integration time with different group delay estimation techniques in the L' band

From fig. 81 & 82 we can conclude that the longer integration reduces the residual difference between the input and the measured group delay for faint targets (high SNR). However for brighter targets, short integration time is more beneficial.

6.4 PERFORMANCE AND SENSITIVITY

The main advantage in estimating the RMS on the residual group delay is that it serves the dual purpose of estimating the performance and sensitivity of each group delay estimation technique. We can split RMS on the residual group delay plots into three regimes. They are,

- High SNR regime, where the RMS of the residual group delay depends only on the limitations of the technique.
- Intermediate SNR regime, where the noise on the fringes plays a significant role in the residual group delay.
- Low SNR regime, where the noise completely dominates and the fringe signal is completely lost.

The limitations of the techniques include,

- Dynamic range and OPD scan step during the DFT of the dispersed ABCD fringes.

- Sensitivity of the fringe envelope model which is fitted by the least squares technique. [Blind et al. \(2011\)](#) found that the sinc function is a better model when compared to a simple parabola model.
- Insufficient number of samples around the fringe envelope or under-sampling the fringes with the double Fourier technique.

Hence, the RMS on the residual group delay is a better alternative to estimate the sensitivity and performance of the group delay estimation techniques than looking only at the SNR.

6.5 INCOHERENT STACKING

Another way to overcome the phase fluctuations during a long integration is to stack each independent fringe frames by their power spectrum. As the power spectrum is insensitive to the phase of the input signal, the fringes can be stacked by their power spectrum to achieve high SNR. If we integrate the fringe frames by their power spectra for a time scale which is half the integration time shown in eq. 138, the resulting signal will have a SNR gain by a factor of 6 as compared to coherent addition of fringes ([Buscher, 1988](#)).

Incoherent addition of fringe frames also removes the errors on coupling the incoming stellar light to optical fibers. If the OPD scan is performed faster than the bandwidth of the fibre coupling fluctuations, the lower frequency scintillation noise can be removed with a high pass filter in the Fourier space.

We can estimate the visibility amplitude from the resulting power spectrum by ([Millour et al., 2016](#)),

$$V^2(\lambda) = \frac{\sum_u \langle |\hat{I}(u, \lambda, t)|^2 \rangle_t}{2 \sum_x \langle P_a(x, \lambda, t) P_b(x, \lambda, t) \rangle_t} \quad (143)$$

Where,

- $\hat{I} \rightarrow$ Fourier transform of the fringe intensities
- $u \rightarrow$ Spatial frequency
- $x \rightarrow$ OPD
- $P_a, P_b \rightarrow$ Photometric contribution from telescopes a and b into the interferometric channel

If the SNR on each fringe frame is sufficiently high, we can also estimate the closure phases from the complex Fourier transform of the fringe frames. The closure phase can be computed by performing a triple correlation of the fringe Fourier spectra of the three baselines.

$$O_{ij}^3(\lambda) = \langle \hat{I}(u, \lambda, t) \hat{I}(v, \lambda, t) \hat{I}^*(u + v, \lambda, t) \rangle_t \quad (144)$$

Even though incoherent addition of fringe frames is insensitive to phase fluctuations, a proper estimation of the fringe power spectrum requires the fringes to be within the coherence length. Hence, coherencing and stacking independent fringe power spectra will increase the sensitivity of an interferometer.

Assuming a top-hat shaped bandpass at each spectral channel with a bandwidth of Δk in wave number, the loss in the resulting visibility amplitude due to an OPD fluctuation RMS of x is given by,

$$V = \text{sinc}(\pi x \Delta k) \quad (145)$$

We can estimate the sensitivity of a group delay algorithm by setting an upper limit on the maximum possible delay (x) for a given budget on the visibility amplitude loss. For example, a 10% loss in contrast can be calibrated by a separate calibration star observation. Thus, we can assume a 10% loss as the maximum budget for the science channel visibilities. Hence, for science observation in the L band with Matisse at low spectral resolution ($R=30$), the bandwidth for each spectral channel will be $0.019\mu\text{m}^{-1}$. Thus for $V = 0.9$, the value of x should be $13\mu\text{m}$. This is the upper limit threshold on the RMS of the residual group delay that will result in a loss in fringe contrast in the science channel to be $\leq 10\%$.

However, the threshold value of x mentioned above is the error on the corrected group delay position. For an efficient closed-loop group delay tracker the error on the measured group delay should be 4 times smaller than the error on the corrected group delay. Thus the threshold limit on the RMS of the residual group delay will be $13/4 = 3.25\mu\text{m}$.

Figures 83 & 84 shows the same plots as in figures 79 & 80 with the $3.25\mu\text{m}$ threshold. The resulting group delay sensitivities are tabulated in table 8.

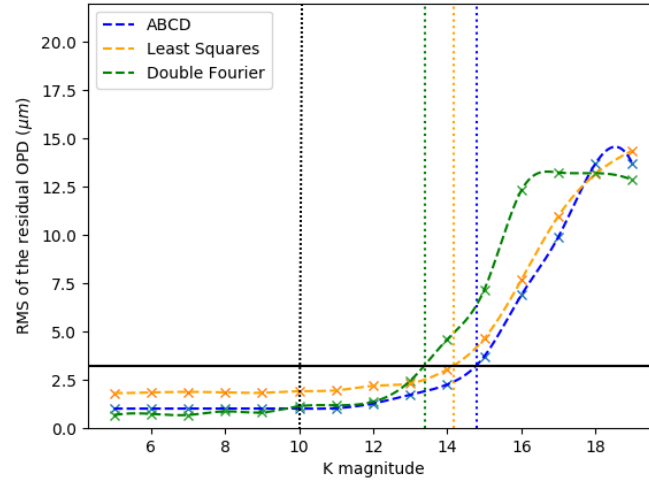


Figure 83: RMS on the residual group delay in K band for a Gravity fringe tracker set up for 100ms integration time for different stellar magnitudes. The horizontal black line shows the $3.25\mu\text{m}$ threshold for MATISSE L band science at low spectral resolution ($R=30$). The vertical black dotted line shows the 10th magnitude phase delay tracking limit of Gravity Fringe tracker in the K band.

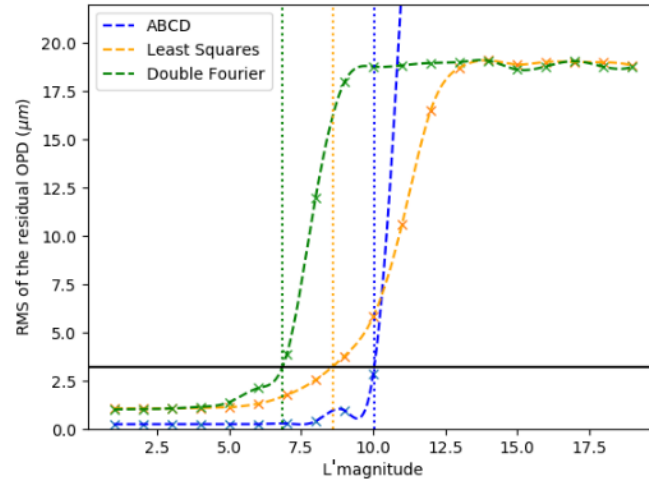


Figure 84: RMS on the residual group delay in the L' band for MATISSE L band set up for 100ms integration time for different stellar magnitudes. The horizontal black line shows the $3.25\mu\text{m}$ threshold for MATISSE L band science at low spectral resolution ($R=30$)

| Technique | K | L |
|----------------|-------|-------|
| ABCD | 14.67 | 10.02 |
| Least square | 14.12 | 8.56 |
| Double Fourier | 13.36 | 6.64 |

Table 8: *K and L band sensitivity in estimating group delay for coherencing science fringes in the L band with MATISSE at low spectral resolution*

At higher spectral resolution the value of Δk gets smaller, thus the threshold value of x becomes larger. Thus for medium spectral resolution ($R = 500$) and high spectral resolution ($R = 950$) of MATISSE L band science the threshold on the error on measured group delay is $53.75\mu\text{m}$ and $100\mu\text{m}$ respectively. However, such threshold values are larger than the asymptotic value on the RMS at the noise dominated regime. Thus, we can assume the turning point between the second and third regimes on the RMS of the residual group delay.

6.6 COHERENCING WITH AUXILIARY TELESCOPES

I have also extended the above analysis (which is mainly on the UTs of the VLTI), into the Auxiliary Telescopes (AT) of VLTI. I have simulated the atmospheric turbulence for 80 meters baselines for the ATs.

Due to the lack of vibration parameters of the auxiliary telescopes, I have simulated only the atmospheric turbulence. Figures 85a and 85b shows the RMS on the residual group delay for K and L' bands respectively with the AT of VLTI with the $3.25\mu\text{m}$ threshold for MATISSE L band science at low spectral resolution ($R=30$). The group delay sensitivities are tabulated in table 9

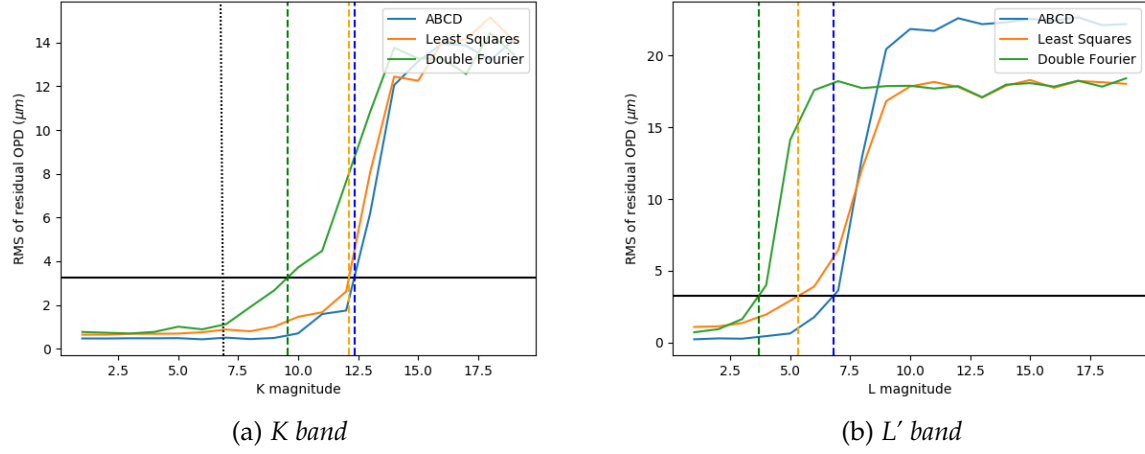


Figure 85: RMS on the residual group delay measured in K and L' bands with a Gravity fringe tracker and MATISSE L band setup at 100ms integration time with the ATs at a baseline of 80 meters. The vertical black dotted line shows the K=7 phase delay sensitivity limit of the Gravity fringe tracker with ATs.

| Technique | K | L |
|----------------|-------|------|
| ABCD | 12.33 | 6.78 |
| Least square | 12.11 | 5.33 |
| Double Fourier | 9.55 | 3.68 |

Table 9: K and L band sensitivity in estimating group delay with ATs for coherencing science fringes in the L band with MATISSE at low spectral resolution

6.7 GROUP DELAY TRACKING WITH RESOLVED SOURCES

One of the main assumptions of my work is that the phase reference source is spatially unresolved (visibility amplitude = 1). However, in some cases when there is a lack of unresolved phase reference in the field of view, on source fringe tracking of the resolved source is the only option. Figure 86 shows the RMS of the residual group delay in the K band by using a resolved phase reference with a visibility amplitude of 0.2 and 0.5. Table 10 shows the corresponding sensitivities.

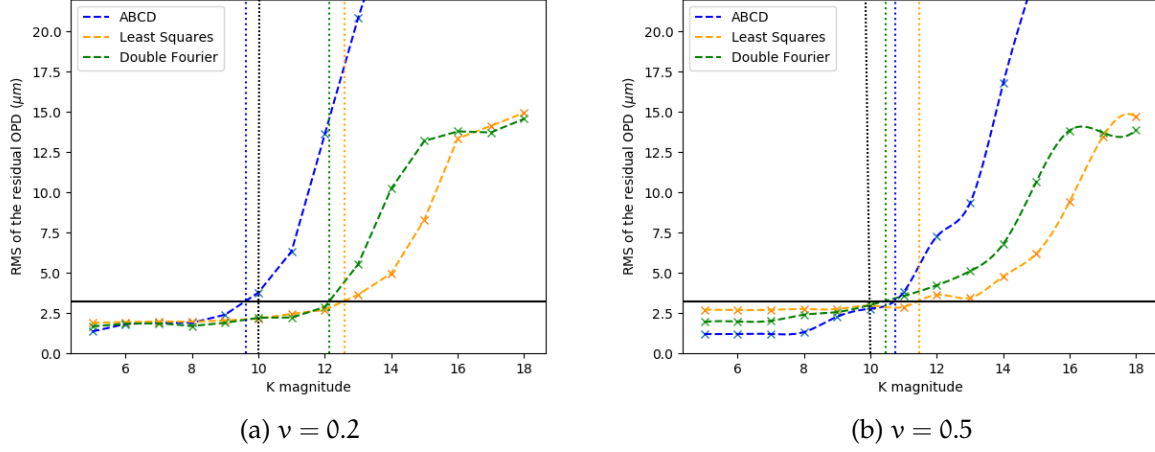


Figure 86: RMS on the residual group delay in the K band with a spatially resolved phase reference. The vertical black dotted line shows the 10th magnitude phase delay sensitivity limit of Gravity fringe tracker with the UTs.

| Technique | $\nu = 0.2$ | $\nu = 0.5$ |
|----------------|-------------|-------------|
| ABCD | 9.62 | 10.74 |
| Least Squares | 12.59 | 11.46 |
| Double Fourier | 12.14 | 10.45 |

Table 10: K band group delay sensitivity by using a spatially resolved phase reference

6.8 DIFFERENT VIBRATION MODES

Mérand et al. (2012) has measured the RMS of the OPD fluctuations caused due to instrumental vibrations for the AMBER instrument at VLTI to be in the range of 300nm – 700nm (as shown in table 1). However, Perrin et al. (2011) reports that currently the vibrations at the VLTI is controlled to have a total RMS on the OPD fluctuations due to instrumental vibrations to under 200nm. Most of the work mentioned above works for the current vibration level. Here let us compare the effects of the high vibration levels mentioned by Mérand et al. (2012) to the main result of this work. Fig. 87 shows the K and L band RMS on the residual OPD with a high vibration level of UT1 & UT2 with a $\sigma_{\text{OPD},\text{vib}} = 411\text{nm}$. Table 11 shows the corresponding sensitivities in K and L bands.

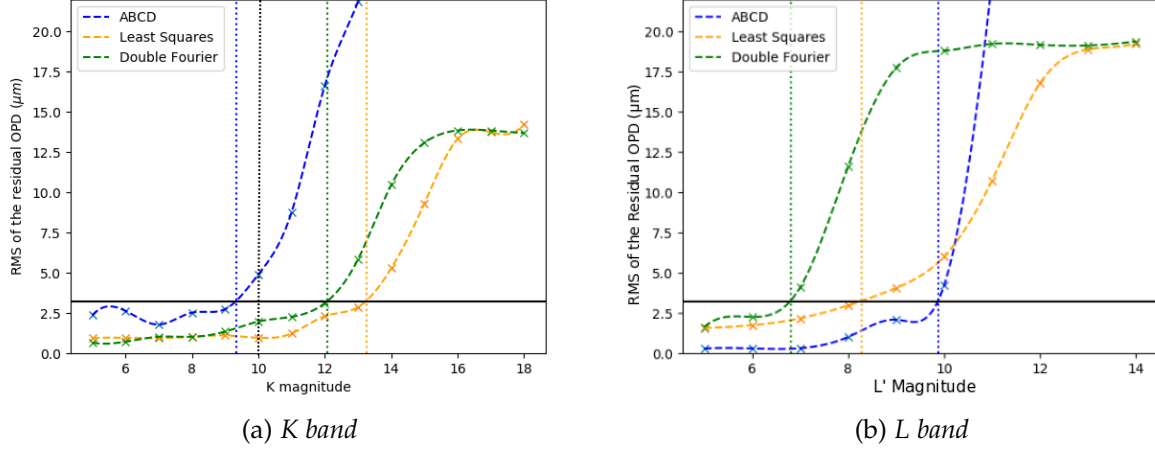


Figure 87: RMS on the residual OPD at K and L bands for high vibration levels with UT₁-UT₂ combination with $\sigma_{\text{OPD,vib}} = 411\text{nm}$. Estimated on a spatially unresolved source ($\nu = 1$). The black vertical dotted line shown in the left figure shows the 10th magnitude phase delay tracking sensitivity of Gravity fringe tracker with UTs!

| Technique | K | L |
|----------------|-------|------|
| ABCD | 9.33 | 9.88 |
| Least square | 13.25 | 8.28 |
| Double Fourier | 12.09 | 6.8 |

Table 11: K and L band sensitivity in estimating group delay for coherencing science fringes at high vibration level (411nm) in the L band with MATISSE at low spectral resolution

From fig. 87 and table 11, we can see that the K band is strongly affected by high vibration levels. However, the effect on the L band is insignificant at high vibration levels. Also comparing figures 87a & 83, we can see that the ABCD technique on dispersed K band fringes is the most affected method (loss of 5.34 magnitudes on sensitivity). This might be due to insufficient step size on the DFT and the loss of correlated flux due to the high loss in fringe contrast ($\sigma_{\text{OPD,vibration}} = 411\text{nm} \approx \lambda_c/5$) as compared to that of the L' band ($\sigma_{\text{OPD,vibration}} \approx \lambda_c/9$).

6.9 MID-IR FEED FORWARD GROUP DELAY

Koresko et al. (2006) used the intra-band dispersion in the K band at the Keck interferometer to estimate the possibility to feed forward to a possible mid infrared nulling

interferometer operating at $10\mu\text{m}$. This involves in computing the dispersion metric mentioned in eq. 88 using the phase and group delay estimates in the K band. Using the dispersion metric, we can estimate the instantaneous differential water vapor column density (Σ_{wv}) and with the knowledge of the specific refractivities of water vapor at the feed-forwarded wavelength, we can estimate the group delay at the output wavelength. By estimating the value of Σ_{wv} from eq. 88, we can compute the value of group delay at N band ($\lambda_c = 10\mu\text{m}$) by,

$$x_{g,10} = x_{g,K} + \left[R_{10}^W - R_K^W - \left(\lambda_{10} \frac{dR_{10}^W}{d\lambda_{10}} - \lambda_K \frac{dR_K^W}{d\lambda_K} \right) \right] \Sigma_{wv} \quad (146)$$

Where,

- $x_{g,10}, x_{g,K} \rightarrow$ Group delay in the N band and K band respectively
- $R_{10}^W, R_K^W \rightarrow$ Specific refractivity of a water vapor molecule at N band and K band respectively

However, the group delay estimation is 2-3 magnitudes more sensitive than the phase delay estimation. Hence, we can compare the inter-band dispersion (GD-GD) than the intra-band dispersion (GD-PD) to estimate the dispersion metric and thus Σ_{wv} . With the new GLS based integrated optics beam combiners, we can perform simultaneous K and L band beam combination and estimate the group delay simultaneously (Tepper et al., 2017). The group delay can be expressed as a function of R^W & Σ_{wv} by rewriting eq. 82 as,

$$x_g = x + R^W \Sigma_{wv} + \lambda \frac{dR^W}{d\lambda} \Sigma_{wv} \quad (147)$$

Hence, the difference between the group delays in K and L bands is,

$$x_{g,K} - x_{g,L} = \Sigma_{wv} \left[(R_K^W - R_L^W) - \left(\lambda_K \frac{dR_K^W}{d\lambda_K} - \lambda_L \frac{dR_L^W}{d\lambda_L} \right) \right] \quad (148)$$

Thus, we can derive the instantaneous differential water vapor column density (Σ_{wv}) by using the inter-band group delay difference.

To estimate the efficiency of K+L band feed forward, we can propagate the errors on the group delay estimation from the RMS on the residual group delay from figures 79 & 80. Let us assume that we are feed-forwarding the group delay to coherence fringes in the N band ($\lambda_c = 10\mu\text{m}$) observed with MATISSE at low spectral resolution ($R=30$). Using eq. 145 around the central spectral channel ($9.67\mu\text{m} - 10.33\mu\text{m}$) and assuming a maximum acceptable fringe contrast loss of 10%, the threshold on the RMS on the residual group delay is $38\mu\text{m}$. This results in a threshold on the error on group delay estimation of $9.5\mu\text{m}$ before the application of the control system.

Rewriting eq. 148 as,

$$x_{g,K} - x_{g,L} = C_{K,L} \Sigma_{wv} \quad (149)$$

Where,

$$C_{K,L} = \left[R_K^W - R_L^W - \left(\lambda_K \frac{dR_K^W}{d\lambda_K} - \lambda_L \frac{dR_L^W}{d\lambda_L} \right) \right] \quad (150)$$

Thus the feed-forward group delay at N band can be written as,

$$x_{g,10} = x_{g,K} - C_{K,10} \Sigma \quad (151)$$

Hence, the error on the estimation of Σ_{wv} is given by,

$$\sigma_\Sigma = \frac{\sqrt{\sigma_{gd,K}^2 + \sigma_{gd,L}^2}}{C_{K,L}} \quad (152)$$

Where, $\sigma_{gd,K}$ & $\sigma_{gd,L}$ is the RMS on the residual group delay in K and L bands. Thus the error on the feed-forward group delay in the N band is,

$$\sigma_{gd,10} = \sqrt{\sigma_{gd,K}^2 + (C_{K,10} \sigma_\Sigma)^2} \quad (153)$$

Fig. 88 shows the error on the estimation of Σ_{wv} and fig. 89 shows the feed-forward error on group delay at the N band using K and L band group delay estimation errors.

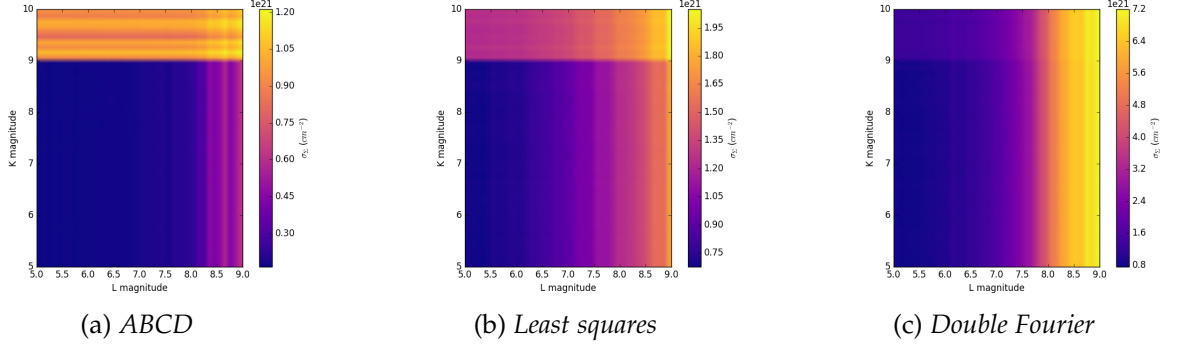


Figure 88: Errors on estimation of Σ_{wv} using K and L band group delay

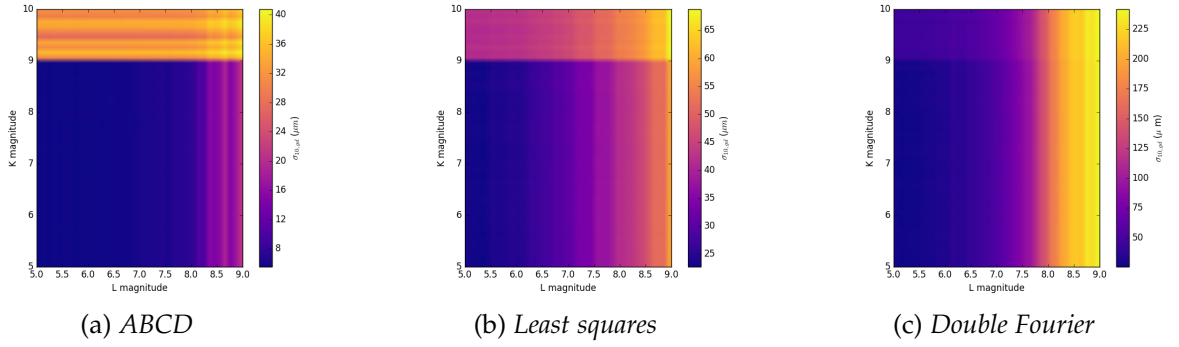


Figure 89: Error on the feed-forward group delay at N band estimated using K and L band group delay estimation errors

To perform coherencing on N band fringes using MATISSE at low spectral resolution ($R=30$) by feed forwarding the N band group delay from K and L band group delay estimates, we have a maximum threshold of $9.5\mu\text{m}$ on the acceptable error for a 10% contrast loss. For this threshold of $9.5\mu\text{m}$, the only possible way to feed-forward the group delay to N band is by using the ABCD group delay estimation in the K and L bands. This gives us a K and L band sensitivity of 8.3 magnitude and 9 magnitude respectively.

This limit applies only when we need to estimate the value of Σ_{wv} instantaneously. However, from fig. 38 the fluctuations of water vapor is small ($\sim 10^{19}\text{cm}^{-2}$) over a few seconds. Combining equations 152 & 153, the error on $\chi_{GD,10}$ can be related to errors on $\chi_{gd,K}$ & $\chi_{gd,L}$ as,

$$\sigma_{gd,10} = \sqrt{\sigma_{gd,K}^2 \left(1 + \left(\frac{C_{K,10}}{C_{K,L}}\right)^2\right) + \sigma_{gd,L}^2 \left(\frac{C_{K,10}}{C_{K,L}}\right)^2} \quad (154)$$

From table 4, the ratio of $C_{K,10}$ and $C_{K,L}$ is,

$$\frac{C_{K,10}}{C_{K,L}} = 14.62 \quad (155)$$

Thus, the errors on K and L band group delay estimation plays a significant role in the instantaneous water vapor estimation and thus the feed forward group delay at longer wavelengths. However, the error on Σ_{wv} can be reduced by averaging over a longer period of time where the fluctuation of Σ_{wv} is sufficiently low.

The difference between K and N band group delay from eq. 151 is the parameter $C_{K,10}\Sigma_{wv}$. The value of $C_{K,10}$ derived from table 4 to be $3.35 \times 10^{-24} \text{cm}^3$. The total excursion of Σ_{wv} from figures 38 & 39 is $\approx 2 \times 10^{20} \text{cm}^{-2}$. Thus the total excursion of the group delay difference between K and N bands is,

$$C_{K,10}\Sigma_{wv} = 3.35\mu\text{m} \quad (156)$$

This will be the maximum difference between the group delays at K and N bands. The maximum coherencing time scale for the N band at low spectral resolution ($R=30$) using eq. 138 is 41.07 seconds. For this time scale the RMS of fluctuation of Σ_{wv} is $2.44 \times 10^{19} \text{cm}^{-2}$ which corresponds to a group delay difference between K and N bands of $0.82\mu\text{m}$. If the coherencing in N band is done with the K band group delay for this time scale while monitoring the fluctuations of Σ_{wv} , we can safely coherence N band fringes with K and L band sensitivities given in table 8. Thus even at the largest fluctuation of Σ_{wv} , we can still keep the RMS on the residual group delay to $3.5\mu\text{m} + 3.35\mu\text{m} = 6.85\mu\text{m}$ which is within the threshold group delay RMS for N band science observations at low spectral resolution with MATISSE.

Fig. 90 shows the decision tree for an efficient way to perform coherencing and cophasing at mid-infrared using K and L band phase and group delays.

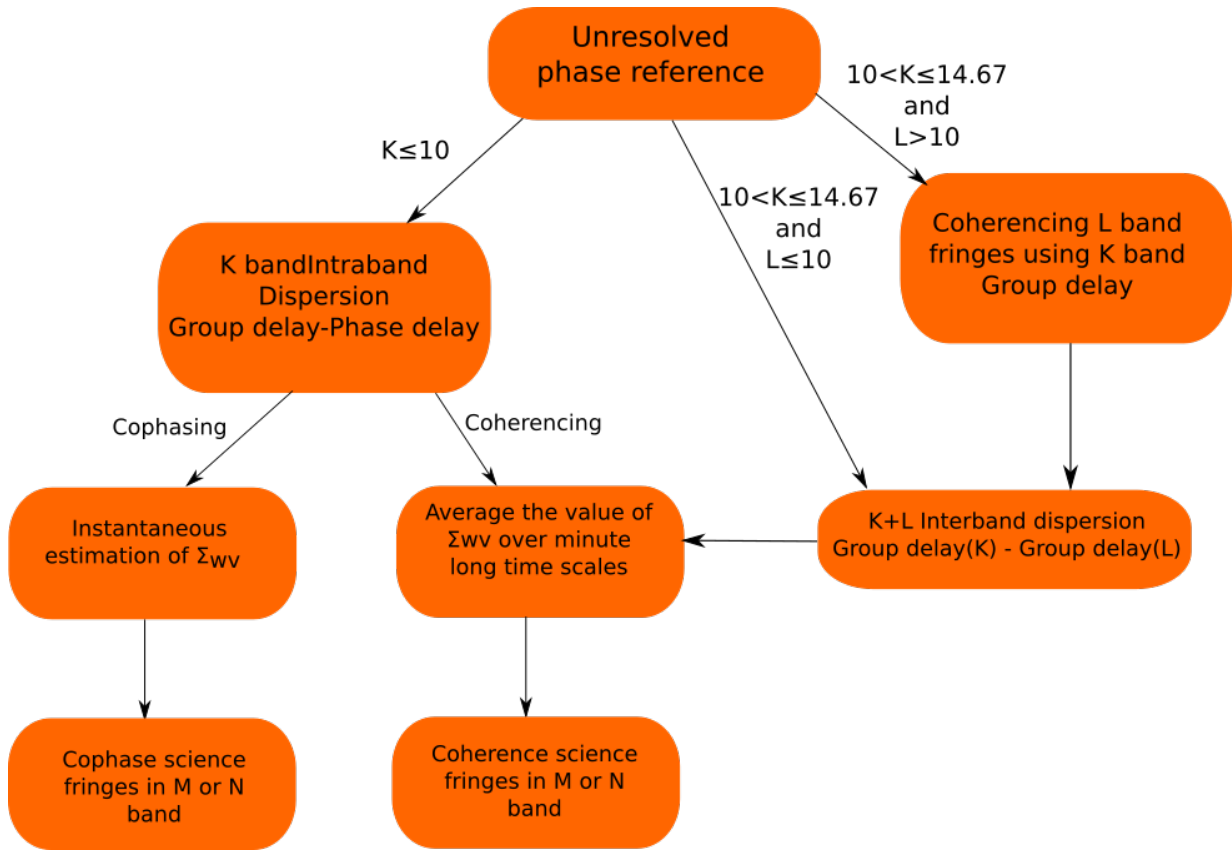


Figure 90: Decision tree for an efficient way to perform coherencing and cophasing at mid-infrared using K and L band group and phase delays.

SUMMARY AND CONCLUSION

Atmospheric turbulence is a major hindrance for high angular resolution astronomical observations in optical and infrared wavelengths. With modern day adaptive optics systems, we can correct for all major optical aberrations caused due to the atmospheric turbulence. However, the global phase shift (piston) is not corrected and plays a major role in the phase of optical and infrared interferometric observations. Hence, a dedicated fringe tracker is required on top of the adaptive optics correction for optical and infrared interferometers.

The main goal of this work is to analyze the possibility to perform simultaneous K and L band group delay estimation for a possible second generation fringe tracker at VLTI. With the arrival of GLS based integrated optics beam combiners which is transparent at near and mid-infrared wavelengths ($1\mu\text{m} - 10\mu\text{m}$), we can simultaneously record K and L band fringes for group delay estimation. The main advantage of moving to a longer wavelength is the longer atmospheric coherence time and hence longer integration time for closed-loop fringe tracking. However, the major challenge at longer wavelength is the high atmospheric and instrumental thermal background. However, this can be overcome with faster chop-nod subtraction or a π phase shift subtraction in interferometry. Hence, the main contribution of the atmospheric background that I have considered in my work is the shot noise of the background.

To understand the effects of atmospheric turbulence and instrumental vibrations on near and mid-infrared interferometric observations, I have built a simulator (GDsim) which simulates the OPD fluctuation time series which also includes the dispersive effects of the atmospheric water vapor. This OPD time series is then applied to a set of K and L band noisy interferometric fringes. The Gravity fringe tracker setup parameters are used to generate the interferometric fringes in the K band and MATISSE L band optical setup parameters are used for the L band fringes. The group delay is then estimated from the noisy fringes using ABCD encoding on dispersed fringes, least squares and double Fourier techniques as described in chapter 5.

One way to estimate the sensitivity of an instrument is through its Signal to Noise Ratio. For interferometric fringes the SNR on the correlated flux given by eq. 98 is suitable to estimate the sensitivity of an interferometer for small integration time. However, at longer integration times ($T_{\text{int}} \geq 1.79\tau_0$) the loss in fringe contrast exhibits a random walk behavior and hence resulting in an asymptotic SNR_c over integration time. Hence,

the SNR_c is not a reliable parameter to estimate the sensitivity at such integration times. Thus I adopted the RMS on the residual group delay, which is the difference between the simulated input group delay and the measured group delay as a marker to estimate the sensitivity and performance of each group delay estimator.

A way to overcome the OPD/phase fluctuations to perform long integration of faint interferometric fringes is to add the fringe frames by their power spectra. Incoherent stacking however still needs the fringes to be within the coherence length to have little to no loss on the fringe contrast and visibilities. The loss of fringe contrast due to the OPD fluctuations is represented in eq.145. Thus assuming a maximum acceptable fringe contrast loss of 10% on the science channel to perform L band science with MATISSE at low spectral resolution ($R=30$), we can coherence the fringes with K and L band sensitivities shown in table 8 for the UTs and table 9 for the ATs at VLTI.

Figures 91 & 92 shows the comparison of K and L magnitudes of class 1 and class 2 YSO from fig.12 with the updated group delay sensitivities from table 8.

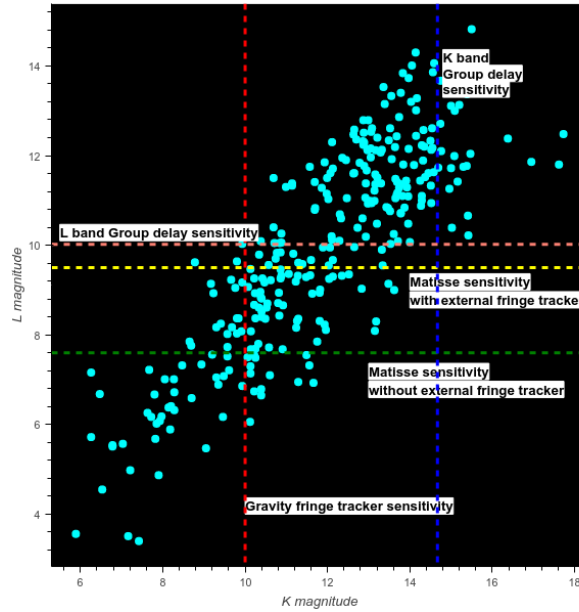


Figure 91: Comparison of K and L magnitudes of class 1 YSOs in embedded clusters with the new group delay sensitivity limits estimated by this work

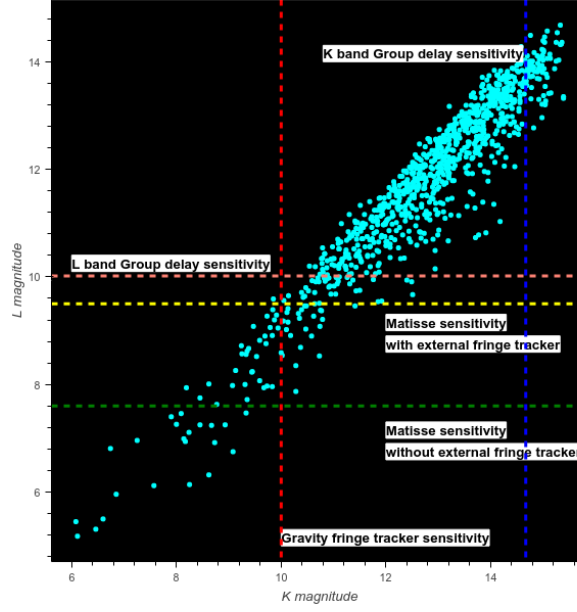


Figure 92: Comparison of K and L magnitudes of class 2 YSOs in embedded clusters with the new group delay sensitivity limits estimated by this work

For mid-infrared interferometry, the current system employs a feed-forward group delay tracking by analyzing the intra-band dispersion (group delay-phase delay) (Koresko et al., 2006). However, as group delay sensitivity is 2-3 magnitudes fainter than the phase delay sensitivity, we can extend the sensitivity of the feed-forward group delay tracker by comparing the inter-band dispersion (group delay-group delay) between two consecutive band instead. As the simulations done in this work looks into both group delay at K and L bands simultaneously, we can directly propagate their group delay estimation errors to mid-infrared (N band, in this case) to estimate the sensitivity of a mid-infrared feed forward group delay tracker. By comparing the RMS on the residual group delays at K and L bands, we can perform feed-forward group delay tracking for science in the N band with MATISSE at low spectral resolution ($R=30$) only by the ABCD group delay estimation technique at K and L bands with a sensitivity of 9.0 magnitude in the K band and 8.3 magnitude in the L band. However, this sensitivity applies only when the feed forward is performed based on the instantaneous value of Σ_{wv} . The contribution of Σ_{wv} on the feed forward group delay over ideal coherencing times is low ($\Delta GD_{K,10} \approx 0.86\mu m$). Thus the value of Σ_{wv} can be averaged over this time scale to reduce the noise σ_{Σ} and thus resulting in a higher sensitivity and a better performance in the feed forward group delay estimation.

7.1 FUTURE WORK

All the work is done by assuming the instrumental properties of Gravity fringe tracker for K band and MATISSE for L' band. The L band group delay estimation performance and sensitivity can be further improved by using laser written GLS based integrated optics beam combiners (Tepper et al., 2017) and better detectors with low noise such as the one reported by Guieu et al. (2014) where it is sensitive till $3.2\mu\text{m}$ with a read noise less than $2e^-$.

We can also extend the current work for increasing the feed-forward group delay sensitivity by utilizing their different integration times. We can increase the L band feed-forward sensitivity by coherencing the fringes during integration using the K band group delay data which runs at a relatively faster duty cycle. This pushes the group delay estimation sensitivity in the L band for mid-infrared feed-forward group delay tracking.

BIBLIOGRAPHY

- Absil, O., den Hartog, R., Gondoin, P., Fabry, P., Wilhelm, R., Gitton, P., & Puech, F. 2006, *A&A*, 448, 787
- Apai, D., Pascucci, I., Bouwman, J., Natta, A., Henning, T., & Dullemond, C. P. 2005, *Science*, 310, 834
- Armitage, P. 2010, *Astrophysics of Planet Formation* (Cambridge University Press)
- Beckmann, V. & Shrader, C. R. 2012, *Active Galactic Nuclei*
- Benisty, M., Berger, J.-P., Jocou, L., Labeye, P., Malbet, F., Perraut, K., & Kern, P. 2009, *A&A*, 498, 601
- Blind, N., Absil, O., Le Bouquin, J.-B., Berger, J.-P., & Chelli, A. 2011, *A&A*, 530, A121
- Bonino, D., Gai, M., Corcione, L., & Massone, G. 2004, in *SPIE*, Vol. 5491, *New Frontiers in Stellar Interferometry*, ed. W. A. Traub, 1463
- Burtscher, L., Meisenheimer, K., Tristram, K. R. W., Jaffe, W., Hönig, S. F., Davies, R. I., Kishimoto, M., Pott, J.-U., Röttgering, H., Schartmann, M., Weigelt, G., & Wolf, S. 2013, *A&A*, 558, A149
- Burtscher, L. & Tristram, K. R. W. 2013, *The Messenger*, 154, 62
- Buscher, D. & Longair, M. 2015, *Practical Optical Interferometry: Imaging at Visible and Infrared Wavelengths*, *Cambridge Observing Handbooks for Research Astronomers* (Cambridge University Press) [\[LINK\]](#)
- Buscher, D. F., Armstrong, J. T., Hummel, C. A., Quirrenbach, A., Mozurkewich, D., Johnston, K. J., Denison, C. S., Colavita, M. M., & Shao, M. 1995, *Applied Optics*, 34, 1081
- Buscher, D., F. 1988, PhD thesis, University of Cambridge
- Caccia, J. L., Azouit, M., & Vernin, J. 1987, *Applied Optics*, 26, 1288
- Champagne, F. H. 1978, *Journal of Fluid Mechanics*, 86, 67 [\[LINK\]](#)
- Choquet, É., Menu, J., Perrin, G., Cassaing, F., Lacour, S., & Eisenhauer, F. 2014, *A&A*, 569, A2

- Ciddor, P. E. 1996, *Applied Optics*, 35, 1566
- Colavita, M. M. 2010, *PASP*, 122, 712
- Colavita, M. M., Swain, M. R., Akeson, R. L., Koresko, C. D., & Hill, R. J. 2004, *PASP*, 116, 876
- Colavita, M. M., Wallace, J. K., Hines, B. E., Gursel, Y., Malbet, F., Palmer, D. L., Pan, X. P., Shao, M., Yu, J. W., Boden, A. F., Dumont, P. J., Gubler, J., Koresko, C. D., Kulkarni, S. R., Lane, B. F., Mobley, D. W., & van Belle, G. T. 1999, *ApJ*, 510, 505
- Connelley, M. S., Reipurth, B., & Tokunaga, A. T. 2008, *AJ*, 135, 2496
- Dali Ali, W., Ziad, A., Berdja, A., Maire, J., Borgnino, J., Sarazin, M., Lombardi, G., Navarrete, J., Vazquez Ramio, H., Reyes, M., Delgado, J. M., Fuensalida, J. J., Tokovinin, A., & Bustos, E. 2010, *A&A*, 524, A73
- Dawson, P., Scholz, A., Ray, T. P., Marsh, K. A., Wood, K., Natta, A., Padgett, D., & Ressler, M. E. 2013, *MNRAS*, 429, 903
- Eckart, A., Mužić, K., Yazici, S., Sabha, N., Shahzamanian, B., Witzel, G., Moser, L., Garcia-Marin, M., Valencia-S., M., Jalali, B., Bremer, M., Straubmeier, C., Rauch, C., Buchholz, R., Kunneriath, D., & Moulta, J. 2013, *A&A*, 551, A18
- Gai, M., Menardi, S., Cesare, S., Bauvir, B., Bonino, D., Corcione, L., Dimmler, M., Massone, G., Reynaud, F., & Wallander, A. 2004, in *SPIE*, Vol. 5491, *New Frontiers in Stellar Interferometry*, ed. W. A. Traub, 528
- Gillessen, S., Genzel, R., Fritz, T. K., Quataert, E., Alig, C., Burkert, A., Cuadra, J., Eisenhauer, F., Pfuhl, O., Dodds-Eden, K., Gammie, C. F., & Ott, T. 2012, *Nature*, 481, 51
- Glindemann, A. 2011, in *Principles of Stellar Interferometry*, *Astronomy and Astrophysics Library* (Springer Berlin Heidelberg), 157–215 [\[LINK\]](#)
- Gravity Collaboration, Abuter, R., Accardo, M., Amorim, A., Anugu, N., Ávila, G., Azouaoui, N., Benisty, M., Berger, J. P., Blind, N., Bonnet, H., Bourget, P., Brandner, W., Brast, R., Buron, A., Burtscher, L., Cassaing, F., Chapron, F., Choquet, É., Clénet, Y., Collin, C., Coudé Du Foresto, V., de Wit, W., de Zeeuw, P. T., Deen, C., Delplancke-Ströbele, F., Dembet, R., Derie, F., Dexter, J., Duvert, G., Ebert, M., Eckart, A., Eisenhauer, F., Esselborn, M., Fédou, P., Finger, G., Garcia, P., Garcia Dabo, C. E., Garcia Lopez, R., Gendron, E., Genzel, R., Gillessen, S., Gonte, F., Gordo, P., Grould, M., Grözing, U., Guieu, S., Haguenauer, P., Hans, O., Haubois, X., Haug, M., Haussmann, F., Henning, T., Hippler, S., Horrobin, M., Huber, A., Hubert, Z., Hubin, N., Hummel, C. A., Jakob, G., Janssen, A., Jochum, L., Jocu, L., Kaufer, A.,

- Kellner, S., Kendrew, S., Kern, L., Kervella, P., Kiekebusch, M., Klein, R., Kok, Y., Kolb, J., Kulas, M., Lacour, S., Lapeyrère, V., Lazareff, B., Le Bouquin, J.-B., Lèna, P., Lenzen, R., Lévêque, S., Lippa, M., Magnard, Y., Mehrgan, L., Mellein, M., Mérand, A., Moreno-Ventas, J., Moulin, T., Müller, E., Müller, F., Neumann, U., Oberti, S., Ott, T., Pallanca, L., Panduro, J., Pasquini, L., Paumard, T., Percheron, I., Perraut, K., Perrin, G., Pflüger, A., Pfuhl, O., Phan Duc, T., Plewa, P. M., Popovic, D., Rabien, S., Ramírez, A., Ramos, J., Rau, C., Riquelme, M., Rohloff, R.-R., Rousset, G., Sanchez-Bermudez, J., Scheithauer, S., Schöller, M., Schuhler, N., Spyromilio, J., Straubmeier, C., Sturm, E., Suarez, M., Tristram, K. R. W., Ventura, N., Vincent, F., Waisberg, I., Wank, I., Weber, J., Wieprecht, E., Wiest, M., Wiezorrek, E., Wittkowski, M., Woillez, J., Wolff, B., Yazici, S., Ziegler, D., & Zins, G. 2017, *A&A*, 602, A94
- Guieu, S., Feautrier, P., Zins, G., Le Bouquin, J.-B., Stadler, E., Kern, P., Rothman, J., Tauvy, M., Coussement, J., de Borniol, E., Gach, J.-L., Jacquard, M., Moulin, T., Rochat, S., Delboulb, A., Derelle, S., Robert, C., Vuillermet, M., Mérand, A., & Bourget, P. 2014, in *SPIE*, Vol. 9146, *Optical and Infrared Interferometry IV*, 91461N
- Gurvich, A. S. & Belen'kii, M. S. 1995, *J. Opt. Soc. Am. A*, 12, 2517 [\[LINK\]](#)
- Gutermuth, R. A., Megeath, S. T., Myers, P. C., Allen, L. E., Pipher, J. L., & Fazio, G. G. 2009, *ApJS*, 184, 18
- Han, C., Udalski, A., Gould, A., Bond, I. A., and, Albrow, M. D., Chung, S.-J., Jung, Y. K., Ryu, Y.-H., Shin, I.-G., Yee, J. C., Zhu, W., Cha, S.-M., Kim, S.-L., Kim, D.-J., Lee, C.-U., Lee, Y., Park, B.-G., KMTNet Collaboration, Skowron, J., Mróz, P., Pietrukowicz, P., Kozłowski, S., Poleski, R., Szymański, M. K., Soszyński, I., Ulaczyk, K., Pawlak, M., The OGLE Collaboration, Abe, F., Asakura, Y., Barry, R., Bennett, D. P., Bhattacharya, A., Donachie, M., Evans, P., Fukui, A., Hirao, Y., Itow, Y., Koshimoto, N., Li, M. C. A., Ling, C. H., Masuda, K., Matsubara, Y., Muraki, Y., Nagakane, M., Ohnishi, K., Ranc, C., Rattenbury, N. J., Saito, T., Sharan, A., Sullivan, D. J., Sumi, T., Suzuki, D., Tristram, P. J., Yamada, T., Yamada, T., Yonehara, A., & The MOA Collaboration. 2017, *AJ*, 154, 133
- Hayashi, C. & Nakano, T. 1963, *Progress of Theoretical Physics*, 30, 460
- Honda, M., Inoue, A. K., Fukagawa, M., Oka, A., Nakamoto, T., Ishii, M., Terada, H., Takato, N., Kawakita, H., Okamoto, Y. K., Shibai, H., Tamura, M., Kudo, T., & Itoh, Y. 2009, *ApJL*, 690, L110
- Houairi, K., Cassaing, F., Perrin, G., Eisenhauer, F., Brandner, W., Straubmeier, C., & Gillessen, S. 2008, in *SPIE*, Vol. 7013, *Optical and Infrared Interferometry*, 70131B
- Ji, X. & Pu, Z. 2009, *Journal of Optics A: Pure and Applied Optics*, 11, 045701

- Kaimal, J. C., Wyngaard, J. C., Haugen, D. A., Coté, O. R., & Izumi, Y. 1976, *Journal of the atmospheric sciences*, 33
- Kerr, J. R. 1972, *J. Opt. Soc. Am.*, 62, 1040
- Kolmogorov, A. 1941, *Akademiia Nauk SSSR Doklady*, 30, 301
- Koresko, C., Colavita, M. M., Serabyn, E., Booth, A., & Garcia, J. 2006, in *SPIE*, Vol. 6268, *Society of Photo-Optical Instrumentation Engineers (SPIE) Conference Series*, 626817
- Kumar, S. S. 1963, *ApJ*, 137, 1121
- Lada, C. J. & Wilking, B. A. 1984, *ApJ*, 287, 610
- Lakshminarayanan, V. & Fleck, A. 2011, *Journal of Modern Optics*, 58, 545
- Lawson, J. K. & Carrano, C. J. 2006, *Proc. SPIE*, 6303, 630304
- Lawson, P. R., Colavita, M. M., Dumont, P. J., & Lane, B. F. in , *SPIE*, Vol. 4006, *Interferometry in Optical Astronomy*, ed. P. LénaA. Quirrenbach, 397–406
- Lay, O. P. 1997, *A&As*, 122
- Lazareff, B., Blind, N., Jocou, L., Eisenhauer, F., Perraut, K., Lacour, S., Delplancke, F., Schoeller, M., Amorim, A., Brandner, W., Perrin, G., & Straubmeier, C. 2014, in *SPIE*, Vol. 9146, *Optical and Infrared Interferometry IV*, 91460X
- Le Bouquin, J.-B., Abuter, R., Bauvir, B., Bonnet, H., Haguénauer, P., di Lieto, N., Menardi, S., Morel, S., Rantakyö, F., Schoeller, M., Wallander, A., & Wehner, S. 2008, in *SPIE*, Vol. 7013, *Optical and Infrared Interferometry*, 701318
- Leinert, C. 2003, in *ESA Special Publication*, Vol. 522, *GENIE - DARWIN Workshop - Hunting for Planets*, 27
- Luhman, K. L. 1999, *ApJ*, 525, 466
- Luhman, K. L., Adame, L., D'Alessio, P., Calvet, N., McLeod, K. K., Bohac, C. J., Forrest, W. J., Hartmann, L., Sargent, B., & Watson, D. M. 2007, *ApJ*, 666, 1219
- Maréchal, A. 1947, *Rev. Opt. Theor. Instrum.*, 26, 257
- Martin, F., Conan, R., Tokovinin, A., Ziad, A., Trinquet, H., Borgnino, J., Agabi, A., & Sarazin, M. 2000, *A&As*, 144, 39
- Masson, C. R. in , *Astronomical Society of the Pacific Conference Series*, Vol. 59, *IAU Colloq. 140: Astronomy with Millimeter and Submillimeter Wave Interferometry*, ed. M. IshiguroJ. Welch, 87–95

- Mathar, R. J. 2004, *Applied Optics*, 43, 928
- Matsumoto, H. 1982, *Metrologia*, 18, 49
- Matter, A., Lagarde, S., Petrov, R. G., Berio, P., Robbe-Dubois, S., Lopez, B., Antonelli, P., Allouche, F., Cruzalebes, P., Millour, F., Bazin, G., & Bourgès, L. 2016, in *SPIE*, Vol. 9907, *Optical and Infrared Interferometry and Imaging V*, 990728
- Mérand, A., Patru, F., Berger, J.-P., Percheron, I., & Poupar, S. 2012, in *Society of Photo-Optical Instrumentation Engineers (SPIE) Conference Series*, Vol. 8445, *Society of Photo-Optical Instrumentation Engineers (SPIE) Conference Series*, 1
- Millour, F., Berio, P., Heininger, M., Hofmann, K.-H., Schertl, D., Weigelt, G., Guitton, F., Jaffe, W., Beckmann, U., Petrov, R., Allouche, F., Robbe-Dubois, S., Lagarde, S., Soulain, A., Meilland, A., Matter, A., Cruzalèbes, P., & Lopez, B. 2016, in *SPIE*, Vol. 9907, *Optical and Infrared Interferometry and Imaging V*, 990723
- Mohanty, S., Greaves, J., Mortlock, D., Pascucci, I., Scholz, A., Thompson, M., Apai, D., Lodato, G., &Looper, D. 2013, *ApJ*, 773, 168
- Mróz, P., Udalski, A., Bond, I. A., Skowron, J., Sumi, T., Han, C., Szymański, M. K., Soszyński, I., Poleski, R., Pietrukowicz, P., Kozłowski, S., Wyrzykowski, Ł., Ulaczyk, K., The OGLE Collaboration, Abe, F., Asakura, Y., Barry, R. K., Bennett, D. P., Bhattacharya, A., Donachie, M., Evans, P., Fukui, A., Hirao, Y., Itow, Y., Koshimoto, N., Li, M. C. A., Ling, C. H., Masuda, K., Matsubara, Y., Muraki, Y., Nagakane, M., Ohnishi, K., Ranc, C., Rattenbury, N. J., Saito, T., Sharan, A., Sullivan, D. J., Suzuki, D., Tristram, P. J., Yamada, T., Yamada, T., Yonehara, A., & The MOA Collaboration. 2017, *AJ*, 154, 205
- Muench, A. A., Alves, J., Lada, C. J., & Lada, E. A. 2001, *ApJL*, 558, L51
- Muthusubramanian, B., Labadie, L., Pott, J.-U., Tepper, J., Minardi, S., & Diener, R. 2016, in *SPIE*, Vol. 9907, *Optical and Infrared Interferometry and Imaging V*, 990736
- Muzerolle, J., Adame, L., D'Alessio, P., Calvet, N., Luhman, K. L., Muench, A. A., Lada, C. J., Rieke, G. H., Siegler, N., Trilling, D. E., Young, E. T., Allen, L., Hartmann, L., & Megeath, S. T. 2006, *ApJ*, 643, 1003
- Nightingale, N. S. & Buscher, D. F. 1991, *MNRAS*, 251, 155
- Noll, R. J. 1976, *Journal of the Optical Society of America* (1917-1983), 66, 207
- Pedretti, E., Thureau, N. D., Wilson, E., Traub, W. A., Monnier, J. D., Ragland, S., Carleton, N. P., Millan-Gabet, R., Schloerb, F. P., Brewer, M. K., Berger, J.-P., & Lacasse, M. G. 2004, in *SPIE*, Vol. 5491, *New Frontiers in Stellar Interferometry*, 540–550

- Pedretti, E., Traub, W. A., Monnier, J. D., Millan-Gabet, R., Carleton, N. P., Schloerb, F. P., Brewer, M. K., Berger, J.-P., Lacasse, M. G., & Ragland, S. 2005, *Applied Optics*, 44, 5173
- Perrin, G., Fédou, P., Dembet, R., Choquet, E., & Menu, J. 2011, 3, 1
- Petrov, R., Roddier, F., & Aime, C. 1986, *Journal of the Optical Society of America A*, 3, 634
- Petrov, R. G., Boskri, A., Bresson, Y., Agabi, K., Folcher, J.-P., Elhalkouj, T., Lagarde, S., & Benkhaldoun, Z. 2016, in *SPIE*, Vol. 9907, *Society of Photo-Optical Instrumentation Engineers (SPIE) Conference Series*, 99071F
- Petrov, R. G., Malbet, F., Weigelt, G., Antonelli, P., Beckmann, U., Bresson, Y., Chelli, A., Dugué, M., Duvert, G., Gennari, S., Glück, L., Kern, P., Lagarde, S., Le Coarer, E., Lisi, F., Millour, F., Perraut, K., Puget, P., Rantakyrö, F., Robbe-Dubois, S., Roussel, A., Salinari, P., Tatulli, E., Zins, G., Accardo, M., Acke, B., Agabi, K., Altariba, E., Arezki, B., Aristidi, E., Baffa, C., Behrend, J., Blöcker, T., Bonhomme, S., Busoni, S., Cassaing, F., Clausse, J.-M., Colin, J., Connot, C., Delboulbé, A., Domiciano de Souza, A., Driebe, T., Feautrier, P., Ferruzzi, D., Forveille, T., Fossat, E., Foy, R., Fraix-Burnet, D., Gallardo, A., Giani, E., Gil, C., Glentzlin, A., Heiden, M., Heininger, M., Hernandez Utrera, O., Hofmann, K.-H., Kamm, D., Kiekebusch, M., Kraus, S., Le Contel, D., Le Contel, J.-M., Lesourd, T., Lopez, B., Lopez, M., Magnard, Y., Marconi, A., Mars, G., Martinot-Lagarde, G., Mathias, P., Mège, P., Monin, J.-L., Mouillet, D., Mourard, D., Nussbaum, E., Ohnaka, K., Pacheco, J., Perrier, C., Rabbia, Y., Rebattu, S., Reynaud, F., Richichi, A., Robini, A., Sacchettini, M., Schertl, D., Schöller, M., Solscheid, W., Spang, A., Stee, P., Stefanini, P., Tallon, M., Tallon-Bosc, I., Tasso, D., Testi, L., Vakili, F., von der Lühse, O., Valtier, J.-C., Vannier, M., & Ventura, N. 2007, *A&A*, 464, 1
- Pinilla, P., Birnstiel, T., Benisty, M., Ricci, L., Natta, A., Dullemond, C. P., Dominik, C., & Testi, L. 2013, *A&A*, 554, A95
- Quirrenbach, A. 2014, http://cfao.ucolick.org/aosummer/book/pdf/3.1_quirrenbach.pdf
- Reeves, A. 2016, in *SPIE*, Vol. 9909, *Adaptive Optics Systems V*, 99097F
- Rigaut, F. & Van Dam, M. in , *Proceedings of the Third AO4ELT Conference*, ed. S. EspositoL. Fini, 18
- Roberts, Jr., L. C. & Bradford, L. W. 2011, *Optics Express*, 19, 820
- Roddier, F. 1981, *Progress in optics. Volume 19*. Amsterdam, North-Holland Publishing Co., 1981, p. 281-376., 19, 281

- Ross, T. S. 2009, *Applied Optics*, 48, 1812
- Sahlmann, J., Ménardi, S., Abuter, R., Accardo, M., Mottini, S., & Delplancke, F. 2009, *A&A*, 507, 1739
- Shahzamanian, B., Eckart, A., Zajaček, M., Valencia-S., M., Sabha, N., Moser, L., Parsa, M., Peissker, F., & Straubmeier, C. 2016, *A&A*, 593, A131
- Shao, M. & Staelin, D. H. 1977, *Journal of the Optical Society of America* (1917-1983), 67, 81
- Tatarski, V. I., Silverman, R. A., & Chako, N. 1961, *Physics Today*, 14, 46
- Taylor, G. I. 1938, *Proceedings of the Royal Society of London Series A*, 164, 476
- Tepper, J., Labadie, L., Diener, R., Minardi, S., Pott, J.-U., Thomson, R., & Nolte, S. 2017, *A&A*, 602, A66
- Thomas, S. SPIE, Vol. 5490, , *Advancements in Adaptive Optics*, ed. D. Bonaccini CaliaB. L. Ellerbroek & R. Ragazzoni, 766–773
- Thureau, N. D., Boysen, R. C., Buscher, D. F., Haniff, C. A., Pedretti, E., Warner, P. J., & Young, J. S. 2003, in SPIE, Vol. 4838, *Interferometry for Optical Astronomy II*, ed. W. A. Traub, 956–963
- Trani, A. A., Mapelli, M., Spera, M., & Bressan, A. 2016, *ApJ*, 831, 61
- Tristram, K. R. W., Meisenheimer, K., Jaffe, W., Schartmann, M., Rix, H.-W., Leinert, C., Morel, S., Wittkowski, M., Röttgering, H., Perrin, G., Lopez, B., Raban, D., Cotton, W. D., Graser, U., Paresce, F., & Henning, T. 2007, *A&A*, 474, 837
- Štefl, S., Parra, R., & Lundgren, A. 2012, in SPIE, Vol. 8445, *Optical and Infrared Interferometry III*, 844524
- von Kármán, T. 1948, *Proceedings of the National Academy of Science*, 34, 530
- Walters, D. L. & Kunkel, K. E. 1981, *J. Opt. Soc. Am.*, 71, 397 [\[LINK\]](#)
- Wilson, E., Pedretti, E., Bregman, J., Mah, R. W., & Traub, W. A. 2005, *EURASIP Journal on Applied Signal Processing*, 2005, 531501
- Zajaček, M., Britzen, S., Eckart, A., Shahzamanian, B., Busch, G., Karas, V., Parsa, M., Peissker, F., Dovčiak, M., Subroweit, M., Dinnbier, F., & Zensus, J. A. 2017, *A&A*, 602, A121
- Zernike, F. 1938, *Physica*, 5, 785
- Zilberman, A., Golbraikh, E., & Kopeika, N. S. 2008, *Appl. Opt.*, 47, 6385 [\[LINK\]](#)

ACKNOWLEDGMENTS

To start with the list of people I would like to thank for supporting me throughout, I would definitely need to write a list as long as this thesis.

I would like to first thank my advisor Prof. Dr. Lucas Labadie for believing in me and supporting me right from the time I applied for this position till today. I really enjoyed all the fun filled discussions about work and my interests. He has also encouraged me to work on other projects like Adaptive Optics and Lucky Imager (AOLI) on the side along with my main work.

I also thank Dr. Jörg-Uwe Pott for sharing his expertise in Adaptive Optics & Fringe tracking and his valuable guidance throughout my PhD. He was ready to answer all my questions anytime, either through email or Skype or in person. I really enjoyed all my visits to Max Planck Institute for Astronomy, Heidelberg.

A special thanks goes to Konstantinos Markakis for morally supporting me through all my tough times throughout my PhD also for reading and commenting on my thesis. I also thank Banafsheh Shazamian and Rebekka Grellman for reading and providing me comments on the thesis.

I am also grateful to all my office mates of room #211, Gerold, Banafsheh, Kostas, Marcus, Dominik, Madalina and Madeleine for putting up with me and for all the fun we had over the last three years.

A special thanks goes to all my group mates of the HiRES group, Andres, Anas, Fabio, Jan, Nicola and Rebekka for all the fun times we had together during conferences and meetings, also for putting up with my crazy ideas. I would also like to thank everyone from aegroup, Abhijeet, Banafsheh, Gerold, Kostas, Mathias, Florian, Nadeen, Nastaran, Mathew, etc. for all the fun times during hangouts, movies, beers, food.

I am also grateful to my professors from my Masters, Prof. Dr. Inga Kamp and Prof. Dr. Scott Trager for inspiring me to pursue a PhD in Astrophysics.

I am also deeply thankful to my sister Anusha Muthusubramanian, who was always there to support me emotionally and morally through out my life till my PhD and especially during my PhD.

I am also thankful to all my friends and fellow members of the Tamil Nadu Astronomy Association, Chennai for all the motivation and support right from my childhood to push me into Astronomy. I would also like to thank Sarrvesh, Kavita, Vinothini, Sai Krishna and Vinodh who were also nurtured by the club and are in professional astronomy today.

A special thanks goes to Dr. Ramesh Karuppusamy from Max Planck Institute for Radio Astronomy, Bonn and his family for their moral support and our outings and great discussions together.

Last but not the least, I am grateful to all my friends from around Cologne, Lukas, Giovanni, Julien, Anna, Uwe, Dawid, Tuba, Floh and Inga and to the people at Chlodwig Eck, Robert, Oli, Luca who made sure I am always back normal after a crazy week of PhD research.

Without all their support I wouldn't have come this far towards the completion of my PhD.

ERKLÄRUNG

Ich versichere, daß ich die von mir vorgelegte Dissertation selbständig angefertigt, die benutzten Quellen und Hilfsmittel vollständig angegeben und die Stellen der Arbeit – einschließlich Tabellen, Karten und Abbildungen –, die anderen Werken im Wortlaut oder dem Sinn nach entnommen sind, in jedem Einzelfall als Entlehnung kenntlich gemacht habe; daß diese Dissertation noch keiner anderen Fakultät oder Universität zur Prüfung vorgelegen hat; daß sie – abgesehen von unten angegebenen Teilpublikationen – noch nicht veröffentlicht worden ist sowie, daß ich eine solche Veröffentlichung vor Abschluß des Promotionsverfahrens nicht vornehmen werde. Die Bestimmungen dieser Promotionsordnung sind mir bekannt. Die von mir vorgelegte Dissertation ist von Prof. Dr. Lucas Labadie betreut worden.

Köln, 17.04.2019

Balaji Muthusubramanian

LEBENS LAUF

ZUR PERSON

| | |
|---------------------|--|
| Name | Balaji Muthusubramanian |
| Adresse | Augustastr. 6, 50996 Cologne, Germany |
| Telefon | +49-221-4707787 |
| E-Mail | muthusu@ph1.uni-koeln.de |
| Staatsangehörigkeit | Indisch |
| Geburtsdatum | 7.Februar.1992 |

BILDUNG

- | | |
|---------------------------|---|
| ▷ Zeitraum | November 2014- |
| ○ Erworbene Qualifikation | Promotion |
| ○ Bildungseinrichtung | I. Physikalisches Institut, Universität zu Köln, Köln, Deutschland |
| ○ Hauptfäch | Experimental physik |
| ▷ Zeitraum | 2012-2014 |
| ○ Erworbene Qualifikation | Masters of Science |
| ○ Hauptfäch | Astronomy |
| ○ Bildungseinrichtung | Kapteyn Astronomical Institute, Rijksuniversiteit Groningen, Groningen, Niederlande |
| ▷ Zeitraum | 2009-2012 |
| ○ Erworbene Qualifikation | Bachelor of Science |
| ○ Hauptfäch | Physik |
| ○ Bildungseinrichtung | University of Madras, Chennai, India |
| ▷ Zeitraum | 2007-2009 |
| ○ Erworbene Qualifikation | High School |
| ○ Bildungseinricht | Sir Sivaswami Kalalaya, Chennai, India |

FORSCHUNG

- | | |
|------------------|--|
| ▷ Dissertation | „Simulations of group-delay tracking strategies in the astronomical K and L bands - For improved sensitivities at the Very Large Telescope Interferometer“ — I. Physikalisches Institut, Universität zu Köln, Köln, Deutschland |
| ▷ Masters arbeit | „Comparison study of brown dwarf protoplanetary disks with T Tauri and Herbig protoplanetary disks“ — Kapteyn Astronomical Institute, Rijksuniversiteit Groningen, Groningen, Niederlande |